

Article

# High Accuracy Buoyancy for Underwater Gliders: The Uncertainty in the Depth Control <sup>†</sup>

Enrico Petritoli, Fabio Leccese \* and Marco Cagnetti

Science Department, Università degli Studi “Roma Tre”, Via della Vasca Navale n. 84, 00146 Rome, Italy; e\_petriloti@libero.it (E.P.); ing.marco.cagnetti@gmail.com (M.C.)

\* Correspondence: fabio.leccese@uniroma3.it; Tel.: +39-06-5733-7347

<sup>†</sup> This paper is an extended version of our paper published in Petritoli, E.; Leccese, F.; Cagnetti, M. A High Accuracy Buoyancy System Control for an Underwater Glider. In Proceedings of the second IEEE International Workshop on Metrology for the Sea (MetroSea), Bari, Italy, 8–10 October 2018.

Received: 8 March 2019; Accepted: 12 April 2019; Published: 17 April 2019

**Abstract:** This paper is a section of several preliminary studies of the Underwater Drones Group of the Università degli Studi “Roma Tre” Science Department: We describe the study philosophy, the theoretical technological considerations for sizing and the development of a technological demonstrator of a high accuracy buoyancy and depth control. We develop the main requirements and the boundary conditions that design the buoyancy system and develop the mathematical conditions that define the main parameters.

**Keywords:** uncertainty; buoyancy; depth control; accuracy; AUV; glider; autonomous; underwater; vehicle

## 1. Introduction

This paper is part of several preliminary studies by Underwater Drones Group (UDG) of the Science Department of the Università degli Studi “Roma Tre”, which is developing an advanced Autonomous Underwater Vehicle (AUV) for the exploration of the sea at high depths. The final aim of the project is to create a platform for underwater scientific research that can accommodate a wide range of different payloads.

We will examine the buoyancy system and evaluate its sizing; then we will illustrate the technological solution we have come up with in order to realize the hydraulic system to be assembled in the Underwater Glider Mk. III (see Figure 1) [1–5].

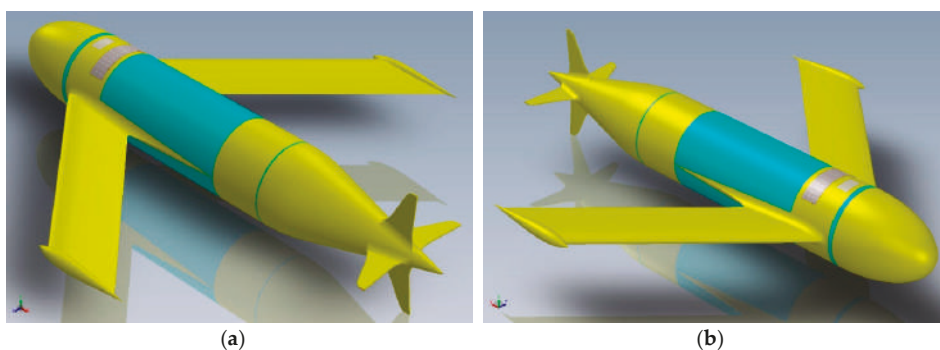


Figure 1. Perspective view of the Underwater Glider Mk. III. (a) Rear/port; (b) front/starboard.

## 1.1. The Underwater Glider

### 1.1.1. AUV Evolution

The exploration of the underwater world has always been one of mankind's dreams: submarines and bathyscaphes (for extreme depths) have been developed to study the "deep blue". Due to obvious dangers, the human exploration can take place only for very short periods and very limited areas: for these reasons, the exploration of the sea has immediately been drawn towards unmanned automatic systems [6–8].

An AUV is a vehicle that travels underwater without requiring input from an operator; this means that it must be equipped with a "brain" that regulates and coordinates its position, its depth and its speed: moreover, it is able to collect and store data from the payload. One of the first realizations was the Autonomous LAgrangian Circulation Explorer (ALACE) system, a buoy that was able to vary its buoyancy and therefore its depth. Although it possessed a great endurance, it only could be employed for great depths and in open sea—the consequences of these limitations are evident.

The next step was the use of Remote Operated Vehicles (ROVs). These, thanks to the constant development of electronic miniaturization, are extremely high performing vehicles for short-lasting marine operations, but they require the constant presence of a support vessel.

The need to get rid of the randomness of the currents has led to the natural development of the underwater glider concept [9–15].

### 1.1.2. The Underwater Glider

An underwater glider is a vehicle that, by changing its buoyancy, moves up and down in the ocean like a profiling float [16]. It uses hydrodynamic wings to convert vertical motion into horizontal motion, moving forward with very low power consumption [17–22]. While not as fast as conventional AUVs, the glider, using buoyancy-based propulsion, offers increased range and endurance compared to motor-driven vehicles and missions may extend to months and to several thousands of kilometres in range. An underwater glider follows an up-and-down, sawtooth-like mission profile providing data on temporal and spatial scales unavailable with previous types of AUVs [23–27].

### 1.1.3. The Mk. III Architecture

The Mk. III sub-glider has a cylindrical fuselage with a radome on the bow containing the customizable payload and, on the other end, the hydrodynamic fairing. The vehicle does not have moving surfaces: control is provided by the displacement of the battery package that varies the position of the centre of mass. The wings aerofoil is based on the Eppler E838 Hydrofoil. The aerofoil has the maximum thickness 18.4% at 37.2% chord and maximum camber 0% at 46.5% chord. The arrangement of the internal sectors is visible in Figure 2a,b. The buoyancy system is contained in the buoyancy control bay: it accommodates the buoyancy motor and the oil tank and provides longitudinal balance to the system by adjusting the level in the reservoir. The bladder is contained in the hydrodynamic fairing, in contact with the open water. The fairing is not a critical structural part—it has the task of not disturbing the hydrodynamic flow of the fuselage [28].

### 1.1.4. Conventions

We introduce, for clarity, the mathematical conventions and symbols that will be used in the subsequent discussion (see Figure 3a,b): where:

- $\alpha$  (or  $\varphi$ ) is the angle between the  $x$  axis and the  $N$  axis.
- $\beta$  (or  $\theta$ ) is the angle between the  $z$  axis and the  $Z$  axis.
- $\gamma$  (or  $\psi$ ) is the angle between the  $N$  axis and the  $X$  axis.

For the rotation matrix, we have:

$$R = \begin{pmatrix} 0 & -\zeta_z & \zeta_y \\ \zeta_z & 0 & -\zeta_x \\ -\zeta_y & \zeta_x & 0 \end{pmatrix} \tag{1}$$

where  $\zeta$  is the parameter vector [29].

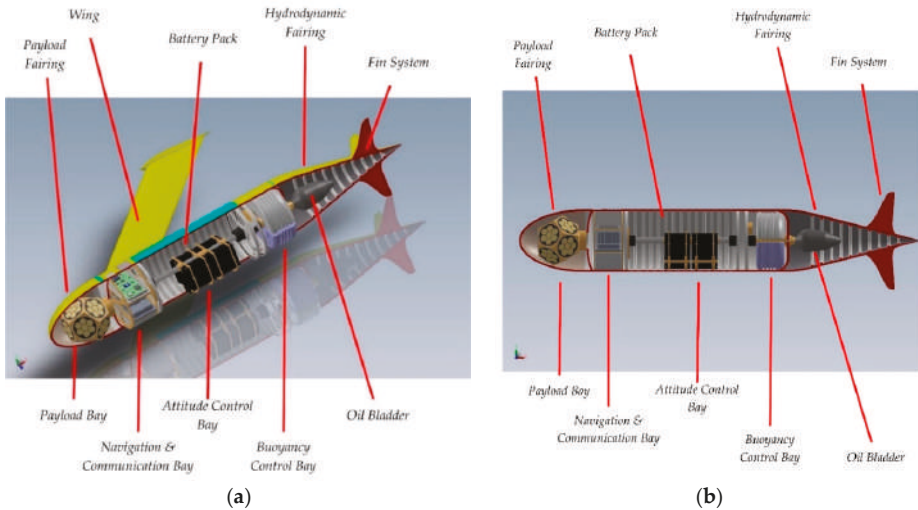


**Figure 2.** Underwater Glider Mk. III cutaway: (a) fuselage prospective section; (b) fuselage sagittal section.

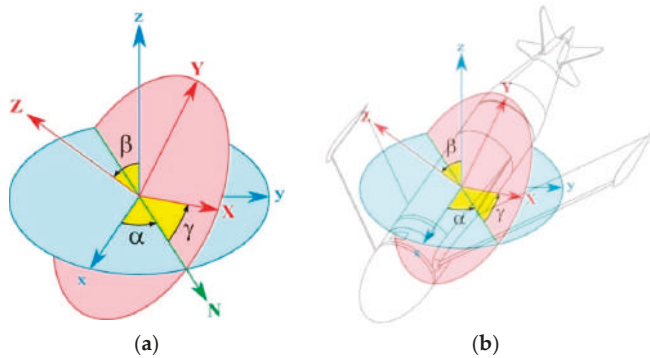


**Figure 3.** The Euler angles. (a) Body frame (blue) and reference frame (red); (b) The body frame referred to the drone.

## 2. Materials and Methods

### 2.1. The Buoyancy System

#### 2.1.1. Basic Concepts

Gliders are controlled through hydrostatics (vertical forces) and manipulate hydrostatic balances in order to accomplish roll and pitch of the vehicle. Stability of the vehicle is a major critical factor:

a stable vehicle has the centre of gravity below the centre of buoyancy. In this configuration, the weight of the vehicle creates a restoring moment to add stability to the vehicle. Roll and pitch on the glider is accomplished by moving the battery pack. Figure 4 below displays a basic concept of a buoyancy system for the glider [30–36].

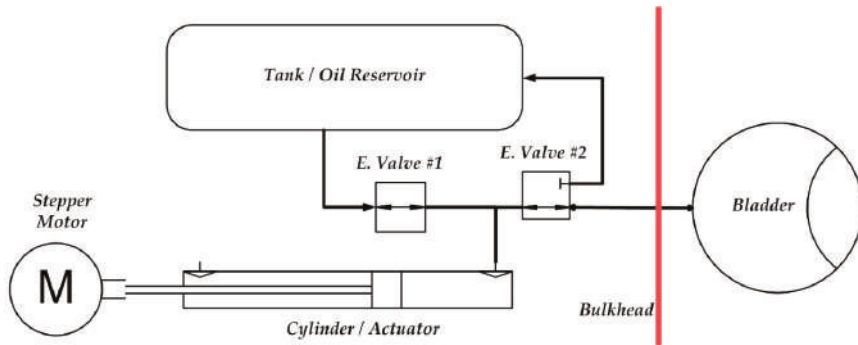


Figure 4. Basic scheme of the buoyancy system.

The system is extremely simple: while descending, hydraulic fluid moves from the external inflatable bladder, which produces a high pressure in the internal reservoir, which is at a low pressure through a valve: the decrease in volume of the bladder creates an increase in density, causing negative buoyancy [37–44].

While ascending, hydraulic fluid moves from internal accumulator to the external inflatable bladder through the pump. The increase in volume creates a decrease in density causing positive buoyancy. The seawater also flushes out the open hydrodynamic fairing of the vehicle, aiding it to rise to the surface. For neutral buoyancy, the vehicle must have a density equal to seawater [45–52].

### 2.1.2. The System Prototype

Our group has developed a technology demonstrator (see Figure 4) of the buoyancy system to validate the related technology and then to test it. To reduce the force required to actuate the oil piston, which pushes the oil in the bladder at high pressure, is necessary to reduce the piston surface (diameter) and increase the stroke: so, the buoyancy engine resembles a “shotgun”. An open-loop stepper motor was used to drive the screw inside the actuator that, in turn, pushes the piston. Two solenoid valves regulate the flow of oil into the bladder [53–57].

The first problem was the occurrence of actuator buckling: under the push of the engine, the probability of a part bending is high, thus deforming the thread and jamming the mechanism. The problem was solved by constructing a rigid cage with four struts that support the piston’s push load, leaving the screw only with the rolling friction load. In the early project development stages, the workgroup was oriented to use a centrifugal pump for all drives: this technology however did not allow us to create strong pressure differences; the need to use a more powerful engine was also highlighted because the prevalence was too low: this would have led to an excessive battery consumption. The second solution was to use volumetric pumps in order to obtain greater differences in pressure (even ones considerably higher than needed). Unfortunately, these would require too much power and are too heavy for our small vehicle [58–62].

At this stage of development, we have also thought to use the oil tank only as a passive fluid reservoir and trimmable counterweight of the payload and as an active actuator for longitudinal stability. The long travel of the piston (forward or backward) ensures the necessary variation of the bladder volume for manoeuvrability [63].

Now, the system prototype seems to work correctly and promises new developments: it is under in several fatigue cycle trials in order to investigate the parts more prone to failure as a sort of burn-in test. Our prototype (breadboard) is presented in Figure 5.

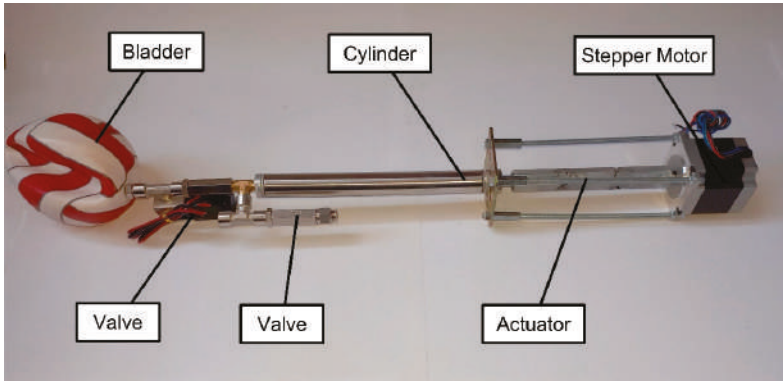


Figure 5. Buoyancy engine prototype.

## 2.2. Buoyancy

Archimedes’ principle is the main concept underlying the buoyancy of underwater vehicles. When a vehicle is submerged in water, a buoyant force acts on the body vertically upward due to the pressure forces below the submerged body being greater than the pressure forces above. The buoyant force results in a value equal to the weight it displaces [64].

### 2.2.1. Static Buoyancy

Now, consider our drone (see Figure 6): it is in steady state.

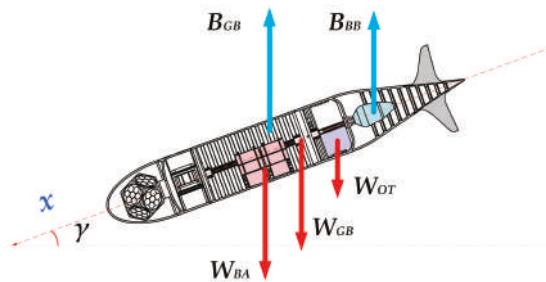


Figure 6. Drone in buoyancy Balance.

In these conditions, the total weight  $W_{TOT}$  of the glider is given by:

$$W_{TOT} = -W_{DW} + B_{GB} + B_{BB} \tag{2}$$

where:

$W_{TOT}$  = Net total “weight” in the water.

$W_{DW}$  = Dry Weight of the glider.

$B_{BB}$  = Buoyancy of the oil bladder.

$B_{GB}$  = Buoyancy of the naked glider.

The expression of dry weight is:

$$W_{DW} = W_{BA} + W_{OT} + W_{GB} \quad (3)$$

where:

$W_{BA}$  = Weight of the battery pack.

$W_{OT}$  = Weight of the oil tank.

$W_{GB}$  = Weight of the naked glider (without oil tank and batteries). For “dry weight”, we mean the weight of the vehicle out of the sea, without the hydrostatic force.

So Equation (2) becomes:

$$\sum F_z = W_{BA} + W_{OT} + W_{GB} + B_{GB} + B_{BB} = 0 \quad (4)$$

This series of equations will be useful later to establish the drone descent attitude.

### 2.2.2. Dynamic Balance on the Vertical Plane

Here, the drone dive (or emersion) is examined at constant speed: it is in steady-state gliding, the geometry of total forces is explained in Figure 7a. Figure 7b shows the Eppler E838 characteristic “Cl vs. Alpha (=angle of attack  $\alpha_{att}$ )”.

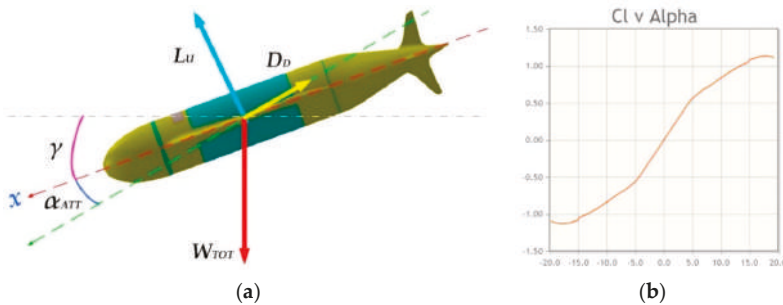


**Figure 7.** Dynamic balance of the forces (a) Drone geometrical balance of the forces; (b) Cl vs. Alpha (=angle of attack,  $\alpha_{att}$  diagram for Eppler E838 aerofoil.

At equilibrium, for the dynamics on the vertical plane at constant speed we have:

$$\vec{W}_{TOT} + \vec{L} + \vec{D} = 0 \quad (5)$$

The expression for the lift is:

$$L = \frac{1}{2} \rho v^2 S C_L \quad (6)$$

According to the Eppler E838 characteristic “Cl vs. Alpha” (Figure 7b) when the angle of attack  $\alpha_{att} = 0^\circ$  (is null) the  $C_L$  is zero so that the lift force  $L$  is null. This shows that the drone cannot progress horizontally at constant speed (straight and level): the only mission profile allowed is a sawtooth curve [65].

### 2.2.3. Glider Trajectory

Because its motion is due to the difference between the forces of weight and buoyancy, the glider is unable to proceed straight and level, thus being forced to follow a dive/climb trajectory made smooth by the wings. Moreover, unlike gliders in air, AUVs can have ascending glide slopes if the net buoyancy is positive, producing a negative sink rate.

The buoyancy engine of the glider allows changing its net buoyancy into alternating positive and negative states, thereby imparting it with the ability to string together a succession of descending and ascending glide slopes referred to as a sawtooth glide.

The behaviour of the vehicle is considered in case of a simple glide slope (refer to Figure 7a):

$$\begin{aligned} \text{Lift} = \mathbb{L} &= qSc_L \\ \text{Drag} = \mathbb{D} &= qSc_D \\ \text{Pitching moment} = \mathbb{m} &= qScC_m \end{aligned} \quad (7)$$

where:

$q = \frac{1}{2}\rho v^2$ : is the dynamic pressure.

$S$ : is the characteristic area.

$c$ : is the mean aerodynamic chord.

$\alpha_{att}$ : is the angle of attack.

For the other coefficients, we have:

$$\begin{aligned} C_L(\alpha) &= C_L^\alpha \cdot \alpha_{att} \\ C_D(\alpha) &= C_D^0 + C_D^\alpha \cdot \alpha_{att}^2 \\ C_m(\alpha) &= C_m^\alpha \cdot \alpha_{att} \end{aligned} \quad (8)$$

The coefficient of drag  $C_D$  is composed of two members: the first  $C_D^0$  is insensitive to the angle of attack and is constant; the second one ( $C_D^\alpha \cdot \alpha_{att}^2$ ) is instead a function of the square of the angle. Note that the zero lift coefficient  $C_L^0 = 0$  because the wing profile that has been chosen for our project is symmetrical (type *Eppler 883*). Now is necessary to separate the contributions of the fuselage (body) and of the wings, for the three factors of lift, friction and pitching moment; so the expression is:

$$\begin{cases} \mathbb{L} = L^b + L^w \\ \mathbb{D} = D^b + D^w \\ \mathbb{m} = m^b + m^w \end{cases} \quad (9)$$

According to the Navier-Stokes (approximated) equations and the simplifications above cited, the previous system of equations becomes:

$$\begin{cases} \mathbb{L} = q\sqrt{V^3} \left\{ C_L^{b\alpha} \cdot \alpha_{att} + \frac{S_w}{\sqrt{V^3}} \cdot C_L^{w\alpha} \cdot \alpha_{att} \right\} \\ \mathbb{D} = q\sqrt{V^3} \left\{ \left[ C_D^{b0} + C_D^{b\alpha} \cdot \alpha_{att}^2 \right] + \frac{S_w}{\sqrt{V^3}} \left[ C_D^{w0} + C_D^{w\alpha} \cdot \alpha_{att}^2 \right] \right\} \\ \mathbb{m} = q\sqrt{V^3} \left\{ C_m^{b\alpha} \cdot \alpha_{att} - c_m \frac{l_{cb/ac_w} \cdot S_w}{c \cdot \sqrt{V^3}} \cdot C_L^{w\alpha} \cdot \alpha_{att} \right\} \end{cases} \quad (10)$$

where:

$S_w$  is the wing area.

$l_{cb/ac_w}$  is the distance between the mean aerodynamic and the center of buoyancy.

$c_m$  is a non-dimensional coefficient.

This parameter is necessary to know the exact attitude and therefore the  $\alpha_{att}$  to obtain a constant descent profile [66].

## 2.2.4. Gliding Forces

In order to allow the vehicle to glide, it is necessary to create a differential buoyancy force and therefore the balance is not null: from the buoyant force expression, the change in volume needed for the buoyancy engine for a full dive is calculated as:

$$\sum F_{Zunbalanced} = \Delta B_{BB} \neq 0 \quad (11)$$

In which  $\Delta B_{BB} \neq 0$  is the buoyancy force due to the difference of volume of the bladder:

$$\sum F_{Z_{unbalanced}} = \Delta B_{BB} = \frac{1}{2} \rho g \cdot \Delta V_{bladder} \quad (12)$$

where:

$\rho$  = Seawater density (average 1.025 kg/l).

$g$  = Gravity approx. to 9.81 m/s<sup>2</sup>.

$\Delta V_{bladder}$  = Volume difference of the bladder.

The relationship between difference volume of the bladder and buoyancy force is:

$$\Delta V_{bladder} = \frac{2}{\rho g} \cdot \Delta B_{BB} \quad (13)$$

### 2.2.5. Restoring Moment on the Vertical Plan

The position of the center of mass is given by:

$$r_{CG} = \frac{\int r \cdot \rho(r) dV}{\int \rho(r) dV} \quad (14)$$

where:

$\rho(r)$ : is the density.

$dV$ : is the considered volume.

$r$ : is the distance considered from the reference frame.

The gliders masses define above, is:

$$r_{CG} = \frac{\sum_i r_i \cdot W_i}{\sum_i W_i} = \frac{r_{BA} \cdot W_{BA} + r_{OT} \cdot W_{OT} + r_{GB} \cdot W_{GB}}{W_{BA} + W_{OT} + W_{GB}} \quad (15)$$

The vectorial balance of the forces becomes:

$$\begin{cases} \mathbb{F}_{gravitational} = W_{DW}(\mathbf{R}^T z) \\ \mathbb{F}_{buoyancy} = -V_{Displacement} g(\mathbf{R}^T z) \end{cases} \quad (16)$$

where

$V_{Displacement}$  is the volume of the drone (submerged).

$\mathbf{R}^T$  is the rotation function around the reference frame.

$z$  is the upward direction.

When the geometrical centre of the body is offset from the CG frame, the resulting torque  $\mathfrak{T}_G$  is given by:

$$\mathfrak{T}_G = r_{CG} \times W_{DW}(\mathbf{R}^T z) \quad (17)$$

The expression of  $r_{CG}$  is:

$$r_{CG} = \begin{pmatrix} x_{CG} \\ y_{CG} \\ z_{CG} \end{pmatrix} \quad (18)$$

The expression of  $\hat{r}_{CG}$  is:

$$\hat{r}_{CG} = \begin{pmatrix} 0 & -z_{CG} & y_{CG} \\ z_{CG} & 0 & -x_{CG} \\ -y_{CG} & x_{CG} & 0 \end{pmatrix} \quad (19)$$

Therefore, we have:

$$\mathfrak{T}_G = W_{DW} \cdot \hat{r}_{CG}(\mathbf{R}^T z) \quad (20)$$

According to which, when the body frame is coincident with the centre of the figure:

$$W_{DW} \cdot r_{CG} = r_{GB} \cdot B_{GB} + r_{BB} \cdot B_{BB} \quad (21)$$

Moreover, the resulting balancing torque is

$$\mathfrak{T}_G = (r_{GB} \cdot B_{GB} + r_{BB} \cdot B_{BB}) \cdot g(\mathbf{R}^T z) \quad (22)$$

This parameter is necessary to know the exact torque and therefore the position to which the servomechanism to move the battery pack will have to obtain a constant descent profile [67].

### 2.2.6. Uncertainty in the Depth Control

In this part, the problem of uncertainty in controlling the depth of the drone is examined. In the case where the drone has a very low vertical speed, due to the high viscosity of the water, the vehicle stops (and therefore stabilizes itself in the vertical plan) in a few centimeters of water, so this is not a problem.

Consider the case in which the drone is gliding, at a constant speed ( $V_z < 0$ ): at a depth of +5 m compared to the “target depth”, the bladder swells up to make the drone assume a neutral buoyancy. From a dynamic point of view, our simulations show us that the drone will behave like a mass-spring-damper system, whose temporal behavior is described in Equation (23) and visible in Figure 8 (blue line).

$$\begin{cases} z_{CG}(t) = \mathbb{Z}e^{-\zeta\omega_n t} \cdot \cos(\sqrt{1 - \zeta^2}\omega_n t - \Phi) \\ \omega_n = 2\pi f_n \end{cases} \quad (23)$$

The maximum precision in the measurement of depth is not given by the precision of the instrument, in this case a piezoelectric depth meter can be accurate up to 2.5 cm, but in the architecture of the drone. Because of all the possible attitudes of the vehicle, it is not known if the transducer is placed higher or lower than the centre of gravity: so, unless more than one transducer is installed (which is impractical) the only consideration is that the maximum distance at which the transducer should be placed from the centre of gravity is precisely 49.7 cm, so, the maximum range of precision obtainable from the instrument is:

$$\delta_z = 0.497 \text{ m} \quad (24)$$

As shown in Figure 8 (blue line) the natural dynamic stability of the vehicle, i.e., the oscillation within the error band, is obtained after a time  $\mathbb{T}_{normal} = 9.78 \text{ s}$  which is not acceptable (see Equation (25)). It is not acceptable for two reasons: first of all because of the long damping time of the oscillation; secondly for the overshoot of the “target depth”: the depth limit may have been placed not only by the type of mission but also by the nature (orography) of the seabed. Therefore, such behavior could lead to a collision of the vehicle with the seabed itself or a known obstacle, thus leading to damage:

$$\begin{cases} z_{CG}(t)_{normal} \leq \delta_z \\ \mathbb{T}_{normal} = 9.78 \text{ s} \end{cases} \quad (25)$$

The solution is to use the bladder as a “hydrostatic parachute” that changes the damping conditions of the system. In this case the simulation have evidenced that, if you place the bladder at maximum buoyancy (Figure 8—red line) shortly after reaching “+5” depth, the resulting behavior of the vehicle is visible in Figure 8 (azure line).

In this case the tolerance band is reached in  $\mathbb{T}_{compensated} = 4.85 \text{ s}$  (see Equation (26)), half the previous time and there is no danger of overshooting the depth, thus keeping us always in safe conditions:

$$\begin{cases} z_{CG}(t)_{compensated} \leq \delta_z \\ \mathbb{T}_{compensated} = 4.85 \text{ s} \end{cases} \quad (26)$$

From a mathematical point of view, the system changes the damping factor, increasing it considerably in fact,  $\zeta_{normal} < \zeta_{compensated}$ . The model parameters are shown in Table 1 below.

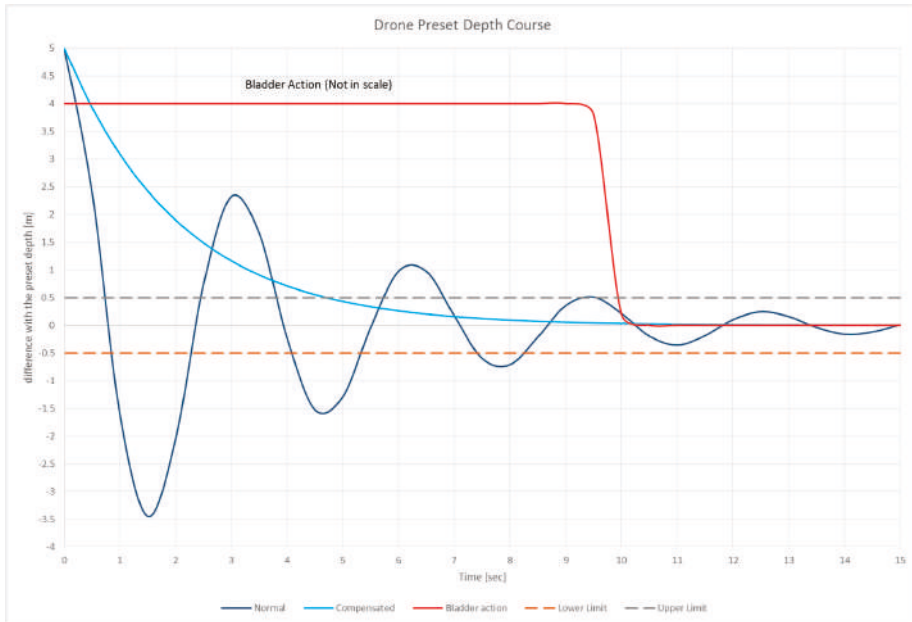


**Figure 8.** Drone depth dynamic behavior: in the blue line the normal (uncompensated) damping; the azure line the compensated behavior; dotted lines are the upper and lower limit. The red line (out of scale) is the bladder’s “hydrostatic chute” action.

**Table 1.** Model parameters.

$f_n$	$\zeta_{normal}$	$\zeta_{compensated}$	$Z$
1	0.0794	0.15779	4.972

### 2.2.7. Dynamic Simulation

In the section, we simulate the behavior of the Eppler 838 aerofoil and the fuselage to evaluate, before a detailed and expensive but more sophisticated 3D simulation, if the proportions and dimensions of the drone fall within the range of measures evaluated as a requirement. For this purpose, the program “JavaFoil—Analysis of Airfoils” [68] is used. JavaFoil is a program which uses several traditional methods for aerofoil analysis. The backbone of the program consists of two methods:

- The evaluation of the potential flow. The analysis is done with a higher order panel method (linear varying vorticity distribution) and it calculates the local, inviscid flow velocity along the surface of the aerofoil for any desired angle of attack.
- The evaluation of the boundary layer. The analysis is steps along the upper and the lower surfaces of the aerofoil, starting at the stagnation point, solves a set of differential equations to find the various boundary layer parameters, according to the integral method.

The equations and criteria for transition and separation are based on the procedures described by Eppler. A standard compressibility correction according to Karman and Tsien has been implemented to take moderate Mach number effects into account. Usually this means Mach numbers between zero and 0.5 [69–72].

The simulation shows the critical parameters for the hydrodynamic behaviour of the model: the results are given in Table 2 below [73–78].

**Table 2.** Body and wing critical parameters [Speed = 0.52 kts,  $R_e = 10^4$  and  $\alpha_{att} = 3.3^\circ$ ].

$C_L^{b_\alpha}$	$C_L^{w_\alpha}$	$C_D^{b_0}$	$C_D^{w_0}$	$C_D^{b_\alpha}$	$C_D^{w_\alpha}$	$C_m^{b_\alpha}$	$c_m$
0.3997	0.4085	0.01746	0.01676	0.00018	0.001515	0.005	0.4752

The trend of the flow lines with  $\alpha_{att} = 3.3^\circ$  around the body and the wing are visible in Figure 9a,b, below.

For completeness, in order to be able to express the induced resistance and the stall delay, the behavior of the aerofoil at different angles of attack is provided in Figure 10.

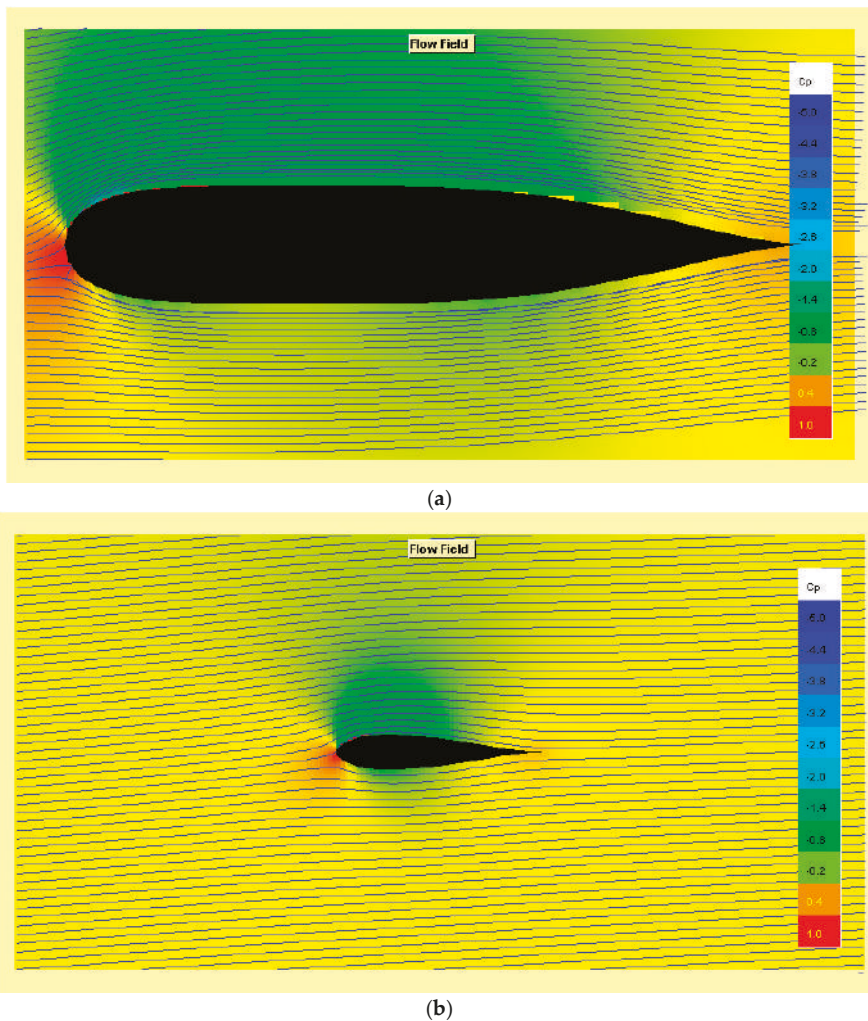


**Figure 9.** Flow field and pressure gradient of conditions: Speed = 0.52 kts,  $R_e = 10^4$  and  $\alpha_{att} = 3.3^\circ$ , (a) Body profile of the drone; (b) Eppler 838 Aerofoil.

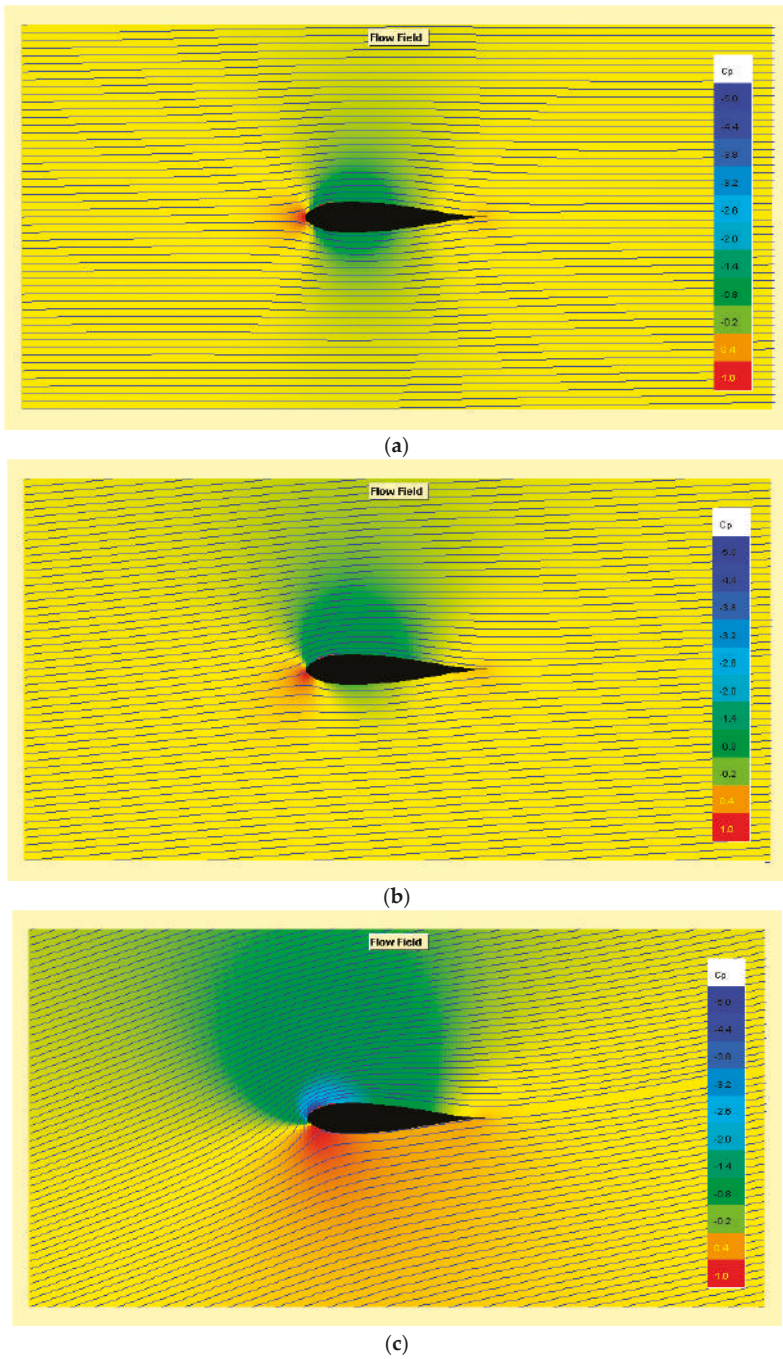


**Figure 10.** Flow field and pressure gradient of conditions (Speed = 0.52 kts,  $R_e = 10^4$ ) are shown at the following  $\alpha_{att}$ : (a)  $0.5^\circ$  (b)  $4.0^\circ$  (c)  $15.0^\circ$ .

### 3. Conclusions

This paper reports part of several preliminary studies of the Underwater Drones Group of the Università degli Studi “Roma Tre” Science Department and follows the route traced on several conference papers presented at the IEEE International Workshop on Metrology for the Sea (MetroSea); this part is dedicated to the design and engineering study of the part relating to the UAV buoyancy.

This paper highlights the large series of considerations and structural dimensions, going down in great detail, of the Underwater Glider Mk. III that is currently in an advanced development phase. The real novelties of this work are highlighted in the development due to two strong constraints that our group inserted during the design of this AUV: the first is to evaluate the project always under the most conservative (pessimistic) operating conditions; the second is to evaluate how any changes made to the subsystem in development (in our case the buoyancy *s/s*) is reflected (and forced) on all the other parts (or subsystems). All the results both from the partial simulations and from the construction and testing of subsystems will then be used in the operating vehicle.

The first section is dedicated to the design and engineering study of the part relating to the UAV buoyancy. In the first section, the architecture, the internal arrangement of the sub glider, the type of mission profile and the maximum requirements for the performances are broadly described. In the second part, the buoyancy system is described from an engineering-construction point of view: the solutions developed and implemented in a working prototype were illustrated.

The last part describes the mathematical requirements for sizing the vehicle. Firstly, the static requirements that are used to determine the mechanical and dimensional sizing of the buoyancy engine are examined. Then the dynamic stability (on the vertical plane) of the vehicle is analysed: this quantifies the forces involved during the “glide”. The trajectory is analysed to decide the attitude and the angle of attack: the latter is necessary, in stationary conditions, to determine the work point of the profile or the position of the profile in the diagram “*Cl vs. Alpha*”. In order to have a constant attitude, it is necessary to balance the moments in the vertical plane so that, once the wing profile is “started” and in progressive acceleration (i.e., while is nearly to reach the terminal velocity) the pitch up effects must be compensated by the movement of the centre of gravity. An evaluation of the uncertainty in the depth control is also provided.

Lastly, a simplified simulation is introduced in order to observe the hydrodynamic behaviour of the fuselage (limited to the profile) and of the aerofoil at different angles of attack, to highlight the stall characteristics.

**Author Contributions:** The authors have made an equal contribution in all the sections of this article.

**Funding:** This research received no external funding.

**Conflicts of Interest:** The authors declare no conflict of interest.

### References

1. Wood, S. Autonomous underwater gliders. In *Underwater Vehicles*; Chapter 26; Inzartsev, A.V., Ed.; In-Tech: Vienna, Austria, 2009; pp. 499–524.
2. Kayton, M.; Fried, W.R. *Avionics Navigation Systems*; Wiley: New York, NY, USA, 2007; ISBN 9780471547952.
3. Jenkins, S.A.; Humphreys, D.E.; Sherman, J.; Osse, J.; Jones, C.; Leonard, N.; Graver, J.; Bachmayer, R.; Clem, T.; Carroll, P.; et al. *Underwater Glider System Study*; Technical Report No. 53; Scripps Institution of Oceanography: San Diego, CA, USA, May 2003.
4. Graver, J.G. *Underwater Gliders: Dynamics, Control and Design*. Ph.D. Thesis, Princeton University, Princeton, NJ, USA, 2005.
5. Kan, L.; Zhang, Y.; Fan, H.; Yang, W.; Chen, Z. MATLAB-Based simulation of buoyancy-driven underwater glider motion. *J. Ocean Univ. Chin.* **2007**, *7*, 113–118. [[CrossRef](#)]
6. Woolsey, C.A.; Leonard, N.E. Stabilizing underwater vehicle motion using internal rotors. *Automatica* **2002**, *38*, 2053. [[CrossRef](#)]

7. Jekeli, C. *Inertial Navigation Systems with Geodetic Applications*; Walter de Gruyter Berlin: New York, NY, USA, 2001.
8. Smith, R.N.; Chao, Y.; Jones, B.H.; Caron, D.A.; Li, P.; Sukhatme, G.S. Trajectory Design for Autonomous Underwater Vehicles based on Ocean Model Predictions for Feature Tracking. In *Field and Service Robotics*; Springer: Berlin/Heidelberg, Germany, 2010; pp. 263–273, 2009.
9. Mitchell, B.; Wilkening, E.; Mahmoudian, N. Low cost underwater gliders for littoral marine research. In Proceedings of the American Control Conference (ACC), Seattle, WA, USA, 17–19 June 2013; pp. 1412–1417.
10. Meyer, D. Glider Technology for Ocean Observations: A Review. *Ocean Sci. Discuss.* **2016**, *2016*, 1–26. [[CrossRef](#)]
11. Davis, R.E.; Eriksen, C.C.; Jones, C.P. Autonomous buoyancy-driven underwater gliders. In *Technology and Applications of Autonomous Underwater Vehicles*; Griffiths, G., Ed.; Taylor & Francis: London, UK, 2002; pp. 37–58.
12. Wang, C.; Zhang, Z.; Gu, J.; Liu, J.; Miao, T. Design and Hydrodynamic Performance Analysis of Underwater Glider Model. In Proceedings of the 2012 International Conference on Computer Distributed Control and Intelligent Environmental Monitoring (CDCIEM), Hunan, China, 5–6 March 2012; pp. 225–227. [[CrossRef](#)]
13. De Francesco, E.; De Francesco, E.; De Francesco, R.; Leccese, F.; Cagnetti, M. A proposal to update LSA databases for an operational availability based on autonomic logistic. In Proceedings of the 2nd IEEE International Workshop on Metrology for Aerospace, MetroAeroSpace, Benevento, Italy, 4–5 June 2015; pp. 38–43. [[CrossRef](#)]
14. Eriksen, C.C.; Osse, T.J.; Light, R.D.; Wen, T.; Lehman, T.W.; Sabin, P.L.; Ballard, J.W.; Chiodi, A.M. Seaglider: A longrange autonomous underwater vehicle for oceanographic research. *IEEE J Oceanic Eng.* **2001**, *26*, 424–436. [[CrossRef](#)]
15. Rudnick, D.L.; Eriksen, C.C.; Fratantoni, D.M.; Perry, M.J. Underwater Gliders for Ocean Research. *Mar. Technol. Soc. J.* **2004**, *38*, 1.
16. Austin, R. *Unmanned Aircraft Systems*; Wiley: Hoboken, NJ, USA, 2010.
17. Graver, J.G.; Liu, J.; Woolsey, C.; Leonard, N.E. Design and Analysis of an Underwater Vehicle for Controlled Gliding. In Proceedings of the Conference on Information Sciences and Systems (CISS), Princeton, NJ, USA, 2–5 July 1998.
18. Leccese, F.; Cagnetti, M.; Giarnetti, S.; Petritoli, E.; Luisetto, I.; Tuti, S.; Đurović-Pejčev, R.; Đorđević, T.; Tomašević, A.; Bursić, V.; et al. A Simple Takagi-Sugeno Fuzzy Modelling Case Study for an Underwater Glider Control System. In Proceedings of the 2018 IEEE International Workshop on Metrology for the Sea; Learning to Measure Sea Health Parameters (MetroSea), Bari, Italy, 8–10 October 2018; pp. 262–267. [[CrossRef](#)]
19. Teledyne Webb Research. Slocum Electric Glider. Available online: <http://www.webbresearch.com/> (accessed on 1 February 2019).
20. Wood, S. State of Technology in Autonomous Underwater Gliders. *Mar. Technol. Soc. J.* **2013**, *47*, 5. [[CrossRef](#)]
21. Waldmann, C.; Kausche, A.; Iversen, M. MOTH-An underwater glider design study carried out as part of the HGF alliance ROBEX. In Proceedings of the 2014 IEEE/OES Autonomous Underwater Vehicles (AUV), Oxford, UK, 25–29 July 2014; pp. 1–3. [[CrossRef](#)]
22. Davis, R.E.; Webb, D.C.; Regier, A.; Dufour, J. The Autonomous Lagrangian Circulation Explorer (ALACE). *J. Atmos. Oceanic Technol.* **1992**, *9*, 264–285. [[CrossRef](#)]
23. Seo, D.C.; Gyungnam, J.; Choi, H.S. Pitching control simulation of an underwater glider using CFD analysis. In Proceedings of the Oceans—MTS/IEEE Kobe Techno-Ocean, Kobe, Japan, 8–11 April 2008; pp. 1–5.
24. Evans, C.D.; Riggins, R. The Design and Analysis of Integrated Navigation Systems Using Real INS and GPS Data. In Proceedings of the IEEE 1995 National Aerospace and Electronics Conference, Dayton, OH, USA, 22–26 May 1995.
25. Yu, J.; Zhang, F.; Zhang, A.; Jin, W.; Tian, Y. Motion Parameter Optimization and Sensor Scheduling for the Sea-Wing Underwater Glider. *IEEE J. Oceanic Eng.* **2013**, *38*, 243–254. [[CrossRef](#)]
26. Hussain, N.A.A.; Arshad, M.R.; Mohd-Mokhtar, R. Modeling and Identification of an Underwater Glider. In Proceedings of the 2010 International Symposium on Robotics and Intelligent Sensors (IRIS2010), Nagoya, Japan, 8–11 March 2010.
27. Bohenek, B.J. The Enhanced Performance of an Integrate Navigation System. In *A Highly Dynamic Environment*; Air Force Institute of Technology: Dayton, OH, USA, 1994.

28. Beard, R.W.; McLain, T.W. *Small Unmanned Aircraft—Theory and Practice*; Princeton University Press: Princeton, NJ, USA, 2012.
29. Petritoli, E.; Leccese, F.; Ciani, L. Reliability assessment of UAV systems. In Proceedings of the 4th IEEE International Workshop on Metrology for AeroSpace (MetroAeroSpace), Padua, Italy, 21–23 June 2017; pp. 266–270.
30. Watts, A.C.; Ambrosia, V.G.; Hinkley, E.A. Unmanned Aircraft Systems in Remote Sensing and Scientific Research: Classification and Considerations of Use. *Remote Sens.* **2012**, *4*, 1671–1692. [[CrossRef](#)]
31. Petritoli, E.; Leccese, F. Improvement of altitude precision in indoor and urban canyon navigation for small flying vehicles. In Proceedings of the 2nd IEEE International Workshop on Metrology for Aerospace (MetroAeroSpace 2015), Benevento, Italy, 4–5 June 2015; pp. 56–60. [[CrossRef](#)]
32. Andrade-Bustos, I.; Salgado-Jiménez, T.; García-Valdovinos, L.G.; Bandala-Sánchez, M. Stable Sliding PD Control for underwater gliders: Experimental results. In Proceedings of the Oceans 2016 MTS/IEEE Monterey, Monterey, CA, USA, 19–23 September 2016; pp. 1–7.
33. Pereira, A.; Heidarrson, H.; Caron, D.A.; Jones, B.H.; Sukhatme, G.S. A communication framework for the cost-effective operation of slocum gliders in coastal regions. In Proceedings of the 7th International Conference on Field and Service Robotics, Cambridge, MA, USA, 14–16 July 2009; pp. 1–10.
34. Skibski, C.E. Design of an Autonomous Underwater Glider focusing on External Wing Control Surfaces and Sensor Integration. Bachelor’s Thesis, Florida Institute of Technology, Melbourne, FL, USA, 2009.
35. Isa, K.; Arshad, M.R. An analysis of homeostatic motion control system for a hybrid-driven underwater glider. In Proceedings of the 2013 IEEE/ASME International Conference on Advanced Intelligent Mechatronics (AIM), Wollongong, Australia, 9–12 July 2013; pp. 1570–1575.
36. Küchemann, D. *The Aerodynamic Design of Aircraft*; Pergamon international library of science, technology, engineering, and social studie; Pergamon Press: Oxford, UK, 1978.
37. Parthasarathy, G.; Sree, D.S.; Manasa, B.L. Design Mathematical Modeling and Analysis of Underwater Glider. *Int. J. Sci. Res.* **2015**, *4*, 711–714.
38. Song, D.L.; Yao, L.L.; Wang, Z.Y.; Han, L. Pitching Angle Control Method of Underwater Glider Based on Motion Compensation. In Proceedings of the 2015 International Conference on Computational Intelligence and Communication Networks (CICN), Jabalpur, India, 12–14 December 2015; pp. 1548–1551.
39. Smith, R.N.; Schwager, M.; Smith, S.L.; Rus, D.; Sukhatme, G.S. Persistent Ocean Monitoring with Underwater Gliders Towards Accurate Reconstruction of Dynamic Ocean Processes. In Proceedings of the 2011 IEEE International Conference Robotics and Automation (ICRA), Shanghai, China, 9–13 May 2011; pp. 1517–1524.
40. Techy, L.; Tomokiyo, R.; Quenzer, J.; Beauchamp, T.; Morgansen, K. *Full Scale Wind Tunnel Study of the Seaglider Underwater Glider*; UWAA Technical Report UWAAATR-2010-0002; University of Washington: Seattle, WA, USA, September 2010.
41. Wilcox, J.S.; Bellingham, J.G.; Zhang, Y.; Baggeroer, A.B. Performance metrics for oceanographic surveys with autonomous underwater vehicles. *IEEE J Oceanic Eng.* **2001**, *26*, 711–725. [[CrossRef](#)]
42. Petritoli, E.; Giagnacovo, T.; Leccese, F. Lightweight GNSS/IRS integrated navigation system for UAV vehicles. In Proceedings of the 2014 IEEE International Workshop on Metrology for Aerospace (MetroAeroSpace), Benevento Italy, 29–30 June 2014; pp. 56–61. [[CrossRef](#)]
43. Webb, D.C.; Simonetti, P.J.; Jones, C.P. SLOCUM: An underwater glider propelled by environmental energy. *IEEE J Oceanic Eng.* **2001**, *26*, 447–452. [[CrossRef](#)]
44. Stommel, H. The Slocum Mission. *Oceanography* **1989**, *2*, 22–25. [[CrossRef](#)]
45. Sherman, J.; Davis, R.E.; Owens, W.B.; Valdes, J. The autonomous underwater glider “Spray”. *IEEE J Oceanic Eng.* **2001**, *26*, 437–446. [[CrossRef](#)]
46. Titterton, D.; Weston, J. *Strapdown Inertial Navigation Technology*, 2nd ed.; The Institution of Electrical Engineers and The American Institute of Aeronautics and Astronautics: Reston, VA, USA, 2004.
47. Jun, B.H.; Park, J.Y.; Lee, F.Y.; Lee, P.M.; Lee, C.M.; Kim, K.; Lim, Y.K.; Oh, J.H. Development of the AUV ‘SiMi’ and free running test in an ocean engineering basin. *Ocean Eng.* **2009**, *36*, 1. [[CrossRef](#)]
48. Leonard, N.E.; Graver, J.G. Model-Based feedback control of autonomous underwater gliders. *IEEE J. Ocean Eng.* **2001**, *26*, 4. [[CrossRef](#)]
49. Arima, M.; Ichihashi, N.; Ikebuchi, T. Motion characteristics of an underwater glider with independently controllable main wings. In Proceedings of the OCEANS 2008—MTS/IEEE Kobe Techno-Ocean, Kobe, Japan, 8–11 April 2008; pp. 1–7.

50. Roger, E.O.; Genderson, J.G.; Smith, W.S.; Denny, G.; Farley, P.J. Underwater acoustic glider. In Proceedings of the IEEE International Geoscience and Remote Sensing Symposium, Anchorage, AK, USA, 20–24 September 2004; pp. 2241–2244.
51. Woithe, H.C.; Kremer, U. A programming architecture for smart autonomous underwater vehicles. In Proceedings of the IEEE/RSJ International Conference on Intelligent Robots and Systems 2009—IROS 2009, St. Louis, MI, USA, 11–15 October 2009; pp. 4433–4438.
52. Woithe, H.C.; Tilkidjieva, D.; Kremer, U. *Towards a Resource-Aware Programming Architecture for Smart Autonomous Underwater Vehicles*; Technical Report, DCS-TR-637; Rutgers University: New Brunswick, NJ, USA, 2008.
53. Lennart, L. *System Identification Theory for the User*, 2nd ed.; Prentice Hall: Upper Saddle River, NJ, USA, 1999.
54. Petritoli, E.; Leccese, F. High accuracy attitude and navigation system for an autonomous underwater vehicle (AUV). *Acta IMEKO* **2018**, *7*, 3–9. [[CrossRef](#)]
55. Petritoli, E.; Leccese, F. A high accuracy navigation system for a tailless underwater glider. In Proceedings of the IMEKO TC19 Workshop on Metrology for the Sea, MetroSea 2017: Learning to Measure Sea Health Parameters, Naples, Italy, 11–13 October 2017; pp. 127–132.
56. Petritoli, E.; Leccese, F. A high accuracy attitude system for a tailless underwater glider. In Proceedings of the IMEKO TC19 Workshop on Metrology for the Sea, MetroSea 2017: Learning to Measure Sea Health Parameters, Naples, Italy, 11–13 October 2017; pp. 7–12.
57. DSIAC. Reliability of UAVs and Drones. Available online: <https://www.dsiac.org/resources/journals/dsiac/spring-2017-volume-4-number-2/reliability-uavs-and-drones> (accessed on 28 February 2019).
58. Etkin, B. *Dynamic of Flight*; John Wiley and Sons: Hoboken, NJ, USA, 1959.
59. Tan, X.; Kim, D.; Usher, N.; Laboy, D.; Jackson, J.; Kapetanovic, A.; Rapai, J.; Sabadus, B.; Zhou, X. An Autonomous Robotic Fish for Mobile Sensing. In Proceedings of the 2006 IEEE/RSJ International Conference on Intelligent Robots and Systems, Beijing, China, 9–15 October 2006; pp. 5424–5429.
60. Smith, R.N.; Pereira, A.; Chao, Y.; Li, P.P.; Caron, D.A.; Jones, B.H.; Sukhatme, G.S. Autonomous Underwater Vehicle trajectory design coupled with predictive ocean models: A case study. In Proceedings of the 2010 IEEE International Conference on Robotics and Automation (ICRA), Anchorage, AK, USA, 4–8 May 2010; pp. 4770–4777.
61. Petritoli, E.; Leccese, F.; Cagnetti, M. A High Accuracy Buoyancy System Control for an Underwater Glider. In Proceedings of the 2018 IEEE International Workshop on Metrology for the Sea: Learning to Measure Sea Health Parameters (MetroSea), Bari, Italy, 8–10 October 2018; pp. 257–261. [[CrossRef](#)]
62. Techy, L.; Kristi Morganseny, A.; Woolseyz, C.A. Long-baseline acoustic localization of the Seaglider underwater glider. In Proceedings of the American Control Conference (ACC) 2011, San Francisco, CA, USA, 29 June–1 July 2011; pp. 3990–3995.
63. Hussain, N.A.A.; Ali, S.S.A.; Saad, M.N.M.; Nordin, N. Underactuated nonlinear adaptive control approach using U-model for multivariable underwater glider control parameters. In Proceedings of the 2016 IEEE International Conference on Underwater System Technology: Theory and Applications (USYS), Penang, Malaysia, 13–14 December 2016; pp. 19–25. [[CrossRef](#)]
64. Yu, P.; Zhao, Y.; Wang, T.; Zhou, H.; Su, S.; Zhen, C. Steady-state spiral motion simulation and turning speed analysis of an underwater glider. In Proceedings of the 2017 4th International Conference on Information Cybernetics and Computational Social Systems (ICCSS), Dalian, China, 24–26 July 2017; pp. 372–377.
65. Bloch, T.; Krishnaprasad, P.S.; Leonard, N.; Murray, R. Jerrold Eldon Marsden [Obituaries]. *Control Syst. IEEE* **2011**, *31*, 105–108.
66. Williams, C.D. AUV systems research at the NRC-IOT: An update. In Proceedings of the Underwater Technology 2004—UT '04. 2004 International Symposium on, Taipei, Taiwan, 20–23 April 2004; pp. 59–73.
67. Jing, D.; Haifeng, W. System health management for unmanned aerial vehicle: conception, state-of-art, framework and challenge. In Proceedings of the Electronic Measurement & Instruments (ICEMI). In Proceedings of the 2013 IEEE 11th International Conference, Harbin, China, 16–19 August 2013; Volume 2, pp. 859–863.
68. Javafoil—Analysys of Airfolis. Available online: <https://www.mh-aerotoools.de/airfoils/javafoil.htm> (accessed on 15 February 2019).
69. Vogeltanz, T. A Survey of Free Software for the Design, Analysis, Modelling, and Simulation of an Unmanned Aerial Vehicle. *Arch. Comput. Meth. Eng.* **2016**, *23*, 449. [[CrossRef](#)]

70. Vogeltanz, T.; Jašek, R. Free software for the modelling and simulation of a mini-UAV. In Proceedings of the Mathematics and Computers in Science and Industry, Varna, Bulgaria, 13–15 September 2014; pp. 210–215.
71. Jodeh, N.; Blue, P.; Waldron, A. Development of small unmanned aerial vehicle research platform: Modeling and simulating with flight test validation. In Proceedings of the AIAA Modeling and Simulation Technologies Conference and Exhibit, Keystone, CO, USA, 21–24 August 2006; p. 6261.
72. Mueller, T.J.; DeLaurier, J.D. Aerodynamics of small vehicles. *Annual review of fluid mechanics* **2003**, *35*, 89–111. [[CrossRef](#)]
73. Fabiani, P.; Fuertes, V.; Piquereau, A.; Mampey, R.; Teichteil-Königsbuch, F. Autonomous flight and navigation of VTOL UAVs: From autonomy demonstrations to out-of-sight flights. *Aerosp. Sci. Technol.* **2007**, *11*, 183–193. [[CrossRef](#)]
74. Wu, N.; Wu, C.; Ge, T.; Yang, D.; Yang, R. Pitch Channel Control of a REMUS AUV with Input Saturation and Coupling Disturbances. *Appl. Sci.* **2018**, *8*, 253. [[CrossRef](#)]
75. Hahn, A. Vehicle sketch pad: A parametric geometry modeller for conceptual aircraft design. In Proceedings of the 48th AIAA Aerospace Sciences Meeting Including the New Horizons Forum and Aerospace Exposition, Orlando, FL, USA, 4–7 January 2010; p. 657. [[CrossRef](#)]
76. Wang, T.; Wu, C.; Wang, J.; Ge, T. Modeling and Control of Negative-Buoyancy Tri-Tilt-Rotor Autonomous Underwater Vehicles Based on Immersion and Invariance Methodology. *Appl. Sci.* **2018**, *8*, 1150. [[CrossRef](#)]
77. Boussalis, H.; Valavanis, K.; Guillaume, D.; Pena, F.; Diaz, E.U.; & Alvarenga, J. Control of a simulated wing structure with multiple segmented control surfaces. In Proceedings of the 2013 21st Mediterranean Conference IEEE Control & Automation (MED), Crete, Greece, 25–28 June 2013; pp. 501–506.
78. Wang, T.; Wang, J.; Wu, C.; Zhao, M.; Ge, T. Disturbance-Rejection Control for the Hover and Transition Modes of a Negative-Buoyancy Quad Tilt-Rotor Autonomous Underwater Vehicle. *Appl. Sci.* **2018**, *8*, 2459. [[CrossRef](#)]



© 2019 by the authors. Licensee MDPI, Basel, Switzerland. This article is an open access article distributed under the terms and conditions of the Creative Commons Attribution (CC BY) license (<http://creativecommons.org/licenses/by/4.0/>).



Article

# Estimation of Wave Characteristics Based on Global Navigation Satellite System Data Installed on Board Sailboats

Paolo De Girolamo <sup>1</sup>, Mattia Crespi <sup>1</sup>, Alessandro Romano <sup>1</sup>, Augusto Mazzoni <sup>1</sup>, Marcello Di Risio <sup>2,\*</sup>, Davide Pasquali <sup>2</sup>, Giorgio Bellotti <sup>3</sup>, Myrta Castellino <sup>1</sup> and Paolo Sammarco <sup>4</sup>

<sup>1</sup> “Sapienza”, University of Rome, DICEA, Via Eudossiana, 18, 00184 Roma, Italy; paolo.degirolamo@uniroma1.it (P.D.G.); mattia.crespi@uniroma1.it (M.C.); alessandro.romano@uniroma1.it (A.R.); augusto.mazzoni@uniroma1.it (A.M.); myrta.castellino@uniroma1.it (M.C.)

<sup>2</sup> Department of Civil, Construction-Architectural and Environmental Engineering (DICEAA)—Environmental and Maritime Hydraulic Laboratory (Llam), University of L’Aquila, 67100 L’Aquila, Italy; davide.pasquali@univaq.it

<sup>3</sup> Engineering Department, Roma Tre University, Via V. Volterra, 62, 00146 Roma, Italy; giorgio.bellotti@uniroma3.it

<sup>4</sup> Department of Civil Engineering and Computer Science, University of Rome “Tor Vergata”, DICIL, Via del Politecnico, 1, 00133 Roma, Italy; sammarco@ing.uniroma2.it

\* Correspondence: marcello.dirisio@univaq.it

Received: 15 March 2019; Accepted: 14 May 2019; Published: 18 May 2019

**Abstract:** This paper illustrates a methodology to get a reliable estimation of the local wave properties, based on the reconstruction of the motion of a moving sailboat by means of GNSS receivers installed on board and an original kinematic positioning approach. The wave parameters reconstruction may be used for many useful practical purposes, e.g., to improve of autopilots, for real-time control systems of ships, to analyze and improve the performance of race sailboats, and to estimate the local properties of the waves. A Class 40 oceanic vessel (ECO40) left from the port of “Riva di Traiano” located close to Rome (Italy) on 19 October 2014 to perform a non-stop sailing alone around the world in energy and food self-sufficiency. The proposed system was installed on ECO40 and the proposed method was applied to estimate the wave properties during a storm in the Western Mediterranean Sea. The results compared against two sets of hindcast data and wave buoy records demonstrated the reliability of the method.

**Keywords:** GPS data analysis; off-shore wave climate; sailboat; ship motions; wave characteristics

---

## 1. Introduction

Estimation of ship motions and wave properties from a traveling ship is of utmost importance for many ocean engineering applications [1], for example: (i) to improve the performance of autopilots and control systems of ships [2] or in general of floating structures [3]; (ii) to provide real-time wave data for Global Forecasting Systems (GFS) numerical models and for the calibration/validation of wave forecasting/hindcasting models (e.g., [4]), etc.; and (iii) to analyze the performance of a race sailboat, i.e., to derive actual velocity polar curves in the presence of waves and to correct wind measurements carried out onboard. As far as the estimation of the wave properties is concerned, a possible approach is to derive the parameters of interest directly on the basis of the ship motion, taking into account the dynamic ship frequency response function (e.g., [1,5–7]).

In the last years, the measurement of directional wave spectra on the basis of moving ships kinematic has been extensively studied (e.g., [8,9]). Some approximated solutions of the main theoretical problem arising from the transformation of encounter frequencies measured onboard into the true wave frequencies have been derived. This problem is known as the “triple-valued function problem”, which is due to the non-linear Doppler shift effect induced by frequency dispersive waves (e.g., [10,11]). Approximated solutions have been obtained by using both parametric methods, which assume the shape of the wave spectrum, and non-parametric (stochastic) methods, where the spectrum shape is not prescribed a priori [1,11,12].

Only in the last ten years, the GNSS technology has been applied on floating buoys for measuring directional wave spectra [13,14]. The advantages, as well as the disadvantages, of using GNSS buoys were pointed out by Herbers et al. [14]. On the other hand, onboard measurements of ship-motion is normally carried out by means of accelerometers used for standard pitch/roll directional wave buoys [10,11,15–17].

This paper describes the estimation of ship motion using GPS receivers, installed on a traveling sailboat for the evaluation of the local wave properties. It has to be stressed that the use of GNSS on an offshore traveling sailboat is challenging. Indeed, the distance of the moving GNSS receivers installed onboard (i.e., rover receivers) from reference static receivers of known coordinates (i.e., base stations) should not exceed few tens of kilometers. Indeed, Herbers et al. [14] used off-the-shelf GPS receivers able to provide positions with accuracy limited to a few meters, mentioning that sub-meter accuracy is achievable with post-processing methodology only. In this work, we propose to adopt the original methodology Kin-Vadase, presented and widely validated by Branzanti et al. [18], able to provide accuracies at decimeter level and at few millimeters/second for positions and velocities directly on-board, respectively (no need of external data, such as differential positioning or precise point positioning) and in real time. With respect to the work of De Girolamo et al. [19], this paper deals with a more detailed description of the methods and extends the results.

The paper is structured as follows. Section 2 illustrates the methodology to analyze the GNSS data and to use them in order to reconstruct the boat motion and, then, the wave parameters. Section 3 illustrates the real scale ECO40 sailboat used to test the proposed methodology during a non-stop sailing alone around the world. Section 4 discusses the results and demonstrates the reliability of the proposed method by comparing the estimated wave parameters against measured and hindcast data. Concluding remarks close the paper.

## 2. Methods

During offshore oceanic sailing, GPS measurements cannot be corrected using on land reference receivers, or a GNSS (Global Navigation Satellite System) network, since the distance between rovers and reference station should not be larger than few tens of kilometers. To solve this problem, in the present work, two GPS data processing techniques have been applied, by using a novel approach. The processed data provided by the GPS receivers have been used to compute the boat motion and to estimate the waves properties faced by the sailboat during its navigation around the world. This sections aims at detailing the proposed methods.

### 2.1. Analysis of Gnss Data

The GPS raw code and phase observations on both L1 and L2 frequencies were acquired by each GPS antenna/receiver system (in the following referred to as “receiver”) with a sampling rate of 2 Hz. The raw observations were stored on a flash-card by each receiver. The data analysis was carried out in post-processing after the recovery of the flash-cards. The analysis carried out in the post processing described in the following, however, can be carried out in real-time onboard of the sailboat. The post-processing was carried out by employing two different techniques: the Variometric approach and the Moving Base Kinematic.

The Variometric Approach for Displacements Analysis Standalone Engine (VADASE) is an innovative GPS data processing approach proposed in the recent past [20,21]. The approach is based on timing single differences of carrier phase observations continuously collected using a standalone GPS receiver and on standard GPS broadcast products (orbits and clocks) that are available in real-time. Therefore, one receiver works in standalone mode and the epoch-by-epoch displacements (equivalent to velocities) are estimated. In this work, a kinematic extension of the Variometric approach (Kin-VADASE) developed specifically for the navigation field was used.

A second approach was used. Indeed, the most widely used technique in GPS kinematic positioning is based on the using of two devices: the rover moving receiver and a reference static receiver of known coordinates. To obtain high accuracy results, the distance between the rover and the reference receiver should not exceed few tens of kilometers. Thus, it is almost impossible to apply this technique in off-shore navigation, due to the lack of close reference receivers availability. Nevertheless, in this work, we present an innovative application of differential kinematic positioning applied to a reference moving (hereinafter referred to as Moving Base Kinematic, MBK). With respect to this reference moving receiver, it was possible to estimate, epoch by epoch, the positions of another receiver. This technique does not allow defining the absolute position of the receiver but only the relative one, which is very accurate, since the distance between each couple of receivers is known. The results of the GPS data post processing may then be used to reconstruct the six Degrees of Freedom (hereinafter referred to as 6DOFs) boat motion and to estimate the wave parameters encountered by sailing boats (i.e., significant wave height and mean wave direction). Actually, only heave, roll and pitch motions are described as they are needed to estimate the waves parameters.

## 2.2. Boat Motion Reconstruction

This subsection describes the method used to reconstruct the 6DOFs boat motion by using the two approaches described in Section 2.1. The two approaches have been used in a complementary way. In the following, the methods used to compute each degree of freedom of the boat from GPS measurements needed to estimate the wave parameters are described. The boat 6DOFs are referred in the following to the center of the triangle defined by the three GPS positions and not to the center of gravity of the boat. However, a simple translation may be applied to the results in order to express the motion of the boat with respect to its center of gravity, as usual. It has to be stressed, however, that this work aims at estimating the wave parameters and that the 6DOF boat motion is used to reach the goal.

### 2.2.1. Heave

To compute the boat heave, it is necessary to use a technique able to provide the absolute vertical position of the boat. Nevertheless, the up-velocity component provided by Kin-VADASE method is subjected to bias, mainly related to the number of visible satellites and to their position with respect to the GPS antennas location. A sensitivity analysis was performed by using different numerical techniques (i.e., first order, Simpson's rule, etc.) to minimize the integration error. It is worth noting that heave motion should exhibit a mean value very close to zero. Nevertheless, whatever the used numerical technique, the bias on the velocities gives rise to a vertical movement of the antenna due to low frequency drift related to the numerical integration. To eliminate the bias, a high pass filter was used. The high pass filter was applied to the vertical movement time history obtained by integrating over time the up-velocity component provided by a GPS antenna. The cut-off frequency was chosen large enough to avoid the low frequency drift related to the numerical integration, but small enough to analyze both the sea and the swell wave features.

### 2.2.2. Roll

For the computation of the boat roll motion, it is not necessary to use a technique able to provide the absolute position of the boat, as roll may be obtained by means of the relative vertical differences between two points located along an axis orthogonal to the main longitudinal axis of the boat.

The roll angle is not characterized by a zero mean value mainly because of two reasons. The first one is related to the wind acting on the sail and on the boat hull, which causes the heeling of the sailboat. It is a function of the wind speed and of the sails trim and configuration. The second one is due to the movable weight (i.e., ballast, not used sails, spare equipment, etc.), which are moved by the crew in order to reduce the heeling induced by the wind action. The heeling angle may be obtained by calculating the mean total roll angle value over a time longer than the waves encountered periods.

### 2.2.3. Pitch

The computation of the pitch motion, as for the roll, can be carried out by using the moving base kinematic (MBK) technique. For this parameter, two GPS receivers located along the main longitudinal axis of the sailboat should be used. Nevertheless, other antennas configurations could be used (see Section 3). In this case, it has to be stressed that the signals may be affected by the influence of the roll motion. To get the estimation of the pitch signal but the roll component, a mean signal (i.e., the actual pitch) can be computed (see Section 4).

### 2.3. Wave Parameters Estimation

The synthetic parameters of the waves faced by sailboats can be derived from the heave, roll and pitch motions. First, the transfer function between the boat and the sea surface movements has to be evaluated and applied to the time series estimated on the basis of GNSS data. Then, the duration of the time window to be analyzed needs to be defined. Herein, time windows of 30 min were considered. Indeed, this duration, which is typical for standard analysis of the free surface elevation signals as measured from conventional wave buoys, is considered to be long enough to properly describe, in a statistical sense, the considered sea state and short enough for considering the wave features to be stationary [22]. On the one hand, the significant wave height may be directly inferred from the heave motion by performing standard time and frequency domain analyses. On the other hand, the directional spectrum may be estimated by using the Direct Fourier Transform Method (i.e., by means of the DIWASP package, e.g., [23]) applied to the heave, pitch and roll signals without taking into account the Doppler shift effect due to the sailboat traveling. It has to be stressed that the influence of the waves upon the roll angle may be obtained by subtracting the heeling angle from the total measured roll angle, obtaining in this way a signal characterized by a mean value which is equal to zero.

## 3. The Experimental Sailboat ECO40

The considered sailboat is a small oceanic race boat length overall of 12.0 m) characterized by a very light displacement. She is a Class 40 oceanic vessel named ECO40, which left from the port of “Riva di Traiano” located close to Rome (Italy) on 19 October 2014 to perform a non-stop sailing alone around the world in energy and food self-sufficiency. The boat route goes through the Gibraltar Strait, then descends the Atlantic Ocean and sailing around the Antarctic, at a mean latitude of 50° S, from west to east, rounding the famous capes of the world: Cape of Good Hope, Cape Leeuwin and Cape Horn. Finally, it ascends the Atlantic Ocean, passing again the Strait of Gibraltar and coming back to homeport [24,25].

The boat was equipped with three high precision GPS receivers (rovers), provided by Leica Geosystem, for measuring the movements of the boat. An ad hoc survey was performed just after their installation in order to know the positions of the GPS antennas needed to infer the three-dimensional position and attitude of the boat as a rigid body.

The three geodetic class GPS antenna/receiver systems are able to acquire code and phase observations on both L1 and L2 frequencies. The GPS antennas were installed on board ECO40, as shown in Figure 1. Two antennas were mounted on the stern roll bar (they are indicated as GPS Stern-right and GPS Stern-left in the figure) and one antenna (GPS Bow) was installed along the main axis of the boat, close to the entrance and protected by a small fiberglass structure. The positions of

the three GPS antennas were at the vertices of an isosceles triangle, as described in the Figure 1. The proposed method was applied to three couples of receivers deployed on board (Figure 1): GPS Bow–GPS Stern-right; GPS Bow–GPS Stern-left, and GPS Stern-right–GPS Stern-left.

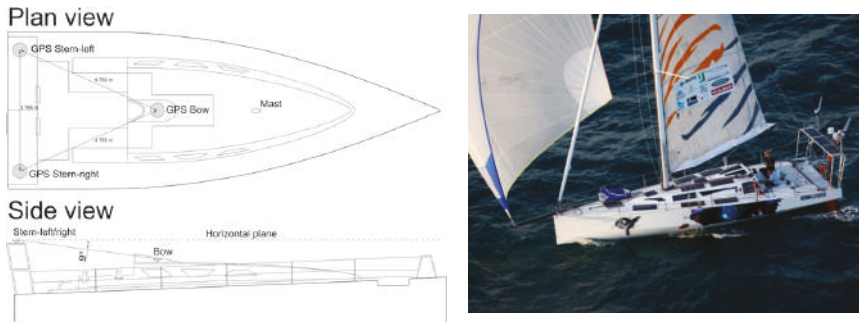


**Figure 1.** Plan view of the sailboat ECO40 and of the three GPS antennas (Top Left) and side view of the sailboat (Bottom Left); and (Right) a picture of the sailboat ECO40 during a test.

#### 4. Results

When ECO40 left from the Italian Port Riva di Traiano (Italy) directed to Gibraltar Strait (on 19 October 2014), the weather forecasts suggested that, within the next 24/48 h, the first seasonal front of cold air was expected to induce Mistral winds with speed exceeding 40 knots, blowing from the Gulf of Lion [24]. ECO40 was able to reach the Asinara Island and to follow the route towards the Balearic Islands before the arrival of the main storm: the sailboat faced the storm running on the quarter. The route between the Asinara Island and the Balearic Islands is represented in Figure 2. The figure also provides information on the travel times.

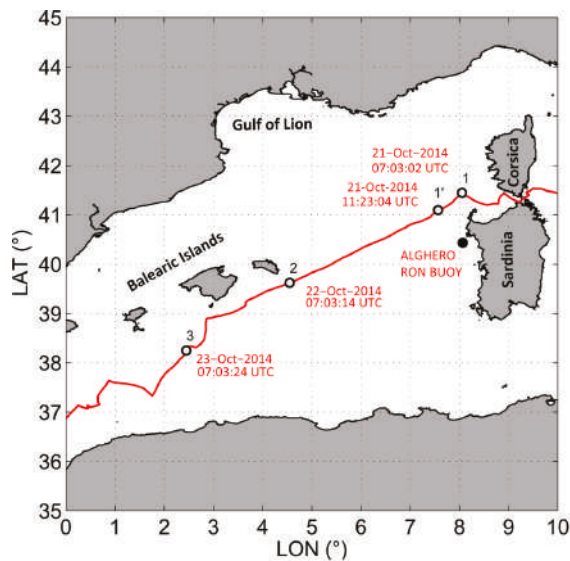
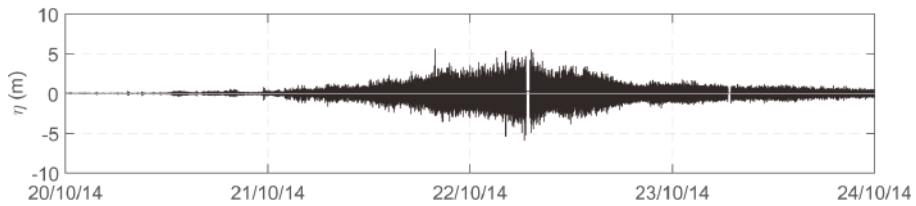


**Figure 2.** The route in the western Mediterranean Sea followed by ECO40. The empty dots refer to four points of interest along the route and the black dot identifies the position of the Alghero wave buoy.

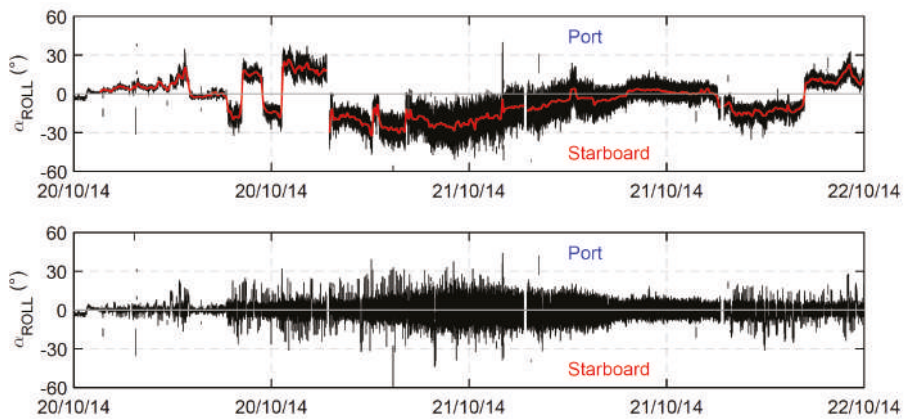
This section aims at illustrating and discussing the results obtained by means of the proposed methodology described in Section 2.

The boat heave time series was obtained by computing the instantaneous mean values of the three filtered heave time series, as obtained by each of the three GPS antennas. Figure 3 shows an example of the calculated boat heave signal for a time window of four days.

The roll motion angle was computed by using the moving base kinematic (MBK) applied to the relative Up position of the couple of Stern-GPSs. Figure 4 shows the roll angle during four days of navigation of ECO40. As expected, the analysis revealed that the measured roll angle was not characterized by a zero mean value. The red line in Figure 4 (top) shows the heeling angle computed over a time of 10 min. It is possible to identify the route changes of the boat which take place when the heeling angle changes from positive (port) to negative values (starboard) or vice versa. The influence of the waves upon the roll angle obtained by subtracting the heeling angle to the total measured roll angle is also shown in Figure 4 (bottom).

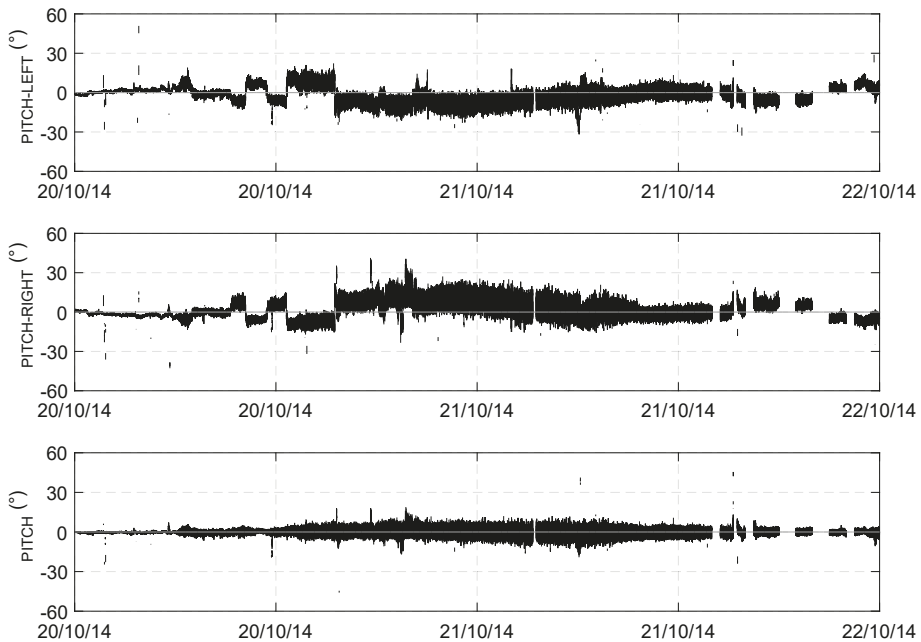


**Figure 3.** Example of the boat heave time series over a time window of four days, obtained by calculating the instant mean values of the three filtered heave time series as obtained by each GPS antenna.



**Figure 4. (Top)** Example of the total measured roll angle time series (black line) over a time window of four days. The red line refers to the heeling angle calculated by averaging over 10 min. **(Bottom)** The roll angle obtained by subtracting the heeling angle to the total measured roll angle.

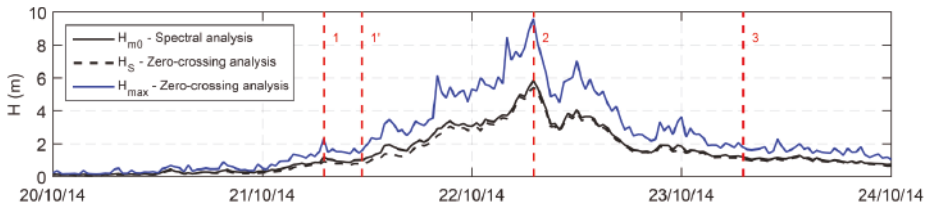
As far as the pitch motion is considered, it has to be observed that two GPS receivers located along the main longitudinal axis of the sailboat were not available and therefore a direct estimation of the pitch could not be obtained. Two couples of GPS receivers were therefore considered: the bow–stern-right and the bow–stern-left. Figure 5 shows an example of the 2 Hz time series of the pitch angle obtained directly from the relative up position of each couple of GPS measurements. The time series were evaluated with respect to the local horizontal plane. Figure 5 (top) shows the time series of the pitch angle obtained by using the bow–stern-left GPS couple, while Figure 5 (middle) represents the same quantity as obtained by using the bow–stern-right GPS couple. The figure shows that both signals were contaminated by a component of the roll motion because the two axes passing for each couple of GPS (bow–stern right and bow–stern left) were not parallel to the main boat axis. Furthermore, the comparison of Figure 5 (top and middle) shows that the two signals are in phase opposition because of the changing of the reference GPS. To obtain the pitch signal depurated by the roll component, a mean signal obtained from the two couple bow–stern right and the bow–stern left was computed (Figure 5, bottom).



**Figure 5.** Time series of the angle obtained by using the bow–stern-left GPS couple (**Top**); and the same quantity as obtained by using the bow–stern-right GPS couple (**Middle**) over a time window of four days. (**Bottom**) Time series of the mean signal (pitch) obtained from the two couples bow–stern right and the bow–stern left over a time window of four days.

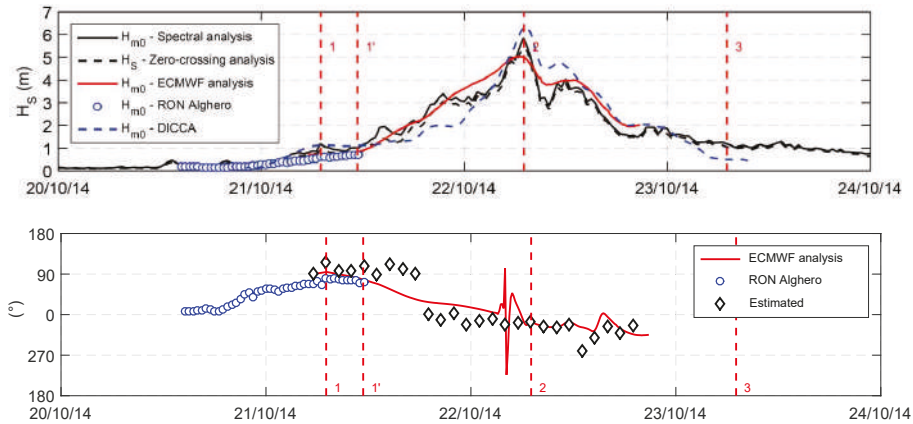
The features of the waves faced by the sailboat during the Gulf of Lion event were derived from the sailboat heave, roll and pitch motions. Since ECO40 is an ultra-light displacement boat (she has full loaded displacement of about 4700 kg, a length of about 12.0 m and a maximum breadth of 4.5 m), it was assumed that the sailboat follows the sea surface, thus assuming a unitary transfer function between the boat and sea surface movements (i.e., the response amplitude operator is the unit matrix).

Figure 6 shows the significant wave height time series of the storm obtained from the heave signal by using both the zero-crossing analysis ( $H_{1/3}$ ) and the frequency spectrum analysis ( $H_{m0}$ ) carried out in the encountered frequency domain. The maximum zero crossing wave height ( $H_{max}$ ) is also represented. The maximum values obtained during the storm for  $H_{1/3}$  and for  $H_{m0}$  were, respectively, 5.84 m and 5.42 m, while  $H_{max}$  was of 9.6 m. The vertical dashed lines refer to four points of interest along the route (as shown in Figure 2).



**Figure 6.** Significant wave height obtained from the heave by using zero crossing analysis (black dashed line) and frequency spectrum analysis (black line). The maximum wave height is reported as well (blue line). The vertical red dashed lines refer to the four points of interest along the route (as shown in Figure 2).

To assess the accuracy of the estimated wave parameters, Figure 7 shows the comparison between the significant wave height and mean wave direction as: (i) measured by the Alghero RON wave buoy; (ii) estimated by the ECMWF analysis; and (iii) estimated by DICCA for a grid point close to the buoy position. It has to be stressed that this study aimed at estimating the wave parameters based on GNSS data analysis (see Section 2). Therefore, only the synthetic wave parameters were compared to the results of other research works, being the original methodology Kin-VADASE widely validated (see Section 2, [18]) even if applied to a different environment. The Alghero wave buoy belongs to the “RON-Rete Ondametrica Nazionale” (Italian Wave Measurements Network [26]), managed by ISPRA up to 2014 and now dismissed after about 23 years; the buoy was located offshore the northwest coast of Sardinia and it was exposed to the waves generated by the storm at hand. The six-hourly hindcast wave data provided in analysis by ECMWF (European Centre for Medium-Range Weather Forecasts) and the hourly wave hindcast data provided by DICCA (Department of Civil, Chemical and Environmental Engineering, University of Genoa, Italy), covering 36 (1979–2014) years over the Mediterranean Sea [27] were also considered. were interpolated in time and in space by means of bi-linear technique. Since the buoy was operating at a fixed position, the comparison between the buoy wave data and the ones measured onboard was performed just for the time window in which the two measurements can be reasonably compared. The analysis revealed that the synthetic parameters reconstructed on the basis of sailboat motion was in close agreement with the DICCA data. On the other hand, the ECMWF data seemed to underestimate the storm peak, as already outlined by previous work e.g., [4], likely due to the time and spatial resolution of the hindcast data. As far as the mean wave direction is concerned, the accuracy of the proposed method was reasonable.



**Figure 7.** (Top) Comparison between the significant wave height measured onboard and the available wave data; and (Bottom) comparison between the mean spectral wave direction as estimated by means of the proposed method and the same quantity as obtained by the ECMWF data (red line) and Alghero wave buoy data (blue dots). The red dashed lines refer to four points of interest along the route (as shown in Figure 2).

## 5. Concluding Remarks

A method to reconstruct the movements of a sailboat in order to get a reliable estimate of wave parameters, using GPS receivers, is presented. It is based on the combined approach of the Kin-VADASE and Moving Base Kinematic techniques. The proposed method was applied to the records collected onboard the ECO40 sailboat during a storm in the Western Mediterranean Sea. Three GPS antennas were deployed on the sailboat. Their positions were measured by means of a survey performed when they were installed. Therefore, the three-dimensional locations of the GPS antennas suffice to infer the three-dimensional position and attitude of the boat as a rigid body, hence to reconstruct wave parameters. A fourth GPS antenna could be considered to improve the reliability of the estimation of the position and attitude of the boat.

Wave properties as derived on the basis of the estimated boat movements were compared to available wave data. It appears that the wave properties were calculated with a high degree of accuracy. Note that the main aim of this work was the estimation of wave parameters, hence the GNSS data analysis was not directly validated. Of course, the good agreement between estimated and available data may be viewed as an indirect validation of GNSS data analysis as well.

In general, the techniques proposed in this paper appear to be suitable to estimate the 6DOFs movements of sailboats navigating offshore, where onshore reference receivers or GNSS network cannot be used to correct GPS errors. The motion of the boat can provide quantitative information for many important practical applications, such as the improvement of autopilots, the analysis and the optimization of ship performances, and the estimation of local wave properties. Furthermore, it can be used to correct wind measurements carried out onboard sailboats.

**Author Contributions:** Conceptualization, P.D.G., M.C. (Mattia Crespi) and A.R.; Methodology, P.D.G., M.C. (Mattia Crespi), A.R., A.M., M.D.R., D.P., G.B., M.C. (Myrta Castellino) and P.S.; Software, A.R., A.M. and D.P.; Validation, P.D.G., M.C. (Mattia Crespi); Formal Analysis, P.D.G., M.C. (Mattia Crespi), A.R., A.M., M.D.R., D.P., G.B., M.C. (Myrta Castellino) and P.S.; Investigation, P.D.G., M.C. (Mattia Crespi), A.R., A.M., M.D.R., D.P., G.B., M.C. (Myrta Castellino) and P.S.; Resources, P.D.G. and M.C. (Mattia Crespi); Data Curation, A.R. and A.M.; Writing—Original Draft Preparation, P.D.G., M.C. (Mattia Crespi), A.R., A.M., M.D.R., D.P., G.B., M.C. (Myrta Castellino) and P.S.; Writing—Review & Editing, P.D.G., M.C. (Mattia Crespi), A.R., A.M., M.D.R., D.P., G.B., M.C. (Myrta Castellino) and P.S.; Visualization, A.R. and D.P.; Supervision, P.D.G. and M.C. (Mattia Crespi).

**Funding:** This research received no external funding.

**Acknowledgments:** Pier Paolo Pecoraro (IDRO-GEOTEC) is acknowledged for his help and expertise during the installation of the instruments. The skipper Matteo Miceli is also acknowledged for his contribution. A special acknowledgement is due to Leica Geosystem for providing the high-precision GPS receivers and to Giovanni Besio for providing the DICCA wave data.

**Conflicts of Interest:** The authors declare no conflict of interest.

## References

- Iseki, T.; Ohtsu, K. Bayesian estimation of directional wave spectra based on ship motions. *Control. Eng. Pract.* **2000**, *8*, 215–219. [[CrossRef](#)]
- Belleter, D.J.; Galeazzi, R.; Fossen, T.I. Experimental verification of a global exponential stable nonlinear wave encounter frequency estimator. *Ocean. Eng.* **2015**, *97*, 48–56. [[CrossRef](#)]
- Tannuri, E.A.; Sparano, J.V.; Simos, A.N.; Da Cruz, J.J. Estimating directional wave spectrum based on stationary ship motion measurements. *Appl. Ocean. Res.* **2003**, *25*, 243–261. [[CrossRef](#)]
- De Girolamo, P.; Di Risio, M.; Beltrami, G.; Bellotti, G.; Pasquali, D. The use of wave forecasts for maritime activities safety assessment. *Appl. Ocean. Res.* **2017**, *62*, 18–26. [[CrossRef](#)]
- Hirayama, T. Real-time estimation of sea spectra based on motions of a running ship, 2nd report: Directional wave estimation. *J. Kansai Soc. Nav. Archit.* **1987**, *204*.
- Iseki, T.; Ohtsu, K.; Fujino, M. A Study on Estimation of Directional Spectra Based on Ship Motions. *Jpn. Inst. Navig. J.* **1992**, *86*, 179–188. [[CrossRef](#)]
- Webster, W.C.; Dillingham, J.T. Determination of directional seas from ship motions. In Proceedings of the Conference on Directional Wave Spectra Applications, Berkeley, CA, USA, 14–16 September 1981.
- Roggenbuck, O.; Reinking, J. Sea Surface Heights Retrieval from Ship-Based Measurements Assisted by GNSS Signal Reflections. *Mar. Geod.* **2019**, *42*, 1–24. [[CrossRef](#)]
- Roggenbuck, O.; Reinking, J.; Lambertus, T. Determination of Significant Wave Heights Using Damping Coefficients of Attenuated GNSS SNR Data from Static and Kinematic Observations. *Remote Sens.* **2019**, *11*, 409. [[CrossRef](#)]
- Nielsen, U.D. Deriving the absolute wave spectrum from an encountered distribution of wave energy spectral densities. *Ocean Eng.* **2018**, *165*, 194–208. [[CrossRef](#)]
- Nielsen, U.D.; Brodtkorb, A.H.; Sørensen, A.J. Sea state estimation using multiple ships simultaneously as sailing wave buoys. *Appl. Ocean Res.* **2019**, *83*, 65–76. [[CrossRef](#)]
- Nielsen, U.D. Estimations of on-site directional wave spectra from measured ship responses. *Mar. Struct.* **2006**, *19*, 33–69. [[CrossRef](#)]
- Kahma, K.; Hauser, D.; Krogstad, H.; Lehner, S.; Monbaliu, J.; Wyatt, L. *Measuring and Analysing the Directional Spectra of Ocean Waves*; COST 714; EUR 21367; COST Office: Brussels, Belgium, 2005.
- Herbers, T.; Jessen, P.; Janssen, T.; Colbert, D.; MacMahan, J. Observing ocean surface waves with GPS-tracked buoys. *J. Atmos. Ocean. Technol.* **2012**, *29*, 944–959. [[CrossRef](#)]
- Longuet-Higgins, M.; Cartwright, D.; Smith, N. Observations of the Directional Spectrum of Sea Waves Using the Motions of a Floating Buoy. *Deep Sea Res. Oceanogr. Abstr.* **1965**, *12*, 53.
- Long, R.B. The statistical evaluation of directional spectrum estimates derived from pitch/roll buoy data. *J. Phys. Oceanogr.* **1980**, *10*, 944–952. [[CrossRef](#)]
- Mitsuyasu, H.; Tasai, F.; Suhara, T.; Mizuno, S.; Ohkusu, M.; Honda, T.; Rikiishi, K. Observations of the directional spectrum of ocean Waves Using a cloverleaf buoy. *J. Phys. Oceanogr.* **1975**, *5*, 750–760. [[CrossRef](#)]
- Branzanti, M.; Colosimo, G.; Mazzoni, A. Variometric approach for real-time GNSS navigation: First demonstration of Kin-VADASE capabilities. *Adv. Space Res.* **2017**, *59*, 2750–2763. [[CrossRef](#)]
- De Girolamo, P.; Crespi, M.; Romano, A.; Mazzoni, A.; Di Risio, M.; Pasquali, D.; Bellotti, G.; Castellino, M.; Sammarco, P. Wave characteristics estimation by GPS receivers installed on a sailboat travelling off-shore. In Proceedings of the 2018 IEEE International Workshop on Metrology for the Sea; Learning to Measure Sea Health Parameters (MetroSea), Bari, Italy, 8–10 October 2018; pp. 18–22. [[CrossRef](#)]
- Colosimo, G.; Crespi, M.; Mazzoni, A. Real-time GPS seismology with a stand-alone receiver: A preliminary feasibility demonstration. *J. Geophys. Res. Solid Earth* **2011**, *116*. [[CrossRef](#)]
- Colosimo, G.; Crespi, M.; Mazzoni, A.; Dautermann, T. Co-seismic displacement estimation: Improving tsunami early warning systems. *Gim Int.* **2011**, *25*, 19–23.

22. Holthuijsen, L.H. *Waves in Oceanic and Coastal Waters*; Cambridge University Press: Cambridge, UK, 2010.
23. Barber, N. The directional resolving power of an array of wave detectors. In *Proceedings of the Conference Ocean Wave Spectra*; Prentice-Hall, Inc.: Upper Saddle River, NJ, USA; pp. 137–150.
24. De Girolamo, P.; Romano, A.; Bellotti, G.; Pezzoli, A.; Boscolo, A.; Crespi, M.; Mazzoni, A.; Di Risio, M.; Pasquali, D.; Franco, L.; et al. Analysis of the 21/22 October 2014 storm experienced by the sailboat ECO40 in the Gulf of Lion. In *Proceedings of the 3rd International Congress on Sport Sciences Research and Technology Support, icSPORTS, Lisbon, Portugal, 15–17 November 2015*; pp. 290–298.
25. De Girolamo, P.; Romano, A.; Bellotti, G.; Pezzoli, A.; Castellino, M.; Crespi, M.; Mazzoni, A.; Di Risio, M.; Pasquali, D.; Franco, L.; et al. Met-ocean and heeling analysis during the violent 21/22 October 2014 storm faced by the sailboat ECO40 in the Gulf of Lion: Comparison between measured and numerical wind data. *Commun. Comput. Inf. Sci.* **2016**, *632*, 86–105. [[CrossRef](#)]
26. De Boni, M.; Cavaleri, L.; Rusconi, A. The Italian waves measurement network. In *Proceedings of the 23rd International Conference on Coastal Engineering, Venice, Italy, 4–9 October 1992*; pp. 1840–1850.
27. Mentaschi, L.; Besio, G.; Cassola, F.; Mazzino, A. Performance evaluation of Wavewatch III in the Mediterranean Sea. *Ocean Model.* **2015**, *90*, 82–94. [[CrossRef](#)]



© 2019 by the authors. Licensee MDPI, Basel, Switzerland. This article is an open access article distributed under the terms and conditions of the Creative Commons Attribution (CC BY) license (<http://creativecommons.org/licenses/by/4.0/>).



Article

# The AMERIGO Lander and the Automatic Benthic Chamber (CBA): Two New Instruments to Measure Benthic Fluxes of Dissolved Chemical Species <sup>†</sup>

Federico Spagnoli <sup>1,\*</sup>, Pierluigi Penna <sup>1</sup>, Giordano Giuliani <sup>1</sup>, Luca Masini <sup>2</sup>  
and Valter Martinotti <sup>3</sup>

<sup>1</sup> Istituto per le Risorse Biologiche e le Biotecnologie Marine (IRBIM), Consiglio Nazionale delle Ricerche (CNR), Ancona 60125, Italy; pierluigi.penna@cnr.it (P.P.); giordano.giuliani@cnr.it (G.G.)

<sup>2</sup> Institute for Microelectronics and Microsystems, Consiglio Nazionale delle Ricerche, Bologna 40129, Italy; masini@bo.imm.cnr.it

<sup>3</sup> Dipartimento Sviluppo sostenibile e Fonti Energetiche, RSE SpA, Milano 20134, Italy; valter.martinotti@rse-web.it

\* Correspondence: federico.spagnoli@cnr.it; Tel.: +39-071-2078847

<sup>†</sup> This paper is an extended version of paper published in Spagnoli, F.; Giuliani, G.; Martinotti, V.; Masini, L.; Penna, P. AMERIGO and CBA: A new lander and a new automatic benthic chamber for dissolved benthic flux measurements. In Proceedings of the 2018 IEEE International Workshop on Metrology for the Sea; Learning to Measure Sea Health Parameters (MetroSea), Bari, Italy, 8–10 October 2018.

Received: 28 April 2019; Accepted: 5 June 2019; Published: 10 June 2019

**Abstract:** Marine environments are currently subject to strong ecological pressure due to local and global anthropic stressors, such as pollutants and atmospheric inputs, which also cause ocean acidification and warming. These stressors can result in biogeochemical cycle variations, environmental pollution, and changes in benthic-pelagic coupling processes. Two new devices, the Amerigo Lander and the Automatic Benthic Chamber (CBA), have been developed to measure the fluxes of dissolved chemical species between sediment and the water column, to assess the biogeochemical cycle and benthic-pelagic coupling alterations due to human activities. The Amerigo Lander can operate in shallow as well as deep water (up to 6000 m), whereas the CBA has been developed for the continental shelf (up to 200 m). The lander can also be used to deploy a range of instruments on the seafloor, to study the benthic ecosystems. The two devices have successfully been tested in a variety of research tasks and environmental impact assessments in shallow and deep waters. Their measured flux data show good agreement and are also consistent with previous data.

**Keywords:** lander; benthic chambers; benthic fluxes of dissolved chemical species; marine technology; marine instrumentation

---

## 1. Introduction

Marine environments are affected by strong ecosystem stressors that include direct human activities (e.g., marine traffic, offshore activities, mining, coastal works) and inputs (e.g., dumping of solid waste on the seafloor, anthropic inputs transported by rivers, ballast water discharge) and chemical and climate changes that act on a global scale (e.g., raised CO<sub>2</sub> levels and air temperature). These stressors affect marine chemistry and processes by inducing ocean acidification, global sea warming, and changes in hydrological and biogeochemical cycles [1]. Human activities also result in an increased supply of trophic substances, which, in some environmental settings such as shallow enclosed seas with low hydrodynamics, can lead to dystrophic crises [2–4]. These stressors also have the potential to alter the biogeochemical cycles of elements such as carbon, phosphorus, nitrogen, silicon, and metals, which can severely damage economic activities, such as fishing and tourism [4,5]. Moreover, the introduction

and accumulation of heavy metals and organic substances (Polycyclic Aromatic Hydrocarbons (PAHs), pesticides, drugs) can induce strong pollution problems involving both the water column and sediment. These pollutants can modify or be incorporated in the food chains, damaging the ecosystem and heightening the risk for human health [5]. In particular, in the past few decades the marine biogeochemical cycle of carbon has undergone an acceleration as a consequence of increased atmospheric CO<sub>2</sub>, which has resulted in reduced seawater pH and carbon sinking rates [6].

The alterations in the marine biogeochemical cycles of elements and pollution due to human activities can affect the water column, the bottom sediment, and the transfer processes at the sediment-water interface. The research into and the development of devices to enhance the study of marine biogeochemical and benthic-pelagic coupling processes is therefore very useful [7–9], also in Italy [10–13].

A variety of devices have been developed to study benthic-pelagic coupling processes. In the past few decades, benthic landers with different setups have been developed for a wide range of purposes and their technological features and models have extensively been reviewed [14–22]. Benthic landers are equipped with diverse sensors and devices according to the tasks they are deployed to perform, including microprofilers, planar optodes, and digital cameras to study sediment-water interface properties; eddy correlation systems to measure the fluxes of dissolved chemical species in extensive areas; video cameras to investigate the deep sea biota; and oceanographic sensors (O<sub>2</sub>, pH, redox potential (Eh or ORP), optical turbidity, CTD, current meters, sediment traps) to study the water column [8,9,23–28]. In the past few years, other and much more complex and expensive devices have also been developed, such as landers for hadal environments [29–33], for multipurpose uses, and for transporting other mobile devices [34–37].

An important benthic-pelagic coupling process is the flux of dissolved chemical species at the sediment-water interface, generated by early diagenesis processes [38–40] or by volcanic benthic exhalation [41,42]. Such fluxes can strongly affect the chemistry of the water column, hence its ecology. This is especially true of shelf and coastal environments, where the high intensity of early diagenesis processes, due to a high reactive organic matter content in surface sediments, produces strong fluxes that affect shallow water columns [43].

The benthic fluxes of dissolved substances can be studied by onboard incubation or by in situ experiments, which are usually more reliable [44]. Fluxes are measured in benthic chambers handled by divers [45] in shallow waters, or mounted on benthic landers in deeper waters [44].

Landers equipped with one or more benthic chambers have been developed in the past [46–55].

Two new, low-cost, light, and easy to handle devices, the Amerigo Lander and the Automatic Benthic Chamber (CBA), which have recently been devised to study benthic ecosystems, particularly the fluxes of dissolved substance between sediment and the water column, are illustrated in this paper [56]. The two devices can also be employed jointly to improve the reliability of particular investigations.

The Amerigo Lander is basically a vector that can be deployed in shallow and deep bottoms and which returns to the surface at the end of its mission. It can carry a variety of instruments to study the water column and the benthic ecosystems by measuring various environmental parameters and processes.

The Amerigo Lander and the CBA have provided the Italian scientific community with new and highly innovative instruments to investigate the benthic ecosystems and their interactions with the water column, bridging a scientific and technological gap with North American [25,35,37,46–55], Northern European [23,24,26,36,49] and Asian [27–30,33,34,50] countries.

Their technical features make the two devices versatile and easy to use. The modularity of the lander, the various instruments that it can carry, and the much larger number of parameters that it can measure, compared with existing devices, make it a complete and original apparatus, suitable for operating both in shallows and at great depths. The most innovative features of the CBA are the larger area where measurements are acquired, which makes the fluxes more representative [23,24], and its easy and fast rigging, light weight, and maneuverability, which make it easy to use.

Both devices operate autonomously. Amerigo can work from shallow bottoms to depths of 6000 m, whereas the CBA has been designed for shallow water to shelf environments (up to about 200 m). Furthermore, the CBA can fit in the Amerigo, if required by research needs.

## 2. Amerigo Lander and Automatic Benthic Chamber: Technical Specifications and Equipment

### 2.1. The Amerigo Lander

The Amerigo Lander is essentially a carrier with a tripod structure that can host different types of instrumentation to measure biogeochemical and geophysical parameters and can collect water and sediment samples (Figure 1). It has been conceived as a simple, low-cost, and practical device that can be employed frequently in a variety of research tasks and environments, since it does not require huge resources, large vessels, or long missions.

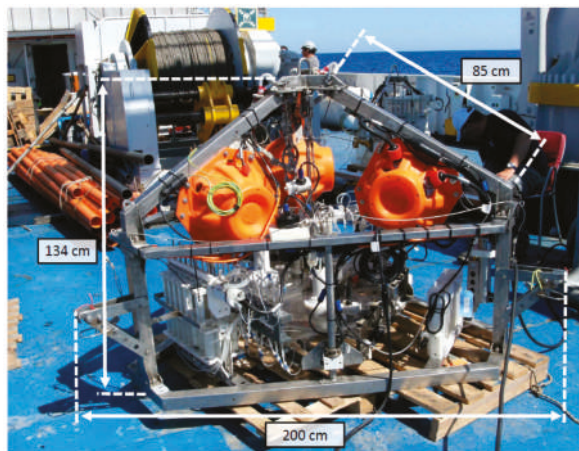


**Figure 1.** Photograph of the Amerigo Lander showing the tripod structure, the measurements, and the main instrumentation and devices.

Since it reaches the bottom through a speed-controlled free-fall and returns to the surface by positive buoyancy, after a timed release of the ballast weights, it requires no drive or propulsion systems, such as thrusters or cables, nor divers for positioning and recovery. It is also completely automatic, because all hosted instruments and mechanical devices are powered in situ and activated and managed by electronics and software, again without the need for divers or cables. Obviating the need for divers also allows for overcoming stringent safety issues, particularly Italian safety regulations, with considerable savings. The elimination of a cable connection to the vessel makes the lander easy to handle, because the support ship can move while the lander is working on the seafloor.

Another important advantage is its modular structure. In fact, the basic tripod structure can support a variety of components and instrumentation, which can be assembled and set to meet diverse research needs and environmental situations, ensuring flexible and simple operability. In particular, the lander's electronics and power supply have been developed to enable management of additional devices and operations and for increased deployment time. Its modular structure allows the Amerigo Lander to operate in shallow waters (lagoons, estuaries, continental shelves) and deep-bottoms (abyssal plains). Further savings have been obtained from the electronic housings and the release mechanisms.

The lander's basic structure consists of a stainless-steel tripod measuring 200 cm in width and 134 cm in height (Figure 1). All the electronic and mechanical devices required for reaching the seabed and returning to the surface and for hosting and managing the instruments operating on the seafloor are installed in the tripod (Figure 1).

The bottom is reached by a free fall without the need for thrusters or power, because the descent configuration envisages three ballast weights at the three ends and four buoys (Figure 2), which result in negative buoyancy.

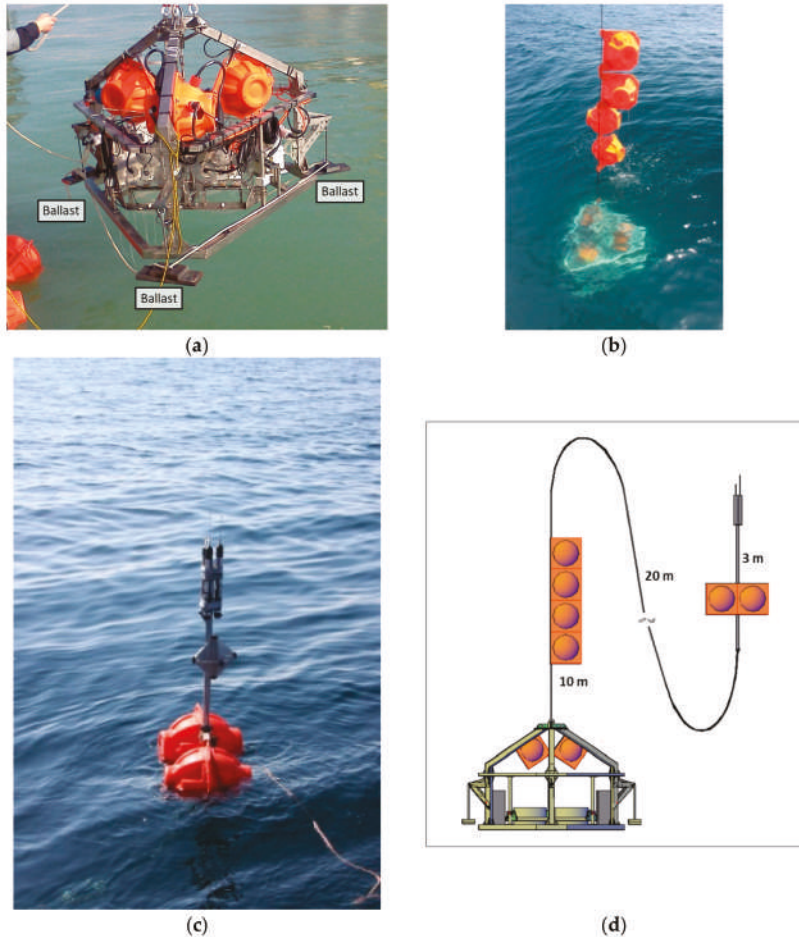


**Figure 2.** Amerigo Lander descent configuration. (a) The ballast weights mounted on the tripod; (b) the four buoys tethered to the tripod structure; (c) the recovery pole with the two buoys and the three localization devices; and (d) a schematic drawing of the Amerigo Lander during deployment on the seafloor.

The buoys are commercially available glass spheres (outer diameter 432 mm, thickness 14 mm, buoyancy 260 N), built for depths up to 6700 m (Nautilus Marine Service GMBH, VITROVEX Deep Sea Floatation Sphere), protected by a plastic shell (Nautilus Marine Service GMBH, SR330). The equilibrium between the buoys and the weights depends on the lander's weight in the water, its descent and landing speed, and ascent requirements.

In the present configuration, the lander weighs 294 kg in air and 131 kg in water and the 4 buoys have a buoyancy in seawater of 1040 kg, whereas the ballast weighs 45 kg (15 kg per weight). The buoys are tethered to the tripod with a rope 10 cm in thickness and 5 m in length (Nautilus Marine Service GMBH, EDDYROPE). Another rope, 10 cm in thickness, is tied to the recovery pole. The pole is fitted

with 2 buoys the same size as the 4 buoyancy array buoys and with a 10 kg ballast weight, to support the recovery devices about 2 m above the sea surface (Figure 2d).

With this configuration the lander's initial descent speed is 0.78 m/s. The thrust of the 2 buoys tied to the recovery pole reduces the descent and landing speed to 0.52 m/s (Figure 3). With this set up, the lander can reach the bottom fast enough to avoid being shifted too much by lateral currents, and slowly enough to avoid an excessively strong impact.

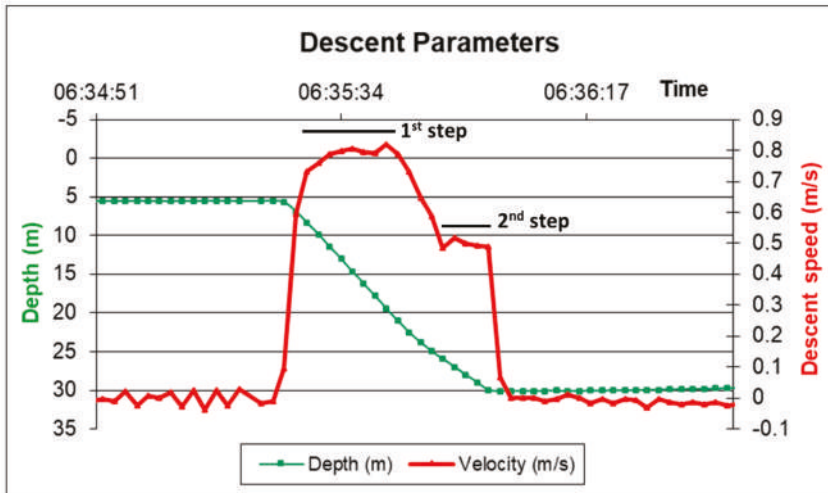


**Figure 3.** Amerigo Lander descent data. The data refer to the setup with three benthic chambers. Red line: Descent and landing speed. First step: Speed before activation of the first 2-buoy array; Second step: Speed after activation of the two buoys of the recovery pole. Green line: Depth profile.

The buoys are tethered to the tripod by a rope, not mounted directly on the tripod as in several other landers [26,47,50,51,54,55]. This solution has been adopted for two reasons, as follows: (i) As separation of the main tripod structure from the buoys makes the lander lighter and smaller, enhancing maneuverability in deployment and recovery operations, this solution requires smaller frames and less powerful winches; and (ii) this setup allows the lander to be transported in an ordinary van that can be driven with an ordinary license. Furthermore, the buoys and the recovery pole may not be needed in case of operation in shallow water, further enhancing maneuverability and reducing vessel size requirements. These features increase cost-effectiveness and the ease of organization.

After completion of the measurement and sampling operations, the lander returns to the surface autonomously. The release of the three ballast weights and the thrust of the buoy array results in positive buoyancy. In the present configuration (4 thrust buoys, 2 recovery pole buoys, 3 benthic chambers) its ascent speed is about 0.2 m/s (Figure 4).

At the end of the bottom operations, the ballast weights are released by a burn wire mechanism that unlocks the three lever hooks (Figure 5). This system is much less expensive than acoustic release [57] and further contributes to make the lander cost-effective and easy to use and to program.

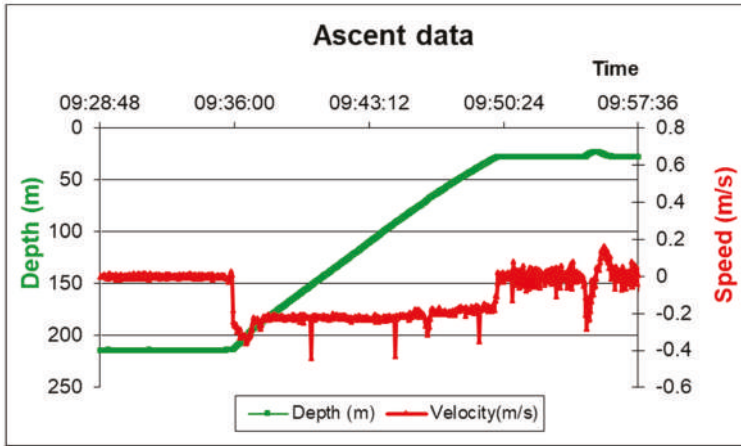


**Figure 4.** Amerigo Lander ascent data. The data refer to the setup with three benthic chambers. Red line: Ascent speed. Green line: Depth profile.

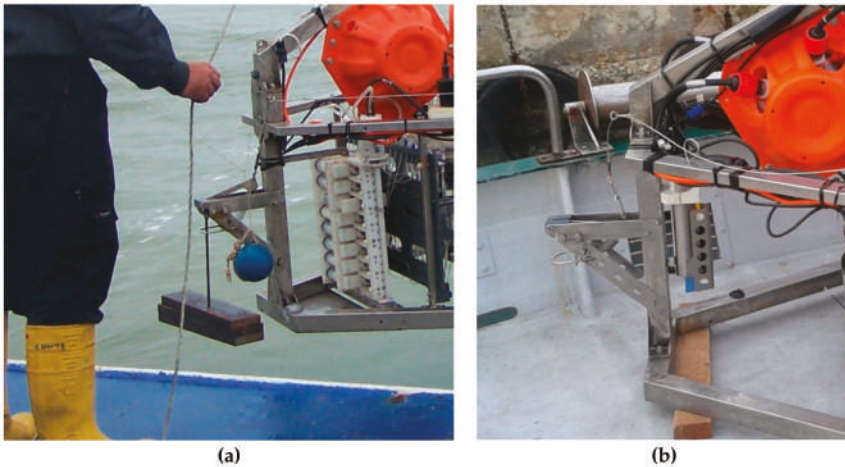


**Figure 5.** The three lever hooks in a locked (a) and unlocked (b) position.

In case of deployment in deep water, the Amerigo Lander may surface at a considerable distance from the dropping site, due to lateral sea currents during the ascent. To facilitate recovery, the lander is equipped with three redundant localization devices fitted on the top of the recovery pole, a GPS (Novatech ARGOS Beacons, Dartmouth, NS, Canada), a directional radio (Novatech Radio Beacon, Dartmouth, NS, Canada), and a flash (Novatech Xenon Flasher, Dartmouth, NS, Canada) for night recovery (Figure 6).

The Amerigo Lander is also equipped with instruments for monitoring and measuring the physical-chemical parameters throughout deployment, from descent to ascent. They include a CTD (SBE 37-SI MicroCAT, Sea-Bird Scientific, Bellevue, WA, USA) for continuous water column pressure, conductivity, and temperature recording, and a camera supporting an SD card from 4GB to 32GB (Telesub Lanterna, La Spezia, Italy) (Figure A1, Appendix A) for monitoring the lander's operation. In fact, both instruments monitor the lander's activities, particularly the beginning of descent, the descent speed, the landing, the functioning of the mechanical devices, the beginning and speed of the ascent, and the lander's surfacing.

Additionally, in this case, both the CTD and the video camera are commercially available to save construction costs. In particular, the video camera is a commercially available camera hosted in a pressure-resistant case.



**Figure 6.** Amerigo Lander recovery system. (A) GPS localization (Novatech ARGOS Beacons); (B) directional radio localization system (Novatech Radio Beacon); and (C) flash for visual localization at night (Novatech Xenon Flasher).

## 2.2. Electronics and Power Supply

The Amerigo Lander's electronics and power supply are developed in-house (Figure 7, Figure A2 of Appendix A). The system is available on request. The burn wire system and all the mechanical and electronic devices, sensors, and probes are powered, turned on, turned off, and managed by the electronics and the batteries fitted in the tripod. The data collected in situ are also stored in the Amerigo electronics. The main hardware components are configured as illustrated in Tables A1 and A2, and Figure A2 of Appendix A. The philosophy of electronics is to be as open as possible, i.e., to enable

fitting other sensors or devices by the availability of redundant on/off, serial, and analogic ports and the possibility of managing these sensors/devices and other operations by the software.

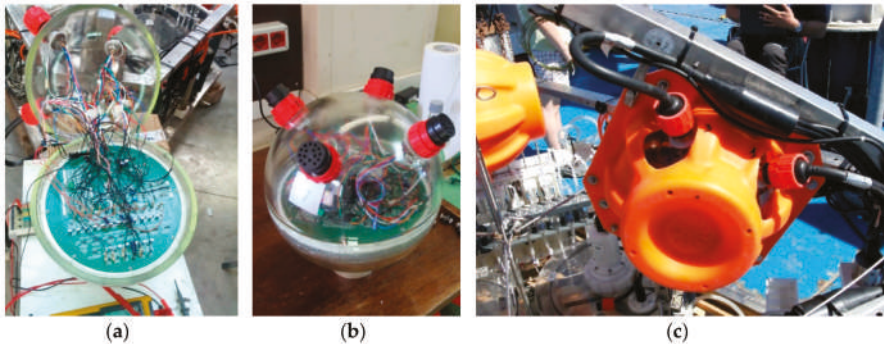


**Figure 7.** Amerigo Lander electronics: (a) Firmware testing phase and soldered cables inside the glass sphere; (b) electronics fitted in the glass sphere; (c) a glass sphere mounted on the tripod with the plastic case, marine connectors, and cables.

The Amerigo Lander is powered by two pairs of 12 V, 18 Ah, rechargeable lead batteries that are connected in parallel and fitted in a pressure-resistant case. The fact that they are commercially available and Pb-based involves lower managing and setup costs, compared to other metal-based batteries. The first pair is supported by the redundant second pair, which is only activated in case of exhaustion or failure of the first pair. This power supply supports about a 40 h operation of the lander in its present configuration. The Pb batteries can be increased or their type changed to support different configurations or to extend the operating time.

In the event of a failure of the general power supply or of the main electronics, a safety burn wire device powered by an independent 9 V battery and controlled by a dedicated electronic circuit is activated, after a predetermined time, to release the ballast for the final ascent. An additional safety system consists of a magnesium ring that is corroded by seawater. In case of the failure of all the electronic devices, its disappearance releases the ballast weights [58].

The electronics and the batteries are hosted in glass spheres built for depths of up to 7000 m (Nautilus Marine Service GMBH, VITROVEX Deep Sea Instrument Sphere; size: 13", outer/inner diameter: 330/306 mm, glass type: DURAN 8330), which are connected to the electronic devices, sensors, probes, and thrusters by marine connectors (Figure 7). The glass spheres are also commercially available and cost less than metal cylinders.

The two battery pairs are recharged on board by a cable that is removed before deployment. The cable is also used for serial port communication with the PC.

The main serial port (RS232-1) is devoted to communication with the PC. It allows for entering commands, changing the setup, downloading recorded data from the RAM flash memory or, in case of direct monitoring, it enables visualizing the data, the situation on the bottom, and the ongoing operations, as well as reporting malfunction alarms in real time (Figure A2 of Appendix A). The same port can be used to connect an acoustic modem for underwater communication.

The second serial port (RS232-2) is multiplexed in order to communicate with infinite RS-232 serial sensors, limited only by the hardware power connections (Figure A2 of Appendix A).

Different systems have been designed to protect the lander's electronics. The power supply to each electrical device (sensors, motors, batteries, burn wires) is protected by an electrical shunt that limits current drain. In case of failure of a device, the power supply to it is cut off to prevent a general electronic failure.

Furthermore, the open electronics and the excess of on/off, serial (by means of a multiplexed serial port), and analogic communication ports allows fitting many other electronic sensors, devices, and instruments, with respect to other system that are devised for standardization as well as useful use [28].

The following sensors are currently installed in the Amerigo Lander (Table 1) (Figure A2 of Appendix A):

**Table 1.** Technical specifications of the sensors installed in the Amerigo Lander.

Sensor Type	Company	Parameter	Resolution	Initial Accuracy	Maximum Depth (m)
SBE37-SI (CTD)	Sea Bird Electronics	Conductivity (S/m)	0.00001	0.0003	7000
		Temperature (°C)	0.002	0.0001	7000
		Depth (m)	0.002% FS	0.1% FS	7000
SBE5T (Pump)	Sea Bird Electronics				7000
Oxygen Optode 3830	AANDERAA	Oxygen concentration (µM)	<1 µM	<8 µM	6000
		Air saturation (%)	0.4%	<5%	6000
Seapoint Turbidity Meter	Seapoint	Turbidity (FTU)	10 mV/FTU (range 500 FTU)	<1%	6000
		Mets	Franatech	2.44 µM (range 50 nM–10 µM)	<1%
pH	AMT	pH	0.01	0.05	6000

An important question is the operation limit connected with temperature. The temperature operation limit of Amerigo coincides with the lower operation value between the sensors fitted in the benthic chambers and the polycarbonate (i.e., 40 °C (optode sensor); if the lander is used without sensors the temperature limit is <140 °C (polycarbonate)).

### 2.3. Burn Wire Device

The burn wire mechanism [51] consists of a metal wire coated with a plastic film that is corroded and then broken by an electric current at a bare point where the coating is interrupted (Figure A2, Appendix A). A simple 12 kg fishing wire coated with a thermo-shrinkable tube is a typical design. The plastic-coated wire usually keeps a lever hook locked. When the electric current runs through the wire, the bare point interacts with seawater, which triggers a reaction (1) that consumes the wire completely, leading to release of the lever hook, as follows:



where  $M^0$  is the metal of the wire,  $2e^-$  is the electric current, and  $M^{2+}$  is the metal in the solution. The electric circuit is closed by an electric mass on the metal tripod. By this method, any spring- or gravity-based mechanical device can be actioned by the release of a mechanical device or lever hook that can hold several tens of kilos, depending on the length of the lever (Figure 5). A metal wire, 0.4 mm in thickness with a resistance of a 12 Ω/m, exposed to an electric current of 200 mA in normal seawater (36 PSU) is usually consumed and broken in about 20 s. As mentioned above, the burn wire system is much less expensive than any acoustic release system.

### 2.4. Current Configuration of the Amerigo Lander

In its current configuration, the Amerigo Lander is equipped with instruments and sensors for measuring benthic fluxes of dissolved chemical species and for monitoring physical-chemical parameters in the near-bottom sea water column. In particular, the former measurements at the sediment-water interface are performed using three benthic chambers, two water sampling systems, and some sensors fitted in the chambers (Figures 8–12).

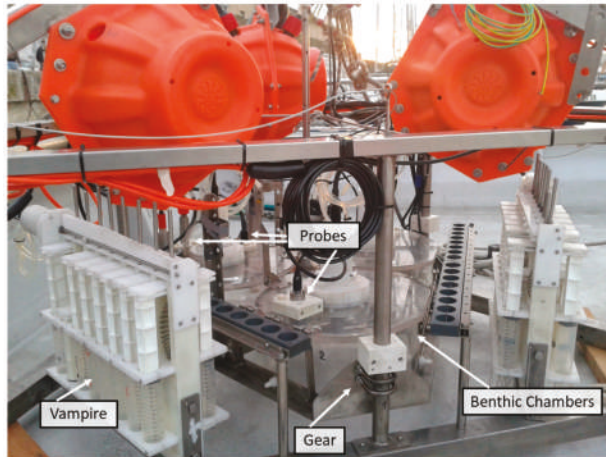


**Figure 8.** Amerigo Lander: The three benthic chambers, the two water sampling devices, the three probes in a chamber, and the chassis on which the chambers are mounted.

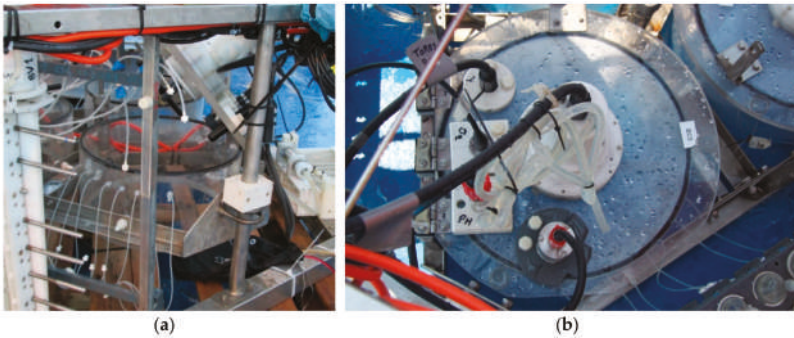


**Figure 9.** Amerigo Lander. (a) Lateral view of a benthic chamber mounted on the chassis with the top lid open, the tubes on the lateral wall to collect water samples, and the rotating paddle. (b) Top view of a benthic chamber with the closed top lid fitted with the oxygen, pH, methane, and turbidity sensor.

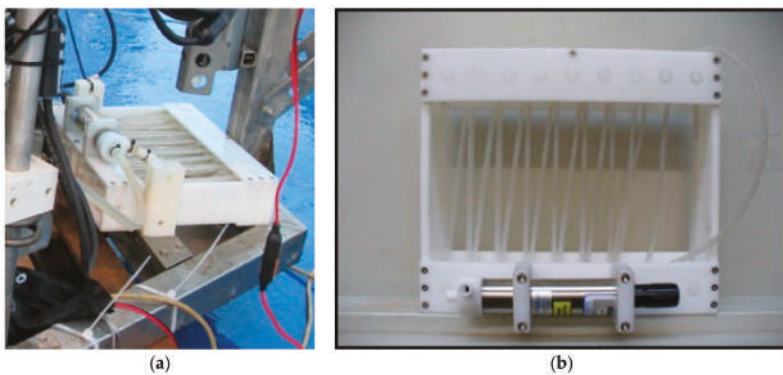


**Figure 10.** The OxyStat oxygen replacement device. (a) The pump and the tube connected to the interior of the chamber; (b) view from above.

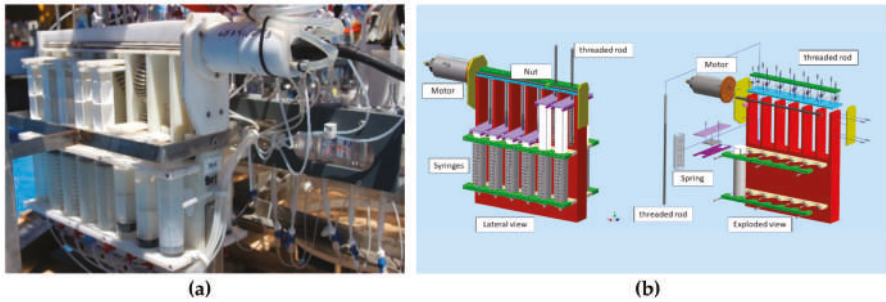


**Figure 11.** The VAMPIRE device allows drawing water into the chamber or expelling it as well as injecting a tracer inside the chamber. (a) Photograph of the VAMPIRE device installed on the Amerigo Lander; (b) schematic drawing of the VAMPIRE device.



**Figure 12.** The Delrin case hosting the electric motors with the silicone tube pressure-compensation system.

The benthic chambers are polycarbonate cylinders with a movable polycarbonate top lid (Figures 8 and 9a). The cylinders measure 37 cm (inner diameter) by 20 cm (height) and have a countersink in the bottom to facilitate penetration in sediment [46].

The three benthic chambers are mounted on a chassis (Figures 8 and 9a) that is released by a burn wire mechanism a few minutes after the tripod has landed on the seabed. The chambers are mounted 5 cm over the plate of the structure so that they can penetrate into the sediment for 5 cm, while the remaining 15 cm remain above the sediment. A few minutes after deployment of the chambers on the seabed, the lid of each chamber is unhooked, again by a burn wire device, thus closing the chamber

and holding a known volume of water (approximately 17 L) overlying a known area of sediment [46]. The chassis and lid release time can be programmed by the lander's software to adapt them to the research task and the type of sea bottom.

The chemical and physical-chemical parameters in the chambers and some solute are measured by the following sensors fitted in each chamber during deployment: An oxygen sensor (AANDERAA, Oxygen Optode 3830, Aanderaa Data Instruments AS, Bergen, Norway), a turbidity sensor (Seapoint Turbidity Meter, Seapoint Sensors, Inc., Exeter, NH, USA), a methane sensor (ASD-Sensortech GmbH, METS methane sensor, Franatech GmbH, Lüneburg, Germany) and a pH (AMT, pH-combined sensor, AMT Analysenmesstechnik GmbH, Rostock, Germany) sensor (Table 1) mounted on the lid (Figure 9b). The power-on/power-off and measurement intervals of each sensor can be set by the lander's software according to research requirements.

The chambers also contain an OxyStat device, which allows for replacing the oxygen consumed in the chamber [59]. The device is connected to the chamber by a water pump (SEABIRD SBE5T, Sea-Bird Scientific, Bellevue, WA, USA) and a silicone tube (Figure 10) and is controlled by the lander's software and the oxygen probe inside the chamber. In practice, the software receives the chamber oxygen concentration data and when its level falls below a given threshold, the software turns the OxyStat pump on. The oxygen-poor water in the chamber is pumped into the 15 m long gas-permeable silicone tube, it adsorbs oxygen from surrounding seawater, and is pumped back into the benthic chamber. Restoration of the oxygen level to the predetermined threshold results in the pump being turned off. The minimum and maximum oxygen concentrations can be set by the lander's software before the mission or calculated on the basis of the initial concentration measured in the chamber.

Each benthic chamber is connected (Figure 9a) by silicone tubes (inner diameter, 1.5 mm, outer diameter 3 mm) to a water sampling device (VAMPIRE) to collect water or to introduce tracers into the chambers (Figure 11). The VAMPIRE consists of a Delrin frame hosting 8 pairs of syringes, each pair capable of collecting/injecting a maximum volume of 280 mL of water or tracer. If one syringe of the pair is not connected to the inside, seawater outside the chamber can be collected while the other syringe draws water inside the chamber. Each couple of syringes is activated by a nut moving on a rotating stainless-steel rod. The nut moves the levers that release the stainless-steel springs, which actuate the syringe pair in suction or injection mode. The rod is controlled by an electric motor (CBF Motors SRL, CRB35GM, CBF motors srl, Lissone, Italy) which is powered on and off by the lander's software. Its timing and the activation of water sampling or tracer injection can also be set by the lander's software.

In research tasks involving analysis of dissolved gases, a set of glass ampoules can be added before the syringes of the VAMPIRE device (Figure A3, Appendix A) to store the water samples in a gas-impermeable vessel until analysis.

Each benthic chamber is also equipped with a stirring system, consisting of a rotating paddle mounted on the chamber lid (Figure 9a). The paddle is actuated by the coupling of an electric motor (CBF Motors SRL, CRB35GM, CBF motors srl, Lissone, Italy) to a permanent Neodymium magnet (Supermagnete, magnetic disk diameter 30 mm, height 15 mm, Neodymium, N42, nickel-plated, Webcraft GmbH, Gottmadingen, Deutschland). The paddle turns at a speed of 4–6 rpm, reproducing the hydrodynamics near the seabed, which is responsible of the formation of the benthic boundary diffusion layer at the sediment-water interface and, consequently, of the intensity of the benthic fluxes of dissolved chemical species. The motors of the rotating paddles are also activated by the lander's software some minutes after closing of the lid.

Whereas the cases housing the electronics and the batteries are pressure-resistant, those housing the motors actuating the stainless-steel rod of the VAMPIRE device and the rotating paddles of the benthic chambers are pressure-compensated. These cases are Delrin cylinders with two silicone tubes (Figure 12) filled with a non-conductive liquid (commercially available Vaseline oil). If any air bubbles remain in the case, compression of the silicone tubes offsets the pressure difference between inside and outside, avoiding a collapse of the case.

At the end of each mission, i.e., after completion of the water sampling and sensor measurements in the benthic chambers, the three ballast weights are released by activation of the burn wire device, which induces positive buoyancy. The lander returns to the surface, where it is localized by means of the three positioning devices, and finally recovered on board. Missions typically last 8 to 36 h, depending on the tasks to be performed or the intensity of the benthic fluxes of dissolved substances, and are limited by the power supply, which, at present, supports the systems for about 40 h (see Section 2.2). However, as noted above, the open philosophy of the electronics allows the increasing of this time.

After the recovery operations, the water samples taken by the syringes are collected from the VAMPIRE, divided and treated in an inert atmosphere (Figure A4, Appendix A) for immediate (on board) or subsequent (laboratory) chemical analysis of the solutes to be determined in the benthic fluxes.

The data collected by the sensors are downloaded into a computer.

The results of the chemical analyses and the data collected by the chemical sensor are then used to calculate the benthic fluxes of dissolved chemical species (see Section 3).

### 2.5. Typical Mission of the Amerigo Lander

The Amerigo Lander hardware is all managed by wizard software, developed in-house. The software helps the operator in setting all the parameters that are required for the lander's function, to activate and test the motors, to monitor all the parameters in real time, to simulate a measurement mission, and to plan the activities for scheduling a mission. The software allows for the downloading and processing of the data collected during the mission and stored in situ. Finally, the software has been developed to fit further sensors and devices and to manage operations that are not currently scheduled.

A typical mission of the Amerigo Lander consists of six sequential phases that need to be correctly planned for the success of the mission, as follows (Figure 13):

- 1) After the on board programming and checks, such as control of the mooring line and testing of motors, sensors, communication, and security equipment, the lander is immersed into the sea, where it is held at a depth of 5 m, until activation of a dedicated burn wire mechanism releases a small buoy that confirms the functioning of the whole electronic system;
- 2) Following the buoy check, the lander is released for its free fall to the bottom;
- 3) After the lander has reached the seabed, a short interval is envisaged to allow the settling of the sediment resuspension, due to the impact of the tripod on the bottom, to settle;
- 4) Activation of a burn wire mechanism releases the chamber chassis, enabling its settling on the bottom and penetration into sediment for the first 5 cm; all the sensors in the chamber (oxygen, methane, turbidity) and CTD are sampled; the chambers are still open;
- 5) After another interval, to allow settling of the sediment resuspension due to the impact of the chamber on the bottom and to enable sensor readings, activation of another burn wire releases the benthic chamber lids;
- 6) Activation of the stirring paddles allows for mixing the seawater in the chambers;
- 7) The 8 pairs of syringes of the 2 VAMPIRES are activated by user-programmable times;
- 8) Finally, the ballast weights are released by the last burn wire and the lander floats back to the surface by virtue of its positive buoyancy.

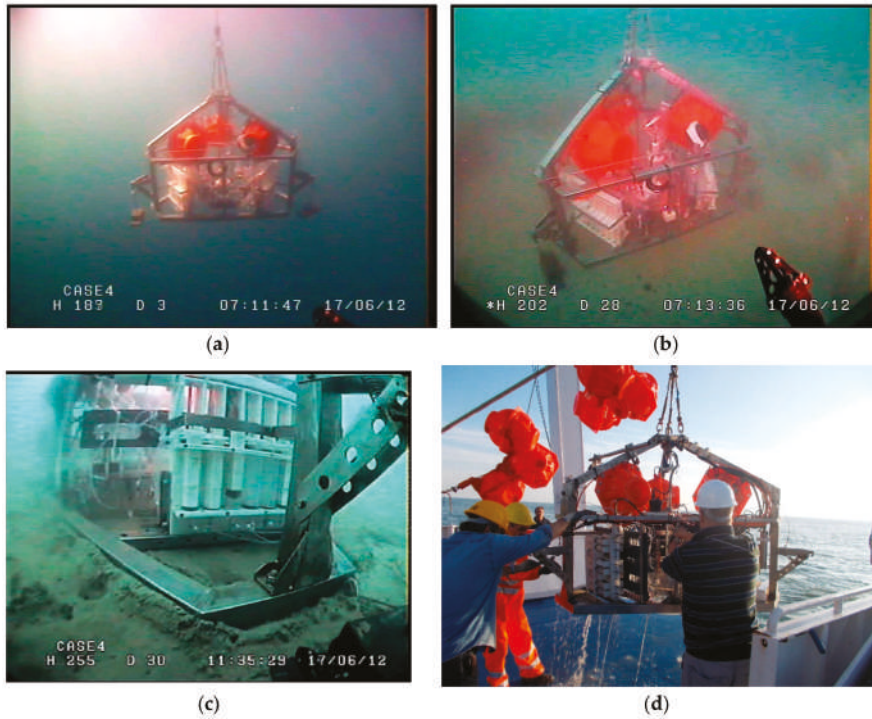


**Figure 13.** The Amerigo Lander photographed in some operational phases: (a) In the water before release; (b) on the seabed (view from above); (c) on the seabed (lateral view); and (d) on board after recovery.

## 2.6. Other Possible Configurations of the Amerigo Lander

The basic structure of the lander is the tripod, which is designed to land on the seabed by gravity, counteracted by the positive thrust of the buoys. It then performs its scheduled operations on the seabed and finally returns to the surface by virtue of positive buoyancy, after the release of the ballast weights. All the on-board instruments and devices are built to operate at depths up to 6000 m.

This setup makes the lander a vector that can host different types of instrumentation, such as sensors and probes for monitoring chemical and physical-chemical environmental parameters (pH, Eh, conductivity, temperature, salinity (calculated), oxygen, methane, pCO<sub>2</sub>, H<sub>2</sub>S) in the water column during its descent, its permanence on the bottom, and its ascent.

The lander has also been designed to host instruments such as a microprofiler, to study sediment-water interface properties, a penetrometer, to measure the mechanical properties of surface sediments, a gravimeter, to measure seismicity on the seafloor, a corer, to collect sediment cores for early diagenesis, pollution, stratigraphy, or other studies, and passive samplers of water column and sediment solutes, to study pollution and environmental processes and to determine background values. In any case, the open architecture of the electronics allows for fitting other instruments and performing other operations.

Finally, it is a modular device, consisting of the buoy array, the recovery pole, the ballast weights, and the removable and replaceable instruments that perform different tasks in different environments, from very shallow waters, like lagoons and salt marshes, to shelf areas and abyssal planes.

### 2.7. The Automatic Benthic Chamber

The CBA (Figure 14) has been developed as an alternative to the Amerigo Lander for missions involving measurements in shallow and transitional waters or work that needs to be carried out quickly and economically. This is made possible by the fact that the CBA does not require expensive maintenance, it is practical and fast to fit out, it is light and easy to maneuver, and it is deployed and recovered simply with a rope, which means that it can also be managed by small vessels.

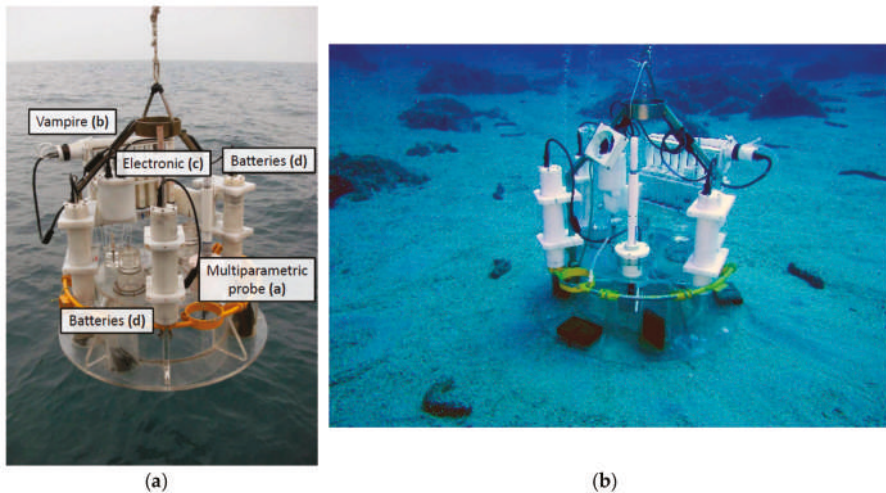


**Figure 14.** The Automatic Benthic Chamber during (a) deployment and (b) operational on the seabed with various instruments: Multiparameter probe; VAMPIRE; electronics case; and battery pack cases.

The CBA can also be mounted on the Amerigo Lander, instead of the three benthic chambers, when measurements of benthic fluxes of dissolved chemical species are to be performed over a wider area.

The present CBA is an automated device based on earlier manual benthic chambers managed by divers [60,61]. It is a Plexiglas cylinder open on the bottom and closed on top, which confines a known volume of water (approximately 100 L) overlying a known sediment area (3116 cm<sup>2</sup>) (Figure 14b). Its inner diameter is 63 cm and its height is 30 cm, of which 5 cm penetrate into the sediment and 25 cm remain above it, due to a lateral horizontal fin (Figure 14). The CBA is fitted with two valves on its top side, to let out the water entering the chamber during descent and landing (Figure 14). Like the Amerigo Lander, the CBA is equipped with an internal stirring system that reproduces the hydrodynamics near the seabed, which is responsible for the formation of the benthic boundary diffusion layer and for the intensity of the dissolved fluxes in the benthic chamber. The stirring system consists of a four-arm rotating paddle fitted on top of the inner side of the chamber. The paddle is actuated by the coupling of an electric motor (CBF Motors SRL, CRB35GM, CBF motors srl, Lissone, Italy) with a Neodymium magnet (Supermagnete, Magnetic disk 30 mm in diameter, 15 mm in height, Neodymium, N42, nickel-plated, Webcraft GmbH, Gottmadingen, Deutschland) and turns at a speed of 4–6 rpm. In the CBA, this motor is activated immediately before deployment by connecting directly the batteries to the motor.

The CBA is also equipped with a multiparameter probe (Hydrolab MS5, OTT HydroMet, Kempten, Germany) for continuous monitoring of temperature, pH, conductivity, dissolved oxygen, Eh, and salinity (calculated) in the chamber (Figure 14). Like the Amerigo Lander, it is also fitted with the VAMPIRE system for collecting water samples inside and outside the chamber and for injecting tracers inside the chamber at programmable times. The motor of the VAMPIRE is activated by simple, easily programmable, and commercially available electronics (Idec MicroSmart FC6A PLC,

IDEC Corporation, Sunnyvale, CA, USA). The cases housing the electronics, the battery packs, and the motors driving the VAMPIRE and the stirring paddle are made in Delrin and are built to withstand hydrostatic pressure up to a depth of about 200 m. Additionally, in the CBA, the VAMPIRE motor and the electronics cases are pressure-compensated by a silicone tube system filled with a non-conductive liquid (simple Vaseline oil), which affords resistance to high water pressures.

The power supply of the CBA consists of three battery packs (NI-MH size D, 12 V, 8 Ah, Torricella SRL, Milano, Italy) housed in cylindrical Delrin cases (Figure 14). Two packs are connected directly to the electronics that supply and manage the VAMPIRE motor and one pack is connected directly to the rotating paddle, while the multiparameter probe has its own power supply system.

As regards the planning of CBA operations, the syringe sampling time is set by programming the electronics, while the probe measurement time is programmed by the software of the probe itself.

With regard to deployment and recovery, the CBA is deployed on the seabed and recovered by a rope which, during measurement activities, is attached to and marked by a buoy and a light.

The CBA, both in the standalone configuration and installed in the Amerigo Lander, is a low-cost device that does not require divers or connection cables to the support ship, thus saving the steep cost of divers and the technical problems posed by the connection cable. Further savings are afforded by the fact that the electronics and the batteries are commercially available, hence the low-cost.

Like the Amerigo Lander, the CBA has a temperature operating limit which coincides with the lowest operating value of the sensors fitted in the benthic chamber and the polycarbonate, which is 50 °C (Hydrolab MS5 Multiprobe). However, if the CBA is used without the multiparameter probe the value is <140 °C (polycarbonate).

### 3. Benthic Flux Calculation

The benthic chambers of the Amerigo Lander and the CBA have been designed to measure the release/adsorption of dissolved substances at the sediment-water interface. The principle of their measurement with benthic chambers involves establishing the concentration differences of a solute over time in a known volume, confined over a known area of sediment [62].

Basically, the benthic fluxes of dissolved substances in each benthic chamber of the lander and of the CBA are calculated (2) by dividing the concentration of each solute, measured in the samples collected in the chamber by the syringes—typically nutrients such as ammonium, nitrites, nitrates, phosphates and silica, carbonate species (DIC, alkalinity, pCO<sub>2</sub>), trace elements (heavy metals), and organic pollutants—or recorded by the sensors (oxygen, methane, and pH), at the time of the collection or measurement, multiplied by the volume of the benthic chamber and divided by its base area [44].

$$D_i = \frac{\partial C_i}{\partial t} V / A, \quad (2)$$

where  $D_i$  is the flux of solute  $i$ ,  $C_i$  is the concentration of chemical  $i$ ,  $t$  is the time of sample collection or sensor measurement,  $V$  and  $A$  are the real volume and the area of each benthic chamber.

In practice, the benthic fluxes of each solute are computed as Equation (3) by multiplying the slope of the line, calculated by a least square fit with time (days) on the x-axis and the concentration at different times, multiplied by the height of the benthic chamber, on the y-axis (Figure 15).

$$D_i = y_i, \quad (3)$$

where  $y_i$  is the slope of the time vs. the concentration line of Figure 15.

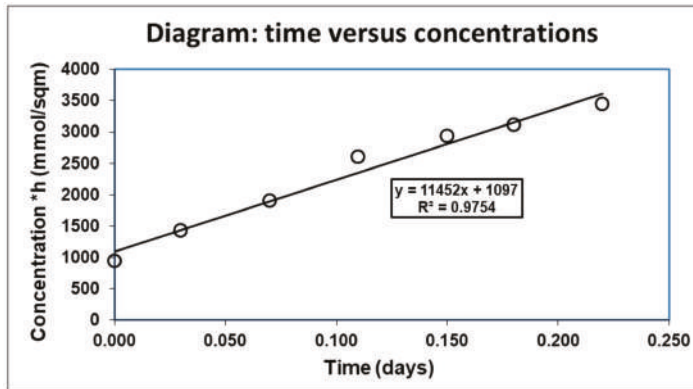


**Figure 15.** Diagram illustrating the time of water sample collection in the benthic chamber against its concentration and the correlation line.

During deployment, the real volume of each chamber is determined by injecting a solution of a non-reactive solute (tracer), e.g., CsCl, BrCl or deionized water, at a known concentration into the chambers [44] and subsequently measuring its concentration in the water samples collected in the syringes as Equation (4).

$$V_2 = \frac{V_1 * C_1}{C_2}, \quad (4)$$

where  $V_2$  is the real volume of the benthic chamber,  $C_1$  is the tracer concentration in the syringe,  $V_1$  is the volume of the tracer injected into the chamber, and  $C_2$  is the tracer concentration in the chamber after the injection.

Theoretically, the tracer concentration in the chamber after the initial injection should be constant. If this does not happen, there are three possible explanations, as follows: The benthic chamber is not well placed on the bottom, there are leaks, or an irrigation process is under way in the bottom sediment.

#### 4. Discussion

The Amerigo Lander [63–71] and the CBA [41,42,70–77] have successfully been tested and used in measurement and research activities carried out in the framework of international and national projects and in environmental investigations into the impacts of human activities on marine (e.g., harbor sediment dredging) or land environments (e.g., quality of drinking water).

The Amerigo Lander has been tested and employed in shallow, medium, and deep-sea environments, whereas the CBA has been used up to a depth of 140 m.

As a discussion of the data collected by the two devices, we report (Figure 16) the trend of the dissolved oxygen concentrations, measured in the benthic chambers of the lander (by the AANDERAA optode oxygen sensors, Aanderaa Data Instruments AS, Bergen, Norway) and the CBA (by the Hydrolab MS5 oxygen sensor, OTT HydroMet, Kempton, Germany), at the same deployment time and site [71], and on a pelitic and organic matter-rich bottom in front of the Po River Estuary [78,79]. All the benthic chambers of the two devices recorded similar continuously decreasing values, due to mineralization of the high content in fresh reactive organic matter, deposited in front of the Po River Estuary.

The benthic fluxes of solutes, whose concentrations were determined in the water samples collected by the VAMPIRE syringes, also showed reliable data. In fact, very similar values were determined for the fluxes of dissolved inorganic carbon (DIC) (Figure 17) measured by the three benthic chambers of the Amerigo Lander and by the CBA, deployed at the same and site, i.e., on pelitic and fresh organic matter-rich bottom sediments. Furthermore, these DIC flux values are very similar to those measured

in earlier studies using different benthic chamber devices [80–82] at the same site and in the same season (Figure 17).

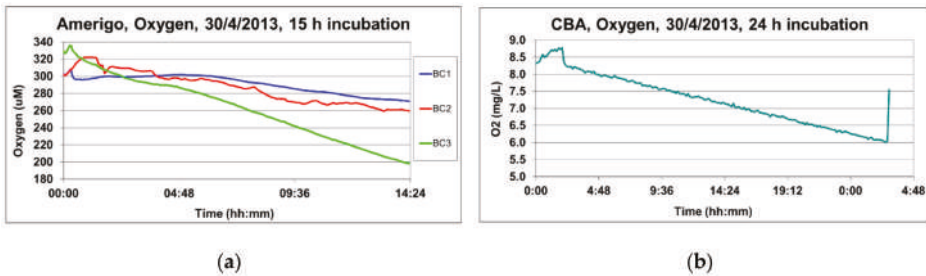


**Figure 16.** (a) Oxygen values recorded in the three benthic chambers of the Amerigo Lander (BC1, BC2, BC3) during deployment; (b) oxygen values recorded in the CBA during deployment of the two devices at the same time and site, a mud bottom sediment rich in fresh organic matter (Po River Prodelta).

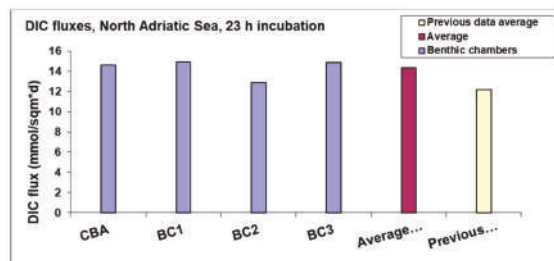


**Figure 17.** DIC fluxes measured by the CBA, by the Amerigo Lander (BC1, BC2, BC3), and in previous investigations at the same site, a mud bottom sediment rich in fresh organic matter (Po River Prodelta).

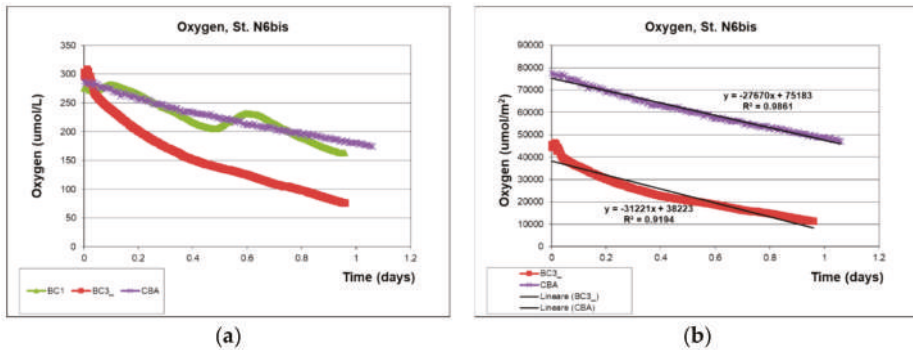
On the whole, the oxygen and DIC data reported above (and other solute flux data that are not shown but are available from the authors) demonstrate that the Amerigo Lander and the CBA provide very similar information on benthic fluxes of dissolved substances and that these data are comparable with flux information recorded in previous work conducted at the same site. These first data, therefore, provide very good support for the correct functioning of both our devices.

The Amerigo Lander and the CBA record oxygen concentrations in the different deployment phases. In particular, the oxygen sensors can monitor the oxygen concentrations inside the chambers, the oxygen fluxes at the sediment-water interface can be calculated, and, furthermore, the oxygen trend can be used to check the closing of the benthic chamber.

The trends of the oxygen concentrations recorded in the CBA and in two benthic chambers of the Amerigo Lander (BC1 and BC3) is shown in Figure 18. The data refer to the same time and station, on pelitic bottom sediment in front of the Po River Estuary.

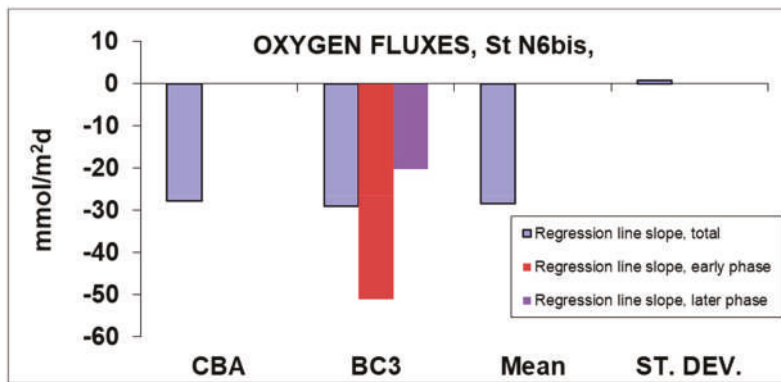
The declining oxygen concentration in the CBA and in the Ox3 chamber, due to benthic respiration or sediment-water interface fluxes, can be appreciated in Figure 18a. Notably, the two peaks in the oxygen concentration trend in the Ox1 chamber of the lander demonstrate that the lid opened twice.

In Figure 18b, the oxygen concentrations were multiplied by the height of the benthic chambers calculated by the dilution of the Cs tracer (4). The oxygen flux was then obtained by the slope of the regression line between time (days) and concentration ( $\mu\text{mol}/\text{m}^2$ ) (black line, Figure 18b).



**Figure 18.** (a) Oxygen concentrations measured in the CBA and in two benthic chambers (BC1 and BC3) of the Amerigo Lander at the same site, a mud bottom sediment rich in fresh organic matter (Po River Prodelta); (b) multiplication of the oxygen concentrations by the height of the benthic chamber of the CBA and in BC3 against time (days) allows calculating the benthic fluxes (slope of the regression line (black line of Figure 18b)).

The fluxes calculated by the slope of the regression line are shown in Figure 19 and Table 2. As demonstrated by the examination of Figure 18, the flux measured in the CBA is almost constant over the 24 h incubation. For this reason, only the total flux was calculated (Figure 19 and Table 2). In contrast, the oxygen concentration trend in BC3 shows a decreasing flux that can be divided into early (with higher values) and later (with lower values). This is due to the small size of the chamber of the lander, which is more responsive to changes in the environmental conditions inside the chamber, like the reduction in fresh reactive organic matter and oxygen consumption.

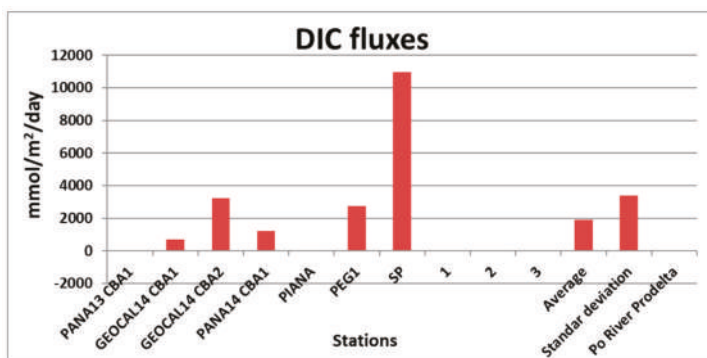


**Figure 19.** Oxygen fluxes calculated based on the data collected in the CBA and in the BC3 chamber of the Amerigo Lander. Deployment in front of the Po River Prodelta.

The CBA has also been deployed in a volcanic environment, at multiple sites on the seabed around the volcanic complex of Panarea, to measure the dissolved fluxes of DIC and metals released from the bottom in the gas vent area [39,43,44,54]. Figure 20 and Table 3 demonstrate the marked difference in DIC fluxes on the bottom between sites affected by vent fluxes (GEOCAL14CBA1, GEOCAL14CBA2, PANA14CBA1, PEG1, SP) and sites devoid of fluxes of dissolved substances at the sediment-water interface (PANA13CBA1, PIANA, 1, 2, 3), due to a surface layer of iron oxyhydroxide [39]. In addition, Figure 20 and Table 3 show very different DIC fluxes on the seafloor around the Panarea volcanic area, which is involved by vent fluxes, and the average DIC benthic fluxes measured in front of the Po River Estuary.

**Table 2.** Values of the oxygen fluxes at the sediment-water interface, calculated by the regression of all points (total), the phase with higher slope (early phase) and the lower slope (later phase).

	Regression Line Slope, Total	Regression Line Slope, Early Phase	Regression Line Slope, Later Phase
Oxygen		mmol/m <sup>2</sup> *days	
CBA	-27.670	-	-
BC3	-28.903	-51.087	-20.144
Mean	-28.287	-	-
ST. DEV.	0.872	-	-

**Figure 20.** DIC fluxes measured by the CBA in the submarine volcanic area of Panarea and in front of the Po River Prodelta.**Table 3.** Values of the DIC fluxes at the sediment-water interface measured by the CBA in the submarine volcanic area of Panarea and in front of the Po River Prodelta.

Cruise	Stations	Flux (mmol/m <sup>2</sup> ·d)
PANA13	PANA13 CBA1	60.60
GEOCAL14	GEOCAL14 CBA1	689.30
GEOCAL14	GEOCAL14 CBA2	3223.90
PANA14	PANA14 CBA1	1212.70
PANA15	PIANA	-17.99
PANA15	PEG1	2750.60
PANA15	SP	10978.00
PANA15B	1	61.54
PANA15B	2	-4.41
PANA15B	3	-19.29
	-	-
Average	-	1893.49
Standard deviation	-	3408.76
Po River Prodelta average	-	29.00

## 5. Conclusions

The Amerigo Lander and the CBA, two new instruments for measuring the benthic fluxes of dissolved substances, built by the authors, are presented herein. Both devices are autonomous and can

operate in shelf (CBA) and deep-sea (Amerigo Lander) environments. The Amerigo Lander can also be used for other investigations of shallow and deep benthic ecosystems, because it can carry several different instruments. Both devices have been successfully tested and employed in international and national research projects and in environmental investigations of anthropic impacts by local authorities. These tests and activities have demonstrated the sound performance of the Amerigo Lander and the CBA, as also reflected by the DIC and oxygen data reported above. The CBA has also proved suitable for deployment in a volcanic area affected by gas and fluid vents, for which very few data are available due to technical measurement difficulties. In case of use in volcanic environments, the temperature of the solutes released from the bottom should be carefully monitored because of the temperature operation limits of the sensors (40–50 °C) or of the polycarbonate (140 °C).

Notably, these new instruments mark an important advancement in the Italian marine technology community, providing the means to compete for international research and applicative projects at the same level as foreign institutions.

**Author Contributions:** The research article has been realized with the following individual contributions. Conceptualization, F.S. and V.M.; methodology, F.S., P.P., G.G., V.M. and L.M.; software, P.P. and F.S.; validation, F.S. and P.P.; formal analysis, F.S. and V.M.; investigation, F.S., P.P. and G.G.; resources, F.S. and V.M.; data curation, F.S., V.M. and P.P.; writing—original draft preparation, F.S. and P.P.; writing—review and editing, F.S. and P.P.; visualization, F.S.; supervision, F.S.; project administration, F.S. and V.M.; funding acquisition, F.S. and V.M.

**Funding:** Research was funded by the contribution of “Fondo di Ricerca per il Sistema Elettrico nell’ambito, Accordo di Programma RSE S.p.A.—Ministero dello Sviluppo Economico—D.G. Nucleare, Energie rinnovabili ed efficienza energetica”.

**Acknowledgments:** We should thank various people that have contributed in some way to the realization of the Amerigo Lander and of the CBA. In particular, we would to thank Giovanni Ciceri, Enrico Capodarca, Fabio Latini, and Massimo Cocciaretto for the fundamental help in the design phase; Patrizia Giordano, Laura Borgognoni, Massimo Leonetti, Franco Lanini, and Claudio Vannini, as well as the crew and the captains of the N/O Urania Emanuele Gentile and Vincenzo Lubrano Lavadera, and also the dive group of the Black Angels for their contributions in the experimental phases. A special thanks and a particular memory go to the mourned Giovanni Bortoluzzi for the infinite energy that transmitted to all of us.

**Conflicts of Interest:** The authors declare no conflict of interest. The funders had no role in the design of the study; in the collection, analyses, or interpretation of data; in the writing of the manuscript, or in the decision to publish the results.

## Appendix A

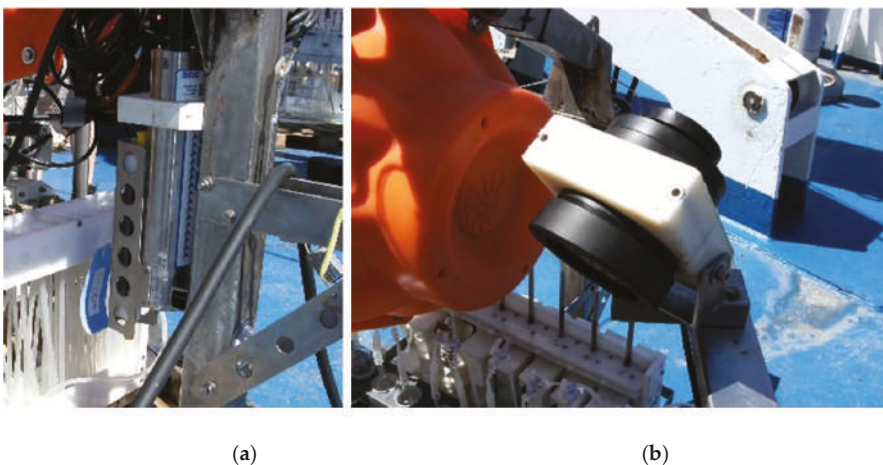


**Figure A1.** The Amerigo Lander monitoring instrumentation. (a) The SBE CTD mounted on the Amerigo tripod; (b) the Telesub Lanterna camera installed on the Amerigo Lander.

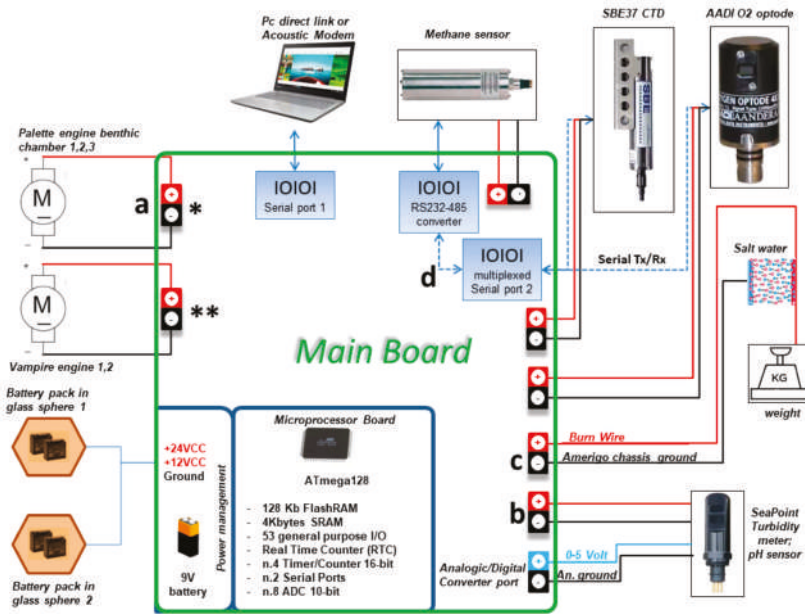


**Figure A2.** Electronics of the Amerigo Lander: Schematic drawing of the electronics diagram architecture. \* Multiplied by three (palettes); \*\* multiplied by two (VAMPIRE motors); a: dedicated POWER-ON/OFF port (H bridge with electronic shunt); b: other “n” analogic devices; c: other “n” burn wire systems; d: other “n” digital sensors; blue dashed line: serial Tx/Rx port.



**Figure A3.** The set of gas-impermeable glass ampoules for water sampling for the analysis of dissolved gases.



**Figure A4.** Filtering, subdivision into aliquots, and treatment of the water samples collected by the syringes of the Amerigo Lander is conducted in a Nitrogen glove-box.

**Table A1.** Main configuration of the Amerigo Lander electronic.

Type	Description
Microprocessor	ATmega128 RAM flash 128 Kb RAM 4Kb e2prom 4Kb Internal clock n. 3 timer 16 bit n. 8 ADC channels 10 bit
External circuit	n. 2 TTL serial ports serial flash RAM 4Mb n. 2 RS232 serial ports n. 3 RS485 ports n. 8 analogic inputs n. 2 digital inputsn. 20 on/off ports (H-bridge with electronic shunt)

**Table A2.** Configurations of the general inputs and outputs of the electronic of the Amerigo Lander.

Name	Type	Description
OUT 1	ON/OFF	Power terminals for CTD sensor
OUT 2	ON/OFF	Power terminals for O2 sensor number 1, chamber n.1
OUT 2	ON/OFF	Power terminals for O2 sensor number 2, chamber n.2
OUT 4	ON/OFF	Power terminals for O2 sensor number 3, chamber n.3
OUT 5	ON/OFF	Power terminals for CH4 sensor number 1, chamber n.1
OUT 6	ON/OFF	Power terminals for CH4 sensor number 2, chamber n.2
OUT 7	ON/OFF	Power terminals for CH4 sensor number 3, chamber n.3
OUT 8	ON/OFF	Power terminals for analogic sensors (n.2 turbidity and n.1pH)
OUT 9	ON/OFF	Power terminals - Engine palette chamber n.1 (mixing water)
OUT 10	ON/OFF	Power terminals - Engine palette chamber n.2 (mixing water)
OUT 11	ON/OFF	Power terminals -Engine palette chamber n.3 (mixing water)
OUT 12	ON/OFF	Engine VAMPIRONE number 1
OUT 13	ON/OFF	Engine VAMPIRONE number 2
OUT 14	ON/OFF	Burn wire n.1 Buoy electronic check
OUT 15	ON/OFF	Burn wire n.2 Benthic chamber release
OUT 16	ON/OFF	Burn wire n.3 Benthic chamber cover release
OUT 17	ON/OFF	Burn wire n.4 Benthic chamber cover release
OUT 18	ON/OFF	Burn wire n.5 weights release
OUT 19	ON/OFF	Power terminals 24 Volts for microprofiler
OUT 20	ON/OFF	OxyStat pump
RS232 1	RS232	Main serial port - PC communication
RS232 2-1	RS232	CTD
RS232 2-2	RS232	serial communication with O2 sensor n. 1, chamber n.1
RS232 2-3	RS232	serial communication with O2 sensor n. 2, chamber n.2
RS232 2-4	RS232	serial communication with O2 sensor n. 3, chamber n.3
RS232 2-5	RS232	serial communication with pH sensor n. 1, chamber n.1
RS232 2-6	RS232	serial communication with pH sensor n. 2, chamber n.2
RS232 2-7	RS232	serial communication with pH sensor n. 3, chamber n.3
RS485 1	RS485	serial communication with CH4 sensor n. 1, chamber n.1
RS485 2	RS485	serial communication with CH4 sensor n. 2, chamber n.2
RS485 3	RS485	serial communication with CH4 sensor n. 3, chamber n.3
an 1	analogical in	Analogical (0-5V) Turbidity sensor n. 1, chamber n.1
an 2	analogical in	Analogical (0-5V) Turbidity sensor n. 2, chamber n.2
an 3	analogical in	Analogical (0-5V) Turbidity sensor n. 3, chamber n.3
an 4	analogical in	NC-future purpose (pCO <sub>2</sub> )
an 5	analogical in	NC-future purpose (Eh)
an 6	analogical in	NC-future purpose (H <sub>2</sub> S)
an 7	analogical in	NC-future purpose (other sensor)
an 8	analogical in	NC-future purpose (other sensor)
DI 1	digital IN	magnetic sensor (future purpose, VAMPIRONE position)
DI 2	digital IN	magnetic sensor (future purpose, VAMPIRONE position)

## References

1. Douvere, F. The importance of marine spatial planning in advancing ecosystem-based sea use management. *Mar. Policy* **2008**, *32*, 762–771. [[CrossRef](#)]
2. Pérez-Albaladejo, E.; Rizzi, J.; Fernandes, D.; Lille-Langøy, R.; Goksøyr, A.; Oros, A.; Spagnoli, F.; Porte, C. Assessment of the environmental quality of coastal sediments by using a combination of in vitro bioassays. *Mar. Pollut. Bull.* **2016**, *108*, 53–61. [[CrossRef](#)] [[PubMed](#)]
3. Catalano, G.; Azzaro, M.; Bastianini, M.; Bellucci, L.G.; Bernardi Aubry, F.; Bianchi, F.; Burca, M.; Cantoni, C.; Caruso, G.; Casotti, R.; et al. The carbon budget in the northern Adriatic Sea, a winter case study. *J. Geophys. Res. Biogeosci.* **2014**, *119*, 1399–1417. [[CrossRef](#)]
4. Legendre, L. *Marine Biogeochemical Cycles*; John Wiley & Sons, Inc.: Hoboken, NJ, USA, 2014; pp. 145–187.

5. Pörtner, H.-O.; Karl, D.M.; Boyd, P.W.; Cheung, W.W.L.; Lluch-Cota, S.E.; Nojiri, Y.; Schmidt, D.N.; Zavalov, P.O. Ocean systems. In *Climate Change 2014: Impacts, Adaptation, and Vulnerability. Part A: Global and Sectoral Aspects. Contribution of Working Group II to the Fifth Assessment Report of the Intergovernmental Panel on Climate Change*; Field, C.B., Barros, V.R., Dokken, D.J., Mach, K.J., Mastrandrea, M.D., Bilir, T.E., Chatterjee, M., Ebi, K.L., Estrada, Y.O., Genova, R.C., et al., Eds.; Cambridge University Press: Cambridge, UK, 2014; pp. 411–484.
6. Gattuso, J.P.; Magnan, A.; Billé, R.; Cheung, W.W.; Howes, E.L.; Joos, F.; Allemand, D.; Bopp, L.; Cooley, S.R.; Eakin, C.; et al. Contrasting futures for ocean and society from different anthropogenic CO<sub>2</sub> emissions scenarios. *Science* **2015**, *349*, aac4722. [[CrossRef](#)] [[PubMed](#)]
7. Spagnoli, F.; Bergamini, M.C. Water-solid exchanges of nutrients and trace elements during early diagenesis and resuspension of anoxic shelf sediments. *Water Air Soil Pollut.* **1997**, *99*, 541–556. [[CrossRef](#)]
8. Apitz, S.E.; Bell, E.; Gilbert, F.; Hall, P.; Kershaw, P.; Nickell, L.; Parker, R.; Rabouille, C.; Shimmield, G.; Solan, M.; et al. Coastal Ocean Benthic Observatories (COBO): Integrated tools for the in situ observation and study of benthic ecosystem biogeochemical processes. In Proceedings of the 230th National Meeting of the American-Chemical-Society, Division of Geochemistry, in-situ Methods and Investigations in Environmental Science, Washington, DC, USA, 28 August–1 September 2005.
9. Apitz, S.E.; Bell, E.; Breuer, E.; Damgaard, L.; Gilbert, F.; Glud, R.; Hall, P.; Kershaw, P.; Lansard, B.; Nickell, L.; et al. Integrating new technologies for the study of benthic ecosystem response to human activity: Towards a Coastal Ocean Benthic Observatory (COBO). In Proceedings of the XVIII Congresso dell'Associazione Italiana di Oceanologia e Limnologia (AIOL), Napoli, Italy, 3–7 July 2006; Volume 19, pp. 73–78.
10. Spagnoli, F.; Marcaccio, M.; Frascari, F. Early diagenesis processes and benthic fluxes in different depositional environments of the Northern and Central Adriatic Sea. In Proceedings of the XVIII Congresso dell'Associazione Italiana di Oceanologia e Limnologia (AIOL), Napoli, Italy, 3–7 July 2006; Volume 19, pp. 483–487.
11. Spagnoli, F.; Bartholini, G.; Dinelli, E.; Marini, M.; Giordano, P. Early diagenesis of carbon and nutrients in sediments of the Gulf of Manfredonia (Southern Adriatic Sea). In *Marine research@CNR*; Brugnoli, E., Cavarretta, G., Mazzola, S., Trincardi, F., Ravaoli, M., Santoleri, R., Eds.; Consiglio Nazionale delle Ricerche, Dipartimento Terra & Ambiente: Roma, Italy, 2011; Volume DTA/06-2011, pp. 459–474.
12. Spagnoli, F.; Bartholini, G.; Marini, M.; Giordano, P. Biogeochemical processes in sediments of the Manfredonia Gulf (Southern Adriatic Sea): Early diagenesis of carbon and nutrient and benthic exchange. *Biogeosci. Discuss.* **2004**, *1*, 803–823. [[CrossRef](#)]
13. Spagnoli, F.; Bartholini, G.; Marini, M.; Giordano, P.; McCorkle, D.; Fiesoletti, F.; Specchiulli, A. Early diagenesis and benthic fluxes in Manfredonia Gulf (Southern Adriatic Sea). *Geochim. Cosmochim. Acta* **2004**, *68*, 348.
14. Berelson, W.M.; Hammond, D.E.; Smith, K.L.; Jahnke, R.A.; Devol, A.H.; Hinga, K.R.; Sayles, F. In situ benthic flux measurement devices-bottom lander technology. *Mar. Technol. Soc. J.* **1987**, *21*, 26–32.
15. Buchholtz-ten Brink, M.R.; Gust, G.; Chavis, D. Calibration and performance of a stirred benthic chamber. *Deep Sea Res. Part A Oceanogr. Res. Pap.* **1989**, *36*, 1083–1101. [[CrossRef](#)]
16. Glud, R.N.; Forster, S.; Huettel, M. Influence of radial pressure gradients on solute exchange in stirred benthic chambers. *Mar. Ecol. Prog. Ser.* **1996**, *141*, 303–311. [[CrossRef](#)]
17. Greinert, J.; Linke, P.; Sweetman, A. *Integrated Modular Systems for Monitoring of Ecosystem Functions in Deep-Sea Habitats with Relevance for Mining*; MIDAS: Itasca, IL, USA, 2015.
18. Parker, W.; Doyle, K.; Parker, E.; Kershaw, P.; Malcolm, S.; Lomas, P.; Kershaw, P. Benthic interface studies with landers. Consideration of lander/interface interactions and their design implications. *J. Exp. Mar. Boil. Ecol.* **2003**, *285*, 179–190. [[CrossRef](#)]
19. Priede, I.G.; Addison, S.; Bradley, S.; Bagley, P.M.; Gray, P.; Yau, C.; Witte, U. Autonomous deep-ocean lander vehicles; modular approaches to design and operation. In Proceedings of the IEEE Oceanic Engineering Society (OCEANS'98), Nice, France, 28 September–1 October 1998; Volume 3, pp. 1238–1244.
20. Tengberg, A.; De Bovee, F.; Hall, P.; Berelson, W.; Chadwick, D.; Ciceri, G.; Crassous, P.; Devol, A.; Emerson, S.; Gage, J.; et al. Benthic chamber and profiling landers in oceanography—A review of design, technical solutions and functioning. *Prog. Oceanogr.* **1995**, *35*, 253–294. [[CrossRef](#)]
21. Tengberg, A.; Stahl, H.; Gust, G.; Müller, V.; Arning, U.; Andersson, H.; Hall, P. Intercalibration of benthic flux chambers I. Accuracy of flux measurements and influence of chamber hydrodynamics. *Prog. Oceanogr.* **2004**, *60*, 1–28. [[CrossRef](#)]

22. Viollier, E.; Rabouille, C.; Apitz, S.; Breuer, E.; Chaillou, G.; Dedieu, K.; Furukawa, Y.; Grenz, C.; Hall, P.; Janssen, F.; et al. Benthic biogeochemistry: State of the art technologies and guidelines for the future of in situ survey. *J. Exp. Mar. Boil. Ecol.* **2003**, *285*, 5–31. [[CrossRef](#)]
23. Berg, P.; Glud, R.N.; Hume, A.; Ståhl, H.; Oguri, K.; Meyer, V.; Kitazato, H. Eddy correlation measurements of oxygen uptake in deep ocean sediments. *Limnol. Oceanogr. Methods* **2009**, *7*, 576–584. [[CrossRef](#)]
24. Berg, P.; Long, M.H.; Huettel, M.; Rheuban, J.E.; McGlathery, K.J.; Foreman, K.H.; Gibling, A.E.; Marino, R.; Howarth, R.W. Eddy correlation measurements of oxygen fluxes in permeable sediments exposed to varying current flow and light. *Limnol. Oceanogr.* **2013**, *58*, 1329–1343. [[CrossRef](#)]
25. Fones, G.R.; Davison, W.; Holby, O.; Thamdrup, B.; Jørgensen, B.B. High-resolution metal gradients measured by in situ DGT/DET deployment in Black Sea sediments using an autonomous benthic lander. *Limnol. Oceanogr.* **2001**, *46*, 982–988. [[CrossRef](#)]
26. Greeff, O.; Glud, R.N.; Gundersen, J.; Holby, O.; Jørgensen, B.B. A benthic lander for tracer studies in the sea bed: In situ measurements of sulfate reduction. *Cont. Shelf Res.* **1998**, *18*, 1581–1594. [[CrossRef](#)]
27. Miwa, T.; Iino, Y.; Tsuchiya, T.; Matsuura, M.; Takahashi, H.; Katsuragawa, M.; Yamamoto, H. Underwater observatory lander for the seafloor ecosystem monitoring using a video system. In Proceedings of the 2016 Techno-Ocean (Techno-Ocean), Kobe, Japan, 6–8 October 2016; pp. 333–336.
28. Best, M.M.; Favali, P.; Beranzoli, L.; Blandin, J.; Çağatay, N.M.; Cannat, M.; de Stigter, H. The EMSO-ERIC Pan-European Consortium: Data benefits and lessons learned as the legal entity forms. *Mar. Technol. Soc. J.* **2016**, *50*, 8–15. [[CrossRef](#)]
29. Chen, J.; Zhang, Q.; Zhang, A.; He, L.; Chen, Q. Sea trial and free-fall hydrodynamic research of a 7000-meter lander. In Proceedings of the OCEANS 2015-MTS/IEEE, Washington, DC, USA, 19–22 October 2015; pp. 1–5.
30. Chen, J.; Zhang, Q.; Zhang, A.; Tang, Y. 7000M lander design for hadal research. In Proceedings of the 2014 Oceans, St. John's, NL, Canada, 14–19 September 2014; pp. 1–4.
31. Hardy, K.; Cameron, J.; Herbst, L.; Bulman, T.; Pausch, S. Hadal landers: The Deepsea Challenge Ocean Trench Free Vehicles. In Proceedings of the 2013 OCEANS, San Diego, CA, USA, 23–27 September 2013; pp. 1–10.
32. Jamieson, A.J.; Fujii, T.; Solan, M.; Priede, I.G. HADEEP: Free-Falling Landers to the Deepest Places on Earth. *Mar. Technol. Soc. J.* **2009**, *43*, 151–160. [[CrossRef](#)]
33. Murashima, T.; Nakajoh, H.; Takami, H.; Yamauchi, N.; Miura, A.; Ishizuka, T. 11,000 m class free fall mooring system. In Proceedings of the Oceans 2009-Europe, Bremen, Germany, 11–14 May 2009; pp. 1–5.
34. Choi, J.K.; Fukuba, T.; Yamamoto, H.; Furushima, Y.; Miwa, T.; Kawaguchi, K. Pinpoint and Safe Installation of a Standalone Seafloor Observatory. In Proceedings of the 2018 OCEANS-MTS/IEEE Kobe Techno-Oceans (OTO), Kobe, Japan, 28–31 May 2018; pp. 1–4.
35. Pargett, D.M.; Jensen, S.D.; Roman, B.A.; Preston, C.M.; Ussler, W.; Girguis, P.R.; Scholin, C.A. Deep water instrument for microbial identification, quantification, and archiving. In Proceedings of the 2013 OCEANS, San Diego, CA, USA, 23–27 September 2013; pp. 1–6.
36. Wenzhöfer, F.; Wulff, T.; Floegel, S.; Sommer, S.; Waldmann, C. ROBEX-Innovative robotic technologies for ocean observations, a deep-sea demonstration mission. In Proceedings of the OCEANS 2016 MTS/IEEE, Monterey, CA, USA, 19–23 September 2016; pp. 1–8.
37. Williams, A.J. Expendable benthic lander (XBL). In Proceedings of the 2008 IEEE/OES US/EU-Baltic International Symposium, Tallinn, Estonia, 27–29 May 2008; pp. 1–8.
38. Berner, A. *Early Diagenesis: A Theoretical Approach*; Princeton University Press: Princeton, NJ, USA, 1980.
39. Hammond, D.E.; Fuller, C.; Harmon, D.; Hartman, B.; Korosec, M.; Miller, L.G.; Hager, S.W. Benthic fluxes in San Francisco bay. In *Temporal Dynamics of an Estuary: San Francisco Bay*; Springer: Dordrecht, The Netherlands, 1985; pp. 69–90.
40. Hammond, D.E.; McManus, J.; Berelson, W.M.; Kilgore, T.E.; Pope, R.H. Early diagenesis of organic material in equatorial Pacific sediments: Stoichiometry and kinetics. *Deep Sea Res.* **1996**, *43*, 1365–1412. [[CrossRef](#)]
41. Esposito, V.; Andaloro, F.; Canese, S.; Bortoluzzi, G.; Bo, M.; Di Bella, M.; Italiano, F.; Sabatino, G.; Battaglia, P.; Consoli, P.; et al. Exceptional discovery of a shallow-water hydrothermal site in the SW area of Basiluzzo islet (Aeolian archipelago, South Tyrrhenian Sea): An environment to preserve. *PLoS ONE* **2018**, *13*, e0190710. [[CrossRef](#)] [[PubMed](#)]

42. Spagnoli, F.; Andaloro, F.; Canese, S.; Capaccioni, B.; Esposito, V.; Giordano, P.; Romeo, T.; Bortoluzzi, G. Nuove recenti conoscenze sul sistema idrotermale del complesso vulcanico dell'Isola di Panarea (Arcipelago delle Eolie, Mar Tirreno Meridionale) New recent insights of the hydrothermal system of the Panarea Island (Aeolian Archipelago, South Tyrrhenian Sea). *Mem. Descr. Carta Geol.* **2019**, *105*, 85–90.
43. Berelson, W.; Hammond, D.; Johnson, K.; Johnson, K. Benthic fluxes and the cycling of biogenic silica and carbon in two southern California borderland basins. *Geochim. Cosmochim. Acta* **1987**, *51*, 1345–1363. [[CrossRef](#)]
44. Cummins, K.M.; McManus, J.; Smith, G.; Spagnoli, F.; Hammond, D.E.; Cummins, K.M.; Berelson, W.M. Methods for measuring benthic nutrient flux on the California Margin: Comparing shipboard core incubations to in situ lander results. *Limnol. Oceanogr. Methods* **2004**, *2*, 146–159.
45. Hammond, D.; Giordani, P.; Berelson, W.; Poletti, R. Diagenesis of carbon and nutrients and benthic exchange in sediments of the Northern Adriatic Sea. *Mar. Chem.* **1999**, *66*, 53–79. [[CrossRef](#)]
46. Berelson, W.; Hammond, D. The calibration of a new free-vehicle benthic flux chamber for use in the deep sea. *Deep. Sea Res. Part A Oceanogr. Res. Pap.* **1986**, *33*, 1439–1454. [[CrossRef](#)]
47. Black, K.S.; Fones, G.R.; Peppe, O.C.; Kennedy, H.A.; Bentaleb, I. An autonomous benthic lander: Preliminary observations from the UK BENBO thematic programme. *Cont. Shelf Res.* **2001**, *21*, 859–877. [[CrossRef](#)]
48. Devol, A.H. Verification of flux measurements made with in situ benthic chambers. *Deep. Sea Res. Part A Oceanogr. Res. Pap.* **1987**, *34*, 1007–1026. [[CrossRef](#)]
49. Ferrón, S.; Alonso-Pérez, F.; Castro, C.G.; Ortega, T.; Pérez, F.F.; Ríos, A.F.; Forja, J.M. Hydrodynamic characterization and performance of an autonomous benthic chamber for use in coastal systems. *Limnol. Oceanogr. Methods* **2008**, *6*, 558–571. [[CrossRef](#)]
50. Ishida, H.; Watanabe, Y.; Fukuhara, T.; Kaneko, S.; Furusawa, K.; Shirayama, Y. In situ Enclosure Experiment Using a Benthic Chamber System to Assess the Effect of High Concentration of CO<sub>2</sub> on Deep-Sea Benthic Communities. *J. Oceanogr.* **2005**, *61*, 835–843. [[CrossRef](#)]
51. Jahnke, R.; Christiansen, M. A free-vehicle benthic chamber instrument for sea floor studies. *Deep. Sea Res. Part A Oceanogr. Res. Pap.* **1989**, *36*, 625–637. [[CrossRef](#)]
52. Lee, J.S.; An, S.-U.; Park, Y.-G.; Kim, E.; Kim, D.; Kwon, J.-N.; Kang, D.-J.; Noh, J.-H. Rates of total oxygen uptake of sediments and benthic nutrient fluxes measured using an in situ autonomous benthic chamber in the sediment of the slope off the southwestern part of Ulleung Basin, East Sea. *Ocean Sci. J.* **2015**, *50*, 581–588. [[CrossRef](#)]
53. Sayles, F.; Dickinson, W. The ROLA<sup>2</sup>D lander: A benthic lander for the study of exchange across the sediment-water interface. *Deep. Sea Res. Part A Oceanogr. Res. Pap.* **1991**, *38*, 505–529. [[CrossRef](#)]
54. Smith, K.L.; Clifford, C.H.; Eliason, A.H.; Walden, B.; Rowe, G.T.; Teal, J.M. A free vehicle for measuring benthic community metabolism. *Limnol. Oceanogr.* **1976**, *21*, 164–170. [[CrossRef](#)]
55. Smith, K.L., Jr.; White, G.A.; Laver, M.B. Oxygen uptake and nutrient exchange of sediments measured in situ using a free vehicle grab respirometer. *Deep Sea Res. Part A Oceanogr. Res. Pap.* **1979**, *26*, 337–346. [[CrossRef](#)]
56. Spagnoli, F.; Giuliani, G.; Martinotti, V.; Masini, L.; Penna, P. AMERIGO and CBA: A new lander and a new automatic benthic chamber for dissolved benthic flux measurements. In Proceedings of the 2018 IEEE International Workshop on Metrology for the Sea, (MetroSea 2018), Bari, Italy, 8–10 October 2018; ISBN 978-1-5386-7643-1.
57. Morris, R.; Hardy, K. Selecting an acoustic release for a mooring or lander. In Proceedings of the OCEANS 2017, Anchorage, AK, USA, 18–21 September 2017; pp. 1–5.
58. Phleger, C.F.; Soutar, A. Free vehicles and deep-sea biology. *Am. Zool.* **1971**, *11*, 409–418. [[CrossRef](#)]
59. Morse, J.W.; Boland, G.; Rowe, G.T. A 'gilled' benthic chamber for extended measurement of sediment-water fluxes. *Mar. Chem.* **1999**, *66*, 225–230. [[CrossRef](#)]
60. Giordano, P.; Spagnoli, F.; Marcaccio, M.; Marini, M.; Frascari, F.; Modica, A.; Rivas, G. Il Mar Piccolo di Taranto: Osservazioni preliminari sul ciclo dei nutrienti all'interfaccia acqua—Sedimento. *Atti Della Assoc. Ital. Oceanol. Limnol.* **2004**, *17*, 59–70.
61. Masini, L.; Spagnoli, F.; Marcaccio, M.; Frascari, F. *Prototipo di Camera Benthica Automatica per Bacini Acquatici Continentali e Marini*; Consiglio Nazionale delle Ricerche, Istituto di Geologia Marina: Bologna, Italy, 2001.
62. Berelson, W.; Hammond, D.; O'Neill, D.; Xu, X.-M.; Chin, C.; Zuckin, J. Benthic fluxes and pore water studies from sediments of the central equatorial north Pacific: Nutrient diagenesis. *Geochim. Cosmochim. Acta* **1990**, *54*, 3001–3012. [[CrossRef](#)]

63. Spagnoli, F. *AMERIGO: A Deep Sea Lander. CNR Marine Research Activities and Technologies, Thematics: Technologies*; Consiglio Nazionale delle Ricerche, Dipartimento Terra & Ambiente: Rome, Italy, 2010.
64. Spagnoli, F.; Andresini, A.; Borgognoni, L.; Bortoluzzi, G.; Campanelli, A.; Canonico, C.; Ferrante, V.; Giuliani, G.; Giordano, P.; Greco, M.; et al. *Campagna Oceanografica CASE4; Rapporto Finale di Crociera*; ISMAR-CNR: Ancona, Italy, 2012.
65. Spagnoli, F.; Allende Ccori, J.; Andresini, A.; Borgognoni, L.; Ferrante, V.; Giordano, P.; Pignotti, E.; Zuzolo, M.G. *Campagna Oceanografica PER1; Rapporto Finale di Crociera*; CNR-ISMAR: Ancona, Italy, 2013; p. 33.
66. Spagnoli, F.; Ciceri, G.; Giuliani, G.; Martinotti, V.; Penna, P. AMERIGO: A new benthic lander for dissolved flux measurements at sediment-water-interface. In *Proceedings of the Goldschmidt 2013, Florence, Italy, 25–30 August 2013*; Volume 77, p. 2242.
67. Spagnoli, F.; Giuliani, G.; Penna, P.; Martinotti, V. AMERIGO, a lander for benthic flux and chemical and physical parameter measurements and for the sampling of water and sediment at the sediment-water interface. In *Le Tecnologie del CNR per il Mare*; Consiglio Nazionale delle Ricerche CNR: Roma, Italy, 2013.
68. Spagnoli, F.; Bartholini, G.; Capaccioni, B.; Giordano, P. Benthic Nutrient Fluxes in Central and Southern Adriatic and Ionian Seas. In *Proceedings of the 40th CIESM Congress, Marseille, France, 28 October–1 November 2013*.
69. Spagnoli, F.; Borgognoni, L.; Campanelli, A.; Ciceri, G.; Martinotti, V.; Giordano, P.; Giuliani, G.; Penna, P. A new biogeochemical method for the monitoring of possible seeps in marine CCS fields. In *Proceedings of the Geoitalia 2013—Le Geoscienze per la Società, IX edizione del Forum Italiano di Scienze della Terra, Pisa, Italy, 16–18 September 2013*.
70. Spagnoli, F.; Ciceri, G.; Giordano, P.; Martinotti, V.; Politi, M. Experimental biogeochemical approach to the monitoring of baseline levels of CO<sub>2</sub> fluxes at the sediment-water interface for CCS purpose. In *Proceedings of the Geoitalia 2011, VIII Forum Italiano di Scienze della Terra, Torino, Italy, 19–23 September 2011*.
71. Spagnoli, F.; Kaberi, H.; Giordano, P.; Zeri, C.; Borgognoni, L.; Bortoluzzi, G.; Campanelli, A.; Ferrante, V.; Giuliani, G.; Martinotti, V.; et al. Benthic fluxes of dissolved heavy metals in polluted sediments of the Adriatic Sea. In *Proceedings of the Scientific Conference: Integrated Marine Research in the Mediterranean and the Black Sea, Bruxelles, Belgium, 7–9 December 2015*; pp. 301–302, ISBN 978-960-9798-25-9.
72. Spagnoli, F.; Bartholini, G.; Giordano, P. Benthic fluxes and early diagenesis processes in Adriatic Sea. Sessione poster. In *Proceedings of the Goldschmidt 2013, Florence, Italy, 25–30 August 2013*.
73. Bortoluzzi, G.; Spagnoli, F.; Aliani, S.; Romeo, T.; Canese, S.; Esposito, V.; Grassi, M.; Masetti, G.; Djaliti, L.; Cocchi, L.; et al. New geological, geophysical and biological insights on the hydrothermal system of the Panarea—Basiluzzo Volcanic complex (Aeolian Islands, Tyrrhenian Sea). In *Proceedings of the SGI-SIMP, Milan, Italy, 10–12 September 2014*.
74. Spagnoli, F.; Borgognoni, L.; Acri, F.; Caccamo, G.; De Marco, R.; Leonetti, M. *Indagini del Fondale del Porto di Fano a Mezzo di Camera Bentica Valutazione Degli Effetti del Dragaggio sui Sedimenti Marini. Fase Post-Operam*; Technical Report; Istituto di Scienze Marine del CNR: Ancona, Italy, 2016.
75. Spagnoli, F.; Giordano, P.; Borgognoni, L.; Acri, F. *Studi di Carattere Ambientale Volti a Valutare le Dinamiche e gli Effetti Ambientali dei Sedimenti Marini Provenienti da Escavi Portuali. Valutazione degli Effetti del Dragaggio sui Sedimenti Marini. Fase Post-Operam*; Technical Report; Istituto di Scienze Marine del CNR: Ancona, Italy, 2016.
76. Giordano, P.; Spagnoli, F.; Langone, L.; Misericocchi, S.; Ferrante, V.; Vasumini, I.; Graziani, G.; Savelli, F.; Dalpasso, E.; De Marco, M. *Rapporto delle Attività di Campagna, Campagna RID16*; Istituto di Scienze Marine: Venice, Italy, 2016.
77. Rovere, M.; Argani, A.; Mercorella, A.; Spagnoli, F.; Frapiccini, E.; Pellegrini, C.; Ciccone, F.; Zaniboni, F.; Pagnone, G.; Paparo, M.A.; et al. *Accordo Operativo 2016 tra Consiglio Nazionale delle Ricerche—Istituto di Scienze Marine (ISMAR CNR) e Ministero dello Sviluppo Economico, Direzione Generale per la Sicurezza Anche Ambientale delle Attività Minerarie ed Energetiche—Ufficio Nazionale Minerario per gli Idrocarburi e le Georisorse (DGS-UNMIG)*; Istituto di Scienze Marine di Bologna: Bologna, Italy, 2018.
78. Frascari, F.; Spagnoli, F.; Marcaccio, M.; Giordano, P. Anomalous Po River flood event effects on sediments and the water column of the northwestern Adriatic Sea. *Clim. Res.* **2006**, *31*, 151–165. [[CrossRef](#)]
79. Spagnoli, F.; Dinelli, E.; Giordano, P.; Marcaccio, M.; Zaffagnini, F.; Frascari, F. Sedimentological, biogeochemical and mineralogical facies of Northern and Central Western Adriatic Sea. *J. Mar. Syst.* **2014**, *139*, 183–203. [[CrossRef](#)]

80. Spagnoli, F.; Dell'Anno, A.; De Marco, A.; Dinelli, E.; Fabiano, M.; Gadaleta, M.V.; Ianni, C.; Lolacono, F.; Manini, E.; Marini, M.; et al. Biogeochemistry, grain size and mineralogy of the central and southern Adriatic Sea sediments: A review. *Chem. Ecol.* **2010**, *26*, 19–44. [[CrossRef](#)]
81. Spagnoli, F.; Frascari, F.; Marcaccio, M.; Bergamini, M.C. Early diagenesis and nutrient benthic fluxes in the Adriatic Sea. *Geophys. Res. Abstr.* **2003**, *5*, 12257.
82. Capet, A.; Lazzari, P.; Spagnoli, F.; Bolzon, G.; Solidoro, C. Benthic contributions to Adriatic and Mediterranean biogeochemical cycles. *EGU Gen. Assem. Conf. Abstr.* **2017**, *19*, 17596.



© 2019 by the authors. Licensee MDPI, Basel, Switzerland. This article is an open access article distributed under the terms and conditions of the Creative Commons Attribution (CC BY) license (<http://creativecommons.org/licenses/by/4.0/>).



Article

# Towards Non-Invasive Methods to Assess Population Structure and Biomass in Vulnerable Sea Pen Fields <sup>†</sup>

Giovanni Chimienti <sup>1,\*</sup>, Attilio Di Nisio <sup>2</sup>, Anna M. L. Lanzolla <sup>2</sup>, Gregorio Andria <sup>2</sup>, Angelo Tursi <sup>1</sup> and Francesco Mastrototaro <sup>1</sup>

<sup>1</sup> Department of Biology and CoNISMa LRU, University of Bari Aldo Moro, 70125 Bari, Italy; angelo.tursi@uniba.it (A.T.); francesco.mastrototaro@uniba.it (F.M.)

<sup>2</sup> Department of Electrical & Information Engineering (DEI), Polytechnic University of Bari, 70125 Bari, Italy; attilio.dinisio@poliba.it (A.D.N.); anna.lanzolla@poliba.it (A.M.L.L.); gregorio.andria@poliba.it (G.A.)

\* Correspondence: giovanni.chimienti@uniba.it; Tel.: +39-080-544-3344

<sup>†</sup> This paper is extended version of the conference paper Biometric relationships in the red sea pen *Pennatula rubra* (Cnidaria: Pennatulacea).

Received: 8 April 2019; Accepted: 13 May 2019; Published: 15 May 2019

**Abstract:** Colonies of the endangered red sea pen *Pennatula rubra* (Cnidaria: Pennatulacea) sampled by trawling in the northwestern Mediterranean Sea were analyzed. Biometric parameters, such as total length, peduncle length, number of polyp leaves, fresh weight, and dry weight, were measured and related to each other by means of regression analysis. Ad hoc models for future inferencing of colonies size and biomass through visual techniques were individuated in order to allow a non-invasive study of the population structure and dynamics of *P. rubra*.

**Keywords:** corals; Pennatulacea; *Pennatula*; model; Mediterranean Sea; biometry; ROV; trawling; fishery; VME

## 1. Introduction

The mesophotic and aphotic zones of the Mediterranean Sea are inhabited by a variety of benthic organisms, some of which are able to create biogenic habitats due to their three-dimensionality and their aggregative behavior. Among them, corals play a crucial role as habitat formers, being the main builders of peculiar coral frameworks, in the case of stony corals [1], or coral forests, in the case of arborescent corals [2,3]. These habitats are featured by a high sensitivity to human pressures, particularly on trawlable grounds, where their abundance and their associated community significantly decrease [4]. Among soft-bottom octocorals, pennatulaceans can form extensive populations, known as sea pen fields, providing relevant structure in flat, low-relief muddy habitats where there is little physical habitat complexity. These fields create essential biogenic habitat for suprabenthic and benthic invertebrates, as well as an important feeding and nursery area for a rich demersal fish fauna [5–8] representing Essential Fish Habitats and Vulnerable Marine Ecosystems (VMEs) [9] worthy of protection.

Sea pen fields are often difficult to be found on muddy bottoms using indirect methods because they cannot be detected using the common habitat mapping geophysical techniques. The most effective way to identify these fields, through the analysis of data coming from commercial fishing bycatch or from experimental trawl fishing surveys, on a large scale still remains trawling. After the identification of a sea pen field, the visual techniques used onboard oceanographic cruises, such as Remotely Operated Vehicles (ROVs), allow to carry out more detailed studies and/or monitoring of VMEs on a relatively small area [10]. Non-contact and non-destructive imaging techniques, based on properly developed object segmentation and detection algorithms, have been proved to be a viable alternative to contact measurement and diagnostic techniques in a large variety of sectors, ranging from industrial quality control to characterization of devices, to medical imaging and clinical applications.

Hence, it is foreseeable the development of automatic vision methods for identification, counting, and measurement of the sea [11–20].

Despite the recognized ecological importance of pennatulaceans, little is known about their biology and ecology, and their vulnerability to human pressures has been assessed under a precautionary approach [21]. Destructive sampling is still needed to estimate the biomass of a sea pen field, as well as to collect information on colonies' size, population structure, and dynamics, in order to assess the main features of the population and to establish its need for protection. Nowadays, advances in the design, lowering of costs, and increased performance of unmanned vehicles, including ROVs and drones, pave the way to the extended exploration of marine environments [22–28]. Underwater imagery techniques, such as ROVs and towed cameras, are now allowing a better understanding of the sea pen numerical importance on a relatively small scale, but these methods are still not effective in understanding biomass and size structure [10]. Hence, the development of a non-invasive technique for determining the weight of colonies is desirable to obtain quantitative data of biomass (both fresh and dry) from ROV imaging, useful to support conservation measures. Moreover, the possibility to estimate the colonies' length with the same approach would also enhance the size structure assessment of sea pens population and their monitoring, consistently with their need of protection and their fragility to the trawled sampling gears (e.g., trawl nets and dredges). Finding of proper biometric correlations could avoid the need of further sampling for the study of these vulnerable populations in the near future [29], allowing non-invasive methods, and representing a valid alternative to destructive sampling.

The present study modeled the biometric measurements collected from a population of the red sea pen *Pennatula rubra* (Ellis, 1761) sampled by trawling. This species, endemic of the Mediterranean Sea, belongs to the suborder Subsessiliflorae because of the presence of polyps disposed in pinnately arranged leaves. It represents one of the most important field-forming sea pens of the Mediterranean continental shelf [30,31], reported as vulnerable in the Red List of the International Union for the Conservation of Nature (IUCN) [32] among the seventeen threatened coral species of the basin. The colonies of *P. rubra* live with the peduncle (i.e., the basal part of the colony) into the sediment, the rachis representing most of the visible portion of the colony (Figure 1). For this reason, the total length cannot be directly measured through visual methods. In this study, we found reliable biometric relationships using the number of polyp leaves as a proxy to estimate the total length and the biomass of the colonies, enabling future in situ assessments of population structure and biomass. This would also avoid the need for sampling for the study of the population dynamic of *P. rubra*, representing a necessary knowledge base for a non-invasive study of the wild populations.

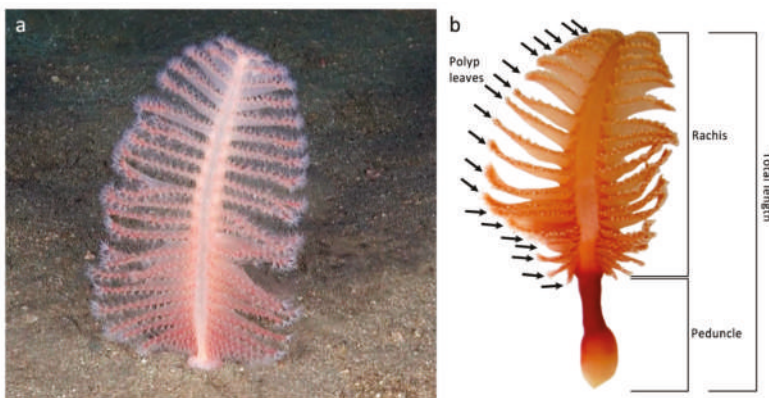


**Figure 1.** The colony of *Pennatula rubra*. (a) In vivo appearance of the species; (b) indication of polyp leaves (black arrows), rachis, peduncle, and total length.

## 2. Materials and Methods

Colonies of *P. rubra* were sampled using an experimental trawl net, with a stretched mesh of 20 mm in the codend, in the frame of the MEDITS (Mediterranean International Bottom Trawl Survey) project [33]. Sampling was carried out during 2013 northwest Punta Alice (Ionian Sea, southern Italy; start: 39°35.05'N–16°52.26'E; end: 39°34.05'N–16°53.63'E) at 61–65 m depth [31], onboard the *Pasquale e Cristina* fishing vessel. A SCANMAR acoustic system (Scanmar AS, Åsgårdstrand, Norway) [34] was used to measure the horizontal and vertical openings of the net in order to estimate the swept area. The colonies of *P. rubra* sampled were preserved on board at  $-20^{\circ}\text{C}$ .

A total of 168 colonies, sampled over an area of 41,000 m<sup>2</sup>, were analyzed. The following biometric parameters were measured for each colony: length of the peduncle, the total length of the colony (considering both rachis and peduncle), fresh weight, and number of polyp leaves (Figure 1). Length measures were carried out using a manual caliber with 1 mm resolution, and fresh weight was measured using a DENVER MXX-212 electronic balance (Denver Instrument GmbH, Goettingen, Germany; 0.01 g resolution, 0.04 g worst-case uncertainty).

Measurements were carried out in the laboratory after thawing, considering that the freezing process causes the complete contraction of the colonies. On the contrary, living colonies can contain a highly variable quantity of seawater driving their contraction and considerably changing their size and fresh weight [31]. Then, a suitable procedure to obtain dry weight measurement was performed for a reduced number of sampled colonies. In particular, 54 colonies were selected having different fresh weight values to obtain a statistically significant population. Each colony was identified by a unique ID and fresh weighted, and then the colonies were dried in an oven at 40 °C for 96 h. Dry weight was measured for each colony. A detailed study highlighting the relationship among all the biometric parameters of *P. rubra* was performed, with the aim to develop suitable models for the colonies' size and fresh weight based on the number of polyp leaves. The model for the estimation of size was developed to obtain both the rachis length and the total length, the former being visible with imagery techniques (Figure 1), while the latter used in direct measurements from samples. Moreover, the relationship between fresh and dry weight of the colonies was also assessed. Finally, data obtained from an ROV survey carried out on the same population sampled by trawling [10] were used to compare the distribution of the number of polyp leaves obtained from both the methods (i.e., visual vs. sampling). In particular, polyp leaves were counted for a total of 207 colonies observed in vivo, whose position, contraction, and ROV framing allowed to clearly distinguish the polyp leaves of at least one side of the colony.

Although it is not very common, the number of polyp leaves from the two sides of the same colony can be different due to mechanical damage or predation events. For this reason, both right and left polyp leaves of each sampled colony were counted. When the number of leaves was different between the two sides of the same colony, the mean value was calculated and used for the models. Whereas, the maximum number of polyp leaves per colony side was preferred over the mean value for the size estimation model, considering the direct link between the length of the colony and the number of polyp leaves.

## 3. Results and Discussion

The number of polyp leaves proved to be a reliable proxy to estimate size and biomass of *P. rubra* colonies using non-invasive approaches based on ROV imaging, as previously highlighted with regression analysis [10,29]. In particular, the analysis of colonies sampled through experimental trawl fishing surveys allowed to identify suitable relationships, which were able to estimate the size and biomass of sea pens using models based on the number of polyp leaves, that can be measured from images.

### 3.1. Model for Size Estimation

In the first step, the relationship between rachis length and the number of polyp leaves was investigated. The experimental results highlighted a good linear behavior (correlation coefficient = 0.84) between number  $n$  of polyp leaves and the estimated rachis length as reported below in Equations (1) and (2) and shown in Figure 2.

$$l_r = l_t - l_p \quad (1)$$

$$\hat{l}_r(n) = 2.6 \cdot n - 1.1 \quad (2)$$

where  $l_t$  is the total length of the colony,  $l_p$  is the length of the peduncle,  $n$  is the number of polyp leaves, and  $l_r$  and  $\hat{l}_r$  are rachis length and its estimation by means of linear regression, respectively.

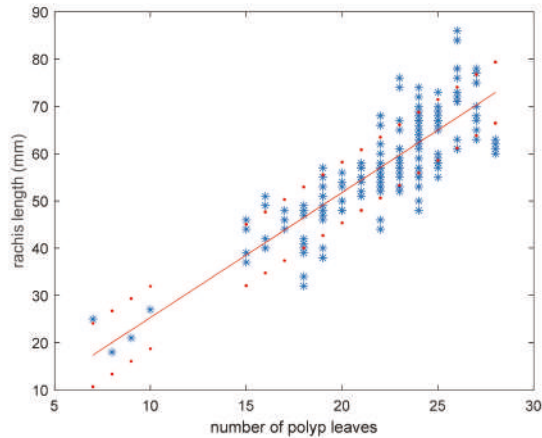


**Figure 2.** Rachis length vs. the number of polyp leaves in *Pennatula rubra*; the red line is the linear regression, and red dot lines include 95% of data.

To quantify the accuracy of the proposed model, the root mean square relative error  $e_{l_r}$  was calculated by using Equation (3), then a value of 11.8% for this parameter was obtained. This value is due to intraspecific variability, and it can be accepted for size-frequency distribution analysis in soft coral populations.

$$e_{l_r} = \sqrt{\frac{1}{M} \sum_i^M \left( \frac{\hat{l}_r(n_i) - l_{r_i}}{l_{r_i}} \right)^2} \quad (3)$$

In Equation (3),  $M$  is the number of samples,  $n_i$  and  $l_{r_i}$  are the values of polyp leaves number and rachis length of the  $i$ -th sample, respectively. Experimental values are equally distributed around the regression line (Figure 2).

Figure 2 shows a significant variation in colony length for each value of the number of polyp leaves; therefore the dispersion of obtained data was analyzed. Figure 3 shows the distribution of  $l_r$  values grouped for each  $n$ , where mean and standard deviation were represented with a box plot. The values with  $n < 15$  were not included in the dispersion analysis because they did not provide length variation in correspondence of the same values of  $n$ . In general, colonies with a high number of polyp leaves provide more dispersion, with a maximum standard deviation value of 8.2 mm. This can be due to intraspecific variability, particularly evident in older colonies whose number of polyp leaves is higher.

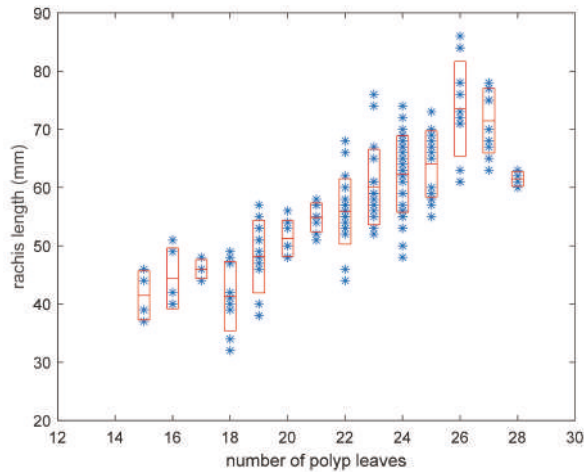


**Figure 3.** Distribution of rachis length in the population of *Pennatula rubra*; red boxes include all values ranging in average  $\pm$  standard deviation.

Similar linear dependence was obtained by analyzing the behavior of total length estimate  $\hat{l}_t$  as a function of the number of polyp leaves, reported in Equation (4), with an obtained root mean square relative error of 10.6%.

$$\hat{l}_t(n) = 5.8 \cdot n + 8.1 \tag{4}$$

The major or minor variation of rachis length for each value of the number of polyp leaves can be due to the natural variability of the population and the number of colonies sampled. Despite a large number of samples analyzed (168 colonies), it is expected that the rachis length variation among the different values of the number of polyp would be more homogeneous by analyzing a larger number of colonies.

### 3.2. Model for Fresh Weight Estimation

The number of polyp leaves was related to the fresh weight of *P. rubra* colonies and served as a model to assess colonies' biomass. A suitable *P. rubra* envelop was considered in order to identify the best curve for data fitting. In particular, by supposing a 2D outline of *P. rubra*, it is possible to consider a second order enveloping curve expressed as a function of distance along the rachis, as shown in Figure 4. The curve intersects the rachis at distances zero and  $l_r$ .

The weight  $\hat{w}_f$  of a *P. rubra* colony is assumed to be proportional to the enveloping area, and consequently can be expressed by integrating that curve between 0 and  $l_r$ , obtaining a third-degree power of  $l_r$ . Therefore, by taking into account the linear dependence between length and the number of polyp leaves, the dependence of fresh weight from  $n$  can be described by a third-degree polynomial, where all powers of  $n$  up to the third have been considered for generality (Figure 5).

Tests consisting of the use of different nonlinear models confirmed that the best fitting curve providing the minimum mean square error is expressed by the following relationship, corresponding to a root mean square relative error of 46%:

$$\hat{w}_f(n) = -0.013 \cdot n^3 + 0.076 \cdot n^2 - 1.170 \cdot n + 5.342 \tag{5}$$

The validity of the model was not assured when  $n < 15$  because the weight estimated in this condition required a higher number of data from juvenile or young colonies and a more accurate weight measurement with very low values. Anyway, small colonies resulted infrequent with both

trawling and visual methods, and their contribution to the biomass of the sampled population is about 0.06% of the mass.

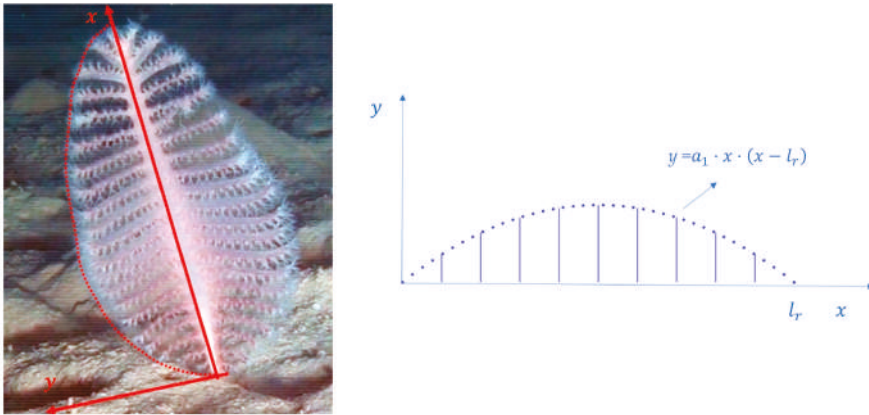


Figure 4. 2D outline of *Pennatula rubra*.

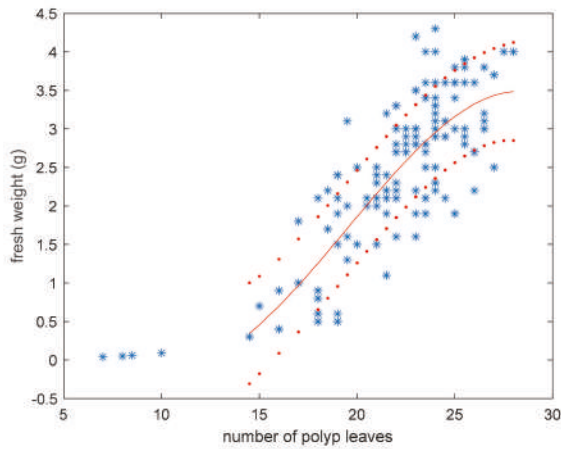
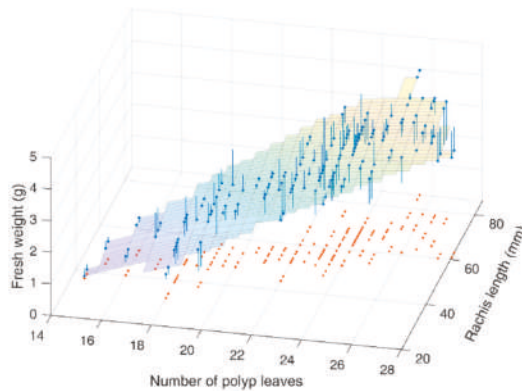


Figure 5. Fresh weight vs. the number of polyp leaves in *Pennatula rubra*; red curve is the third-degree polynomial fitting experimental data, and red dot curves include 95% of data.

A further model of the estimated weight  $\hat{w}_{2f}$ , taking into account also the linear dependence on rachis length, was considered with the aim to reduce the fitting error (Equation (6)). The following fitting surface was identified, as shown in Figure 6.

$$\hat{w}_{2f}(n, l_r) = 2.28 \cdot 10^{-4} \cdot n^3 - 0.023 \cdot n^2 + 0.826 \cdot n + 0.039 \cdot l_r - 9.182 \quad (6)$$

In this way, the root mean square relative error was reduced to 38.7%.



**Figure 6.** The behavior of fresh weight as a function of both the number of polyp leaves and rachis length in *Pennatula rubra*. Blue bars represent errors between measured weight and least squares surface fitting. Red dots are projections on the horizontal plane.

### 3.3. Dry Weight Estimation

The correlation between dry and fresh weight was analyzed based on measurement data on a reduced set of *P. rubra* samples represented by 54 colonies. Despite the fact that the dry weight is not frequently used for sea pens, it is considered a more reliable measure of the biomass because of the variable water content in living colonies of *P. rubra*, driving their exposure to different currents and their withdrawal as a defense strategy [31].

Figure 7 shows fresh weight behavior vs. dry weight, which can be described by means of a polynomial function of the third order expressed by means of

$$\hat{w}_d(n) = 0.062 \cdot w_f^3 - 0.412 \cdot w_f^2 + 1.134 \cdot w_f - 0.416 \tag{7}$$

where  $w_f$  is the measured fresh weight, and  $\hat{w}_d$  is the dry weight estimation.

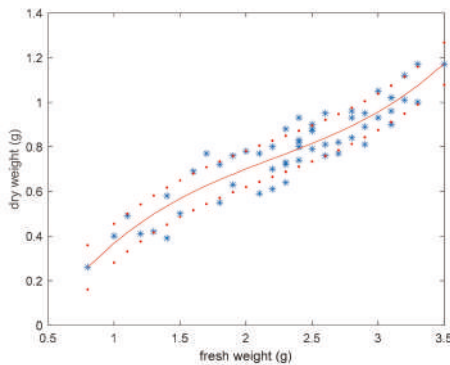


**Figure 7.** Fresh weight vs. dry weight in *Pennatula rubra*; the red curve is the polynomial interpolation of the third order, and red dot curves include 95% of data.

The obtained model allows to predict dry weight based on the fresh weight and shows root mean square relative error of 19.2%. This can allow the use of the model to assess dry biomass starting from both fresh weight estimation (e.g., from ROV imaging) or direct fresh weight measures (e.g., from

fishery samples). In this last case, the model would help to rapidly understand the dry biomass of a sea pen field (e.g., onboard a fishing vessel) without the need of drying procedures.

### 3.4. Distribution of the Number of Polyp Leaves

Starting from ROV imaging data,  $n_i$ , the number of polyp leaves of the  $i$ -th colony, was counted for each of the  $M = 207$  *P. rubra* colonies observed and analyzed, giving the set  $\mathbf{n} = [n_i]_{i=0, \dots, 206}$ . This set was compared with the one obtained by trawling, consisting of  $M = 168$  colonies,  $\mathbf{n} = [n_i]_{i=0, \dots, 167}$ .

The distributions of the number of polyp leaves in both sets are compared in Figure 8, while descriptive statistics are reported in Table 1.

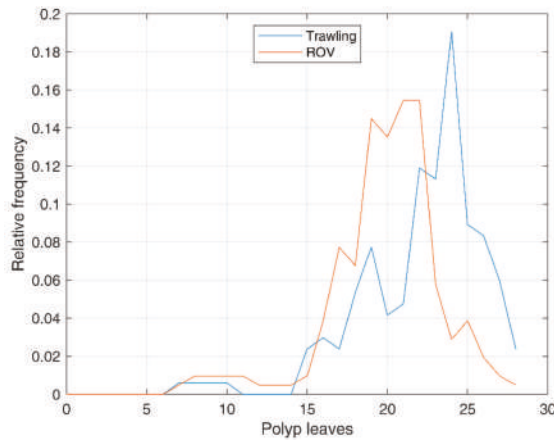


**Figure 8.** Comparison of the distribution of the number of polyp leaves in *Pennatula rubra*: in blue, samples obtained with trawling; in red, observations from Remotely Operated Vehicle (ROV) surveys.

**Table 1.** Statistics of the number of polyp leaves of *Pennatula rubra* for trawling- and Remotely Operated Vehicle (ROV)-based sampling.

Set	Mean $\mu$	Standard Deviation $\sigma$	Skewness $s$	Kurtosis $k$
Trawling	22.0	3.7	-1.3	5.6
ROV	19.9	3.5	-1.1	5.5

Bias-corrected standard deviation, standard deviation, bias-corrected skewness, and bias-corrected kurtosis have been defined, respectively, as follows:

$$\sigma = \sqrt{\sum_{i=0}^{M-1} \frac{(n_i - \mu)^2}{M - 1}} \tag{8}$$

$$\sigma' = \sqrt{\sum_{i=0}^{M-1} \frac{(n_i - \mu)^2}{M}} \tag{9}$$

$$s = \frac{\sqrt{M(M-1)}}{(M-2)} \sum_{i=0}^{M-1} \frac{\frac{1}{M}(n_i - \mu)^3}{\sigma'^3} \tag{10}$$

$$k = \frac{M-1}{(M-2)(M-3)} \left[ [M+1] \sum_{i=0}^{M-1} \frac{\frac{1}{M}[n_i - \mu]^4}{\sigma'^4} - 3[M-1] \right] + 3 \tag{11}$$

Standard deviation and kurtosis are similar for trawling and ROV data, while mean values and skewness differ by about 10% and 18%, respectively (Table 1). These differences can be due to many causes, such as: a slight difference in the two nearby subpopulations studied, since trawling hauls and ROV transects do not completely overlap; a minor catch efficiency of the trawl net on smaller colonies, that can be easily passed by the net without being collected; underestimation and errors in counting the number of polyp leaves from video analysis, considering that the first and the last polyp leaves can be very small, and their identification can be less easy from images than from samples.

By using the previously identified relationship between the number of polyp leaves and fresh weight of the colonies, an estimation of the total weight can be obtained from ROV images. In particular, for each colony  $i$ , the predicted fresh weight is  $\hat{w}_i = \hat{w}(n_i)$  according to the model (5).  $\hat{w}_i$  has been set to 0 for small colonies ( $n \leq 15$ ), where the model is not applicable.

Based on ROV images, the predicted mean weight of a colony is

$$\hat{w}_{mean} = \frac{1}{M} \sum_{i=0}^{M-1} \hat{w}_i = 1.86 \text{ g}$$

The total weight of a population present on an area  $S$  can then be estimated through

$$\hat{w}_{tot} = \hat{w}_{mean} \delta S$$

where  $\delta$  is the density of the colonies present on the surface  $S$ .

The mean weight of trawling samples, obtained by averaging the weights measured in the laboratory, is  $w_{mean} = 2.39$  g. Therefore, the relative error of weight prediction with ROV, for a given surface density and area, is  $-22\%$ . This result takes into account the previously mentioned error contributions, as well as the weight modeling error.

The weight estimation based on the number of polyp leaves through ROV imaging proved to be a feasible alternative to destructive sampling. Considering the low catch efficiency of trawl nets on sea pens [10,35,36], it cannot be excluded that small colonies have less possibility to be sampled, thus justifying the 22% difference observed between the mean weight of samples with the two methods.

#### 4. Conclusions

Zoological and ecological studies on VME indicator taxa are often based on abundance, biomass, and size structure of the population studied. This information is fundamental to assess the extent and the main features of soft-bottom coral communities, such as sea pen fields and coral gardens, in order to plan and apply proper protection initiatives. Except for abundance, considered as colonies density, whose estimation is known to be more accurate using visual methods than trawled sampling gears, the gathering of both size and biomass data has been historically carried out through destructive sampling. This study showed that the number of polyp leaves could be used for non-invasive studies of vulnerable species, such as *P. rubra*. In fact, this information can be retrieved from ad hoc ROV surveys, with a good level of accuracy and good reliability.

Despite the fact that the estimation of colonies' size and biomass using ROV imaging is a time-consuming process compared to the direct measurement of the samples, it can allow a non-destructive study and monitoring of vulnerable and protected species, for both studying and preserving the natural population. Data from different populations of *P. rubra* within the Mediterranean Sea would contribute to improve and refine the models, in order to make them applicable on a basin scale, as well as to highlight potential morphometric differences among the populations.

The use of polyp leaves to estimate other biometric parameters could be used worldwide for other species belonging to the suborder Subsessiliflorae, being characterized by the presence of polyp leaves. The identification of proper biometric relationships has been recently done for other sea pen species in eastern Canada [21] and is common for size–frequency distribution of other octocorals [37], as well

as for other marine invertebrates [38]. However, this approach cannot currently be applied to rare species, such as the endemic sea pen *Crassophyllum thessalonicae* Vafidis & Koukouras, 1991 [39] and the wip-like sea pen *Protoptilum carpenteri* Kölliker, 1872 [40].

Records of benthic species collected from accidental catches (e.g., fishery) could be used to obtain useful preliminary information to identify VMEs over very large areas. The analysis of large-enough sets of samples can also represent a basis to build further ad hoc models for the future study and monitoring of these species, particularly concerning soft-bottom coral populations. This sustainable approach supports the restrictions that should take place after the finding of dense populations of vulnerable species, such as the adoption of encounter protocols and the establishment of no-fishing areas on VMEs.

**Author Contributions:** Conceptualization, G.C.; Data curation, G.C., A.D.N. and A.M.L.L.; Formal analysis, A.D.N. and A.M.L.L.; Funding acquisition, G.C., G.A. and A.T.; Investigation, G.C. and F.M.; Methodology, G.C., A.D.N. and A.M.L.L.; Resources, G.C., A.D.N., A.M.L.L., G.A., A.T. and F.M.; Software, A.D.N. and A.M.L.L.; Validation, G.C., A.D.N., A.M.L.L. and F.M.; Writing—original draft, G.C.; Writing—review & editing, G.C., A.D.N., A.M.L.L. and F.M.

**Funding:** This research was funded by Ministero delle Politiche Agricole Alimentari e Forestali (MIPAAF). Part of this research was funded by National Geographic Society, grant number EC-176R-18. The APC was funded by Polytechnic University of Bari.

**Conflicts of Interest:** The authors declare no conflict of interest. The funders had no role in the design of the study; in the collection, analyses, or interpretation of data; in the writing of the manuscript, or in the decision to publish the results.

## References

- Chimienti, G.; Bo, M.; Mastrototaro, F. Know the distribution to assess the changes: Mediterranean cold-water coral bioconstructions. *Rendiconti Lincei Scienze Fisiche e Naturali* **2018**, *29*, 583–588. [[CrossRef](#)]
- Chimienti, G.; Bo, M.; Taviani, M.; Mastrototaro, F. Occurrence and Biogeography of Mediterranean Cold-Water Corals. In *Mediterranean Cold-Water Corals: Past, Present and Future*; Orejas, C., Jimenez, C., Eds.; Springer International Publishing: Berlin, Germany, 2019; Volume 9, pp. 1–64.
- Rossi, S.; Bramanti, L.; Gori, A.; Orejas, C. An overview of the animal forests of the world. In *Marine Animal Forests*; Rossi, S., Ed.; Springer International Publishing: Berlin, Germany, 2017; pp. 1–26.
- Mastrototaro, F.; Chimienti, G.; Acosta, J.; Blanco, J.; Garcia, S.; Rivera, J.; Aguilar, R. *Isidella elongata* (Cnidaria: Alcyonacea) facies in the western Mediterranean Sea: Visual surveys and descriptions of its ecological role. *Eur. Zool. J.* **2017**, *84*, 209–225. [[CrossRef](#)]
- Porporato, E.M.D.; De Domenico, F.; Mangano, M.C.; Spanò, N. *Macropodia longirostris* and *Latreillia elegans* (Decapoda, Brachyura) climbing on Mediterranean Pennatulidae (Anthozoa, Octocorallia): A preliminary note. *Crustaceana* **2011**, *84*, 1777–1780.
- Baillon, S.; Hamel, J.F.; Wareham, V.E.; Mercier, A. Deep cold-water corals as nurseries for fish larvae. *Front. Ecol. Environ.* **2012**, *10*, 351–356. [[CrossRef](#)]
- Kennington, E.; Murillo, F.J.; Lirette, C.; Sacau, M.; Koen-Alonso, M.; Kenny, A.; Ollerhead, N.; Wareham, V.; Beazley, L. Kernel Density Surface Modelling as a Means to Identify Significant Concentrations of Vulnerable Marine Ecosystem Indicators. *PLoS ONE* **2014**, *9*, e109365. [[CrossRef](#)] [[PubMed](#)]
- Ruiz-Pico, S.; Serrano, A.; Punzón, A.; Altuna, A.; Fernández-Zapico, O.; Velasco, F. Sea pen (Pennatulacea) aggregations on the northern Spanish shelf: Distribution and faunal assemblages. *Sci. Mar.* **2017**, *81*, 1–11. [[CrossRef](#)]
- FAO (Food and Agriculture Organization). *International Guidelines for the Management of Deep-Sea Fisheries in the High Seas*; FAO: Rome, Italy, 2009; pp. 1–21.
- Chimienti, G.; Angeletti, L.; Rizzo, L.; Tursi, A.; Mastrototaro, F. ROV vs. trawling approaches in the study of benthic communities: The case of *Pennatula rubra* (Cnidaria: Cennatulacea). *J. Mar. Biol. Assoc. UK* **2018**, *98*, 1859–1869. [[CrossRef](#)]
- Adamo, F.; Attivissimo, F.; Di Nisio, A.; Savino, M. An automated visual inspection system for the glass Industry. In Proceedings of the 16th IMEKO TC-4 International Symposium and 13th Workshop on ADC Modelling and Testing, Florence, Italy, 22–24 September 2008; pp. 442–447.

12. Adamo, F.; Attivissimo, F.; Di Nisio, A. Calibration of an inspection system for online quality control of satin glass. *IEEE Trans. Instrum. Meas.* **2010**, *59*, 1035–1046. [[CrossRef](#)]
13. Attivissimo, F.; Di Nisio, A.; Guarnieri Calò Carducci, C.; Spadavecchia, M. Fast Thermal Characterization of Thermoelectric Modules Using Infrared Camera. *IEEE Trans. Instrum. Meas.* **2017**, *66*, 305–314. [[CrossRef](#)]
14. Schindelin, J.; Rueden, C.T.; Hiner, M.C.; Eliceiri, K.W. The ImageJ ecosystem: An open platform for biomedical image analysis. *Mol. Reprod. Dev.* **2015**, *82*, 518–529. [[CrossRef](#)]
15. Sharma, N.; Aggarwal, L.M. Automated medical image segmentation techniques. *J. Med. Phys.* **2010**, *35*, 3–14. [[CrossRef](#)]
16. Adamo, F.; Attivissimo, F.; Di Nisio, A.; Spadavecchia, M. An automatic document processing system for medical data extraction. *Measurement* **2015**, *61*, 88–99. [[CrossRef](#)]
17. Andria, G.; Attivissimo, F.; Di Nisio, A.; Lanzolla, A.M.L.; Maiorana, A.; Mangiatini, M.; Spadavecchia, M. Dosimetric Characterization and Image Quality Assessment in Breast Tomosynthesis. *IEEE Trans. Instrum. Meas.* **2017**, *66*, 2535–2544. [[CrossRef](#)]
18. Gleason, A.C.R.; Reid, R.P.; Voss, K.J. Automated classification of underwater multispectral imagery for coral reef monitoring. In Proceedings of the OCEANS 2007, Vancouver, BC, Canada, 29 September–4 October 2007; pp. 1–8.
19. Phinn, S.R.; Roelfsema, C.M.; Mumby, P.J. Multi-scale, object-based image analysis for mapping geomorphic and ecological zones on coral reefs. *Int. J. Remote Sens.* **2012**, *33*, 3768–3797. [[CrossRef](#)]
20. Fogliini, F.; Grande, V.; Marchese, F.; Bracchi, V.A.; Prampolini, M.; Angeletti, L.; Castellan, G.; Chimienti, G.; Hansen, I.M.; Gudmundsen, M.; et al. Underwater Hyperspectral Imaging for seafloor and benthic habitat mapping in the southern Adriatic Sea (Italy). In Proceedings of the 2018 IEEE International Workshop on Metrology for the Sea, Learning to Measure Sea Health Parameters (MetroSea), Bari, Italy, 8–10 October 2018; pp. 201–205.
21. Murillo, F.J.; MacDonald, B.W.; Kenchington, E.; Campana, S.E.; Sainte-Marie, B.; Sacau, M. Morphometry and growth of sea pen species from dense habitats in the Gulf of St. Lawrence, eastern Canada. *Mar. Biol. Res.* **2018**, *14*, 366–382. [[CrossRef](#)]
22. Ludvigsen, M.; Johnsen, G.; Sørensen, A.J.; Lågstad, P.A.; Ødegaard, Ø. Scientific operations combining ROV and AUV in the Trondheim Fjord. *Mar. Technol. Soc. J.* **2014**, *48*, 59–71. [[CrossRef](#)]
23. Mastrototaro, F.; Aguilar, R.; Chimienti, G.; Gravili, C.; Boero, F. The rediscovery of *Rosalinda incrustans* (Cnidaria: Hydrozoa) in the Mediterranean Sea. *Ital. J. Zool.* **2016**, *83*, 244–247. [[CrossRef](#)]
24. Petritoli, E.; Leccese, F.; Cagnetti, M. A High Accuracy Buoyancy System Control for an Underwater Glider. In Proceedings of the 2018 IEEE International Workshop on Metrology for the Sea, Learning to Measure Sea Health Parameters (MetroSea), Bari, Italy, 8–10 October 2018; pp. 257–261.
25. Adamo, F.; Andria, G.; Di Nisio, A.; Calò Carducci, C.G.; Lay-Ekuakille, A.; Mattencini, G.; Spadavecchia, M. Designing and prototyping a sensors head for test and certification of UAV components. *Int. J. Smart Sens. Intell. Syst.* **2017**, *10*, 646–672. [[CrossRef](#)]
26. Barwise, A.; Cowie, M. Advancement in Geotechnical Site Investigation Practice Using ROV Technology. In Proceedings of the Offshore Technology Conference, Houston, TX, USA, 6–9 May 2013; pp. 1–8.
27. McLean, D.L.; Macreadie, P.; White, D.J.; Thomson, P.G.; Fowler, A.; Gates, A.R.; Benfield, M.; Horton, T.; Skropeta, D.; Bond, T.; et al. Understanding the Global Scientific Value of Industry ROV Data, to Quantify Marine Ecology and Guide Offshore Decommissioning Strategies. In Proceedings of the Offshore Technology Conference Asia, Kuala Lumpur, Malaysia, 20–23 March 2018; pp. 1–10.
28. Adamo, F.; Andria, G.; Bottiglieri, O.; Cotecchia, F.; Di Nisio, A.; Miccoli, D.; Sollecito, F.; Spadavecchia, M.; Todaro, F.; Trotta, A.; et al. GeoLab, a measurement system for the geotechnical characterization of polluted submarine sediments. *Measurement* **2018**, *127*, 335–347. [[CrossRef](#)]
29. Chimienti, G.; Tursi, A.; Mastrototaro, F. Biometric relationships in the red sea pen *Pennatula rubra* (Cnidaria: Pennatulacea). In Proceedings of the 2018 IEEE International Workshop on Metrology for the Sea, Learning to Measure Sea Health Parameters (MetroSea), Bari, Italy, 8–10 October 2018; pp. 212–216.
30. Rooper, C.N.; Wilborn, P.; Goddard, P.; Williams, K.; Towler, R.; Hoff, G.R. Validation of deep-sea coral and sponge distribution models in the Aleutian Islands, Alaska. *ICES J. Mar. Sci.* **2017**, *75*, 199–209. [[CrossRef](#)]
31. Chimienti, G.; Angeletti, L.; Mastrototaro, F. Withdrawal behaviour of the red sea pen *Pennatula rubra* (Cnidaria: Pennatulacea). *Eur. Zool. J.* **2018**, *85*, 64–70. [[CrossRef](#)]

32. Otero, M.M.; Numa, C.; Bo, M.; Orejas, C.; Garrabou, J.; Cerrano, C.; Kružić, P.; Antoniadou, C.; Aguilar, R.; Kipson, S.; et al. *Overview of the Conservation Status of Mediterranean Anthozoans*; IUCN: Málaga, Spain, 2017; pp. 1–73.
33. Bertrand, J.A.; Gil De Sola, L.; Papaconstantinou, C.; Relini, G.; Souplet, A. The general specifications of the MEDITS surveys. *Sci. Mar.* **2002**, *66*, 9–17. [[CrossRef](#)]
34. Fiorentini, L.; Dremière, P.Y.; Leonori, I.; Sala, A.; Palombo, V. Efficiency of the bottom trawl used for the Mediterranean International Trawl Survey (MEDITS). *Aquat. Living Resour.* **1999**, *12*, 187–205. [[CrossRef](#)]
35. Kenchington, E.; Murillo, F.J.; Cogswell, A.; Lirette, C. *Development of Encounter Protocols and Assessment of Significant Adverse Impact by Bottom Trawling for Sponge Grounds and Sea Pen Fields in the NAFO Regulatory Area*; NAFO Scientific Council Report 11/75 Serial No N6005; Agris: Dartmouth, NS, Canada, 2011; Volume 53, pp. 1–51.
36. Troffe, P.M.; Levings, C.D.; Piercey, G.E.; Keong, V. Fishing gear effects and ecology of the sea whip (*Halipterus willemoesi* (Cnidaria: Octocorallia: Pennatulacea)) in British Columbia, Canada: Preliminary observations. *Aquat. Conserv.* **2005**, *15*, 523–533. [[CrossRef](#)]
37. Ambroso, S.; Gori, A.; Dominguez-Carrió, C.; Gili, J.M.; Berganzo, E.; Teixidó, N.; Greenacre, M.; Rossi, S. Spatial distribution patterns of the soft corals *Alcyonium acaule* and *Alcyonium palmatum* in coastal bottoms (Cap de Creus, northwestern Mediterranean Sea). *Mar. Biol.* **2014**, *160*, 3059–3070. [[CrossRef](#)]
38. Mastrototaro, F.; Chimienti, G.; Matarrese, A.; Gambi, M.C.; Giangrande, A. Growth and population dynamics of the non-indigenous species *Branchiomma luctuosum* Grube (Annelida, Sabellidae) in the Ionian Sea (Mediterranean Sea). *Mar. Ecol.* **2015**, *36*, 517–529. [[CrossRef](#)]
39. Fryganiotis, K.; Antoniadou, C.; Chintiroglou, C.; Vafidis, D. Redescription of the Mediterranean endemic sea-pen *Crassophyllum thessalonicae* (Octocorallia: Pteroeidae). *Mar. Biodivers. Rec.* **2011**, *4*, 1–3. [[CrossRef](#)]
40. Mastrototaro, F.; Chimienti, G.; Capezzuto, F.; Carlucci, R.; Williams, G. First record of *Protoptilum carpenteri* (Cnidaria: Octocorallia: Pennatulacea) in the Mediterranean Sea. *Ital. J. Zool.* **2015**, *82*, 61–68. [[CrossRef](#)]



© 2019 by the authors. Licensee MDPI, Basel, Switzerland. This article is an open access article distributed under the terms and conditions of the Creative Commons Attribution (CC BY) license (<http://creativecommons.org/licenses/by/4.0/>).

Article

# Application of Hyperspectral Imaging to Underwater Habitat Mapping, Southern Adriatic Sea

Federica Fogliani <sup>1</sup>, Valentina Grande <sup>1,\*</sup>, Fabio Marchese <sup>2</sup>, Valentina A. Bracchi <sup>2</sup>, Mariacristina Prampolini <sup>1</sup>, Lorenzo Angeletti <sup>1</sup>, Giorgio Castellan <sup>1,3</sup>, Giovanni Chimienti <sup>4</sup>, Ingrid M. Hansen <sup>5</sup>, Magne Gudmundsen <sup>5</sup>, Agostino N. Meroni <sup>2</sup>, Alessandra Mercorella <sup>1</sup>, Agostina Vertino <sup>2,6</sup>, Fabio Badalamenti <sup>7</sup>, Cesare Corselli <sup>2</sup>, Ivar Erdal <sup>5</sup>, Eleonora Martorelli <sup>8</sup>, Alessandra Savini <sup>2</sup> and Marco Taviani <sup>1,9,10</sup>

- <sup>1</sup> National Research Council, Institute of Marine Sciences, Via Gobetti 101, 40129 Bologna, Italy; federica.fogliani@bo.ismar.cnr.it (F.F.); mariacristina.prampolini@bo.ismar.cnr.it (M.P.); lorenzo.angeletti@bo.ismar.cnr.it (L.A.); giorgio.castellan@bo.ismar.cnr.it (G.C.); alessandra.mercorella@bo.ismar.cnr.it (A.M.); marco.taviani@bo.ismar.cnr.it (M.T.)
- <sup>2</sup> Department of Earth and Environmental Sciences and CoNISMa LRU, University of Milano - Bicocca, Piazza della Scienza 1, 20126 Milano, Italy; fabio.marchese1@unimib.it (F.M.); valentina.bracchi@unimib.it (V.A.B.); a.meroni9@campus.unimib.it (A.N.M.); agostina.vertino@unimib.it (A.V.); cesare.corselli@unimib.it (C.C.); alessandra.savini@unimib.it (A.S.)
- <sup>3</sup> Department for the Cultural Heritage, University of Bologna, Via degli Ariani 1, 48121 Ravenna, Italy
- <sup>4</sup> Department of Biology and CoNISMa LRU, University of Bari, Via Orabona 4, 70124 Bari, Italy; giovanni.chimienti@uniba.it
- <sup>5</sup> Ecotone AS, Pirsenteret Havnegata 9, inngang 1 – 3 etg, 7010 Trondheim, Norway; ingrid@ecotone.com (I.M.H.); magne@ecotone.com (M.G.); ivar@ecotone.com (I.E.)
- <sup>6</sup> Ghent University, Campus Ufo, Rectorate, Sint-Pietersnieuwstraat 25, B-9000 Ghent, Belgium
- <sup>7</sup> National Research Council, Institute for the Study of Anthropic Impacts and Sustainability in Marine Environments Via Giovanni da Verrazzano 17, 91014 Castellammare del Golfo, Trapani, Italy; fabio.badalamenti@cnr.it
- <sup>8</sup> National Research Council, Institute of Environmental Geology and Geoengineering, Via Salaria km 29,300, 00015 Monterotondo, Rome, Italy; eleonora.martorelli@uniroma1.it
- <sup>9</sup> Biology Department, Woods Hole Oceanographic Institution, 266 Woods Hole Road, Woods Hole, MA 02543, USA
- <sup>10</sup> Stazione Zoologica Anton Dohrn, Villa Comunale, 80121 Naples, Italy
- \* Correspondence: valentina.grande@bo.ismar.cnr.it; Tel.: +39-051-6398875

Received: 31 March 2019; Accepted: 12 May 2019; Published: 16 May 2019

**Abstract:** Hyperspectral imagers enable the collection of high-resolution spectral images exploitable for the supervised classification of habitats and objects of interest (OOI). Although this is a well-established technology for the study of subaerial environments, Ecotone AS has developed an underwater hyperspectral imager (UHI) system to explore the properties of the seafloor. The aim of the project is to evaluate the potential of this instrument for mapping and monitoring benthic habitats in shallow and deep-water environments. For the first time, we tested this system at two sites in the Southern Adriatic Sea (Mediterranean Sea): the cold-water coral (CWC) habitat in the Bari Canyon and the Coralligenous habitat off Brindisi. We created a spectral library for each site, considering the different substrates and the main OOI reaching, where possible, the lower taxonomic rank. We applied the spectral angle mapper (SAM) supervised classification to map the areal extent of the Coralligenous and to recognize the major CWC habitat-formers. Despite some technical problems, the first results demonstrate the suitability of the UHI camera for habitat mapping and seabed monitoring, through the achievement of quantifiable and repeatable classifications.

**Keywords:** hyperspectral camera; spectral library; habitat mapping; coralligenous; cold-water coral; Adriatic Sea

## 1. Introduction

Traditionally, underwater habitat mapping has been carried out coupling acoustic remote sensing techniques with red/green/blue (RGB) images, videos and bottom sampling [1,2]. The analysis of video and images is performed manually by expert interpretation, or automatically when a photomosaic is available [3]. Recently, the European programs such as the EU Marine Strategy Framework Directive (MSFD: 2008/56/EC), require the monitoring of benthic habitat extent and distribution (Criteria 1.4 and 1.5 of the Descriptor 1 “Biological Diversity”). The MSFD scope is to assess the good environmental status (GES) of European water [4] with the lowest possible impact on the seafloor. This effort is translated into quantifiable operational indicators that should be measurable at different scale and repeatable in time [4]. To fulfill these requirements, there is a need for innovative approaches and tools to obtain detailed, reliable, quantifiable and repeatable maps of relevant habitats in different underwater environments [2].

During the last decade, the implementation of hyperspectral devices has become a viable alternative to regular photography. In contrast to ordinary cameras that acquire three colour bands (RGB), hyperspectral cameras record the full spectrum of reflected light, in each pixel of the acquired image. Therefore, the spectral resolution and amount of information obtainable from an image transect is vastly increased compared to traditional photography [5]. As a result, UHI can detect the subtle and otherwise unnoticeable spectral properties of a given OOI and record object-specific optical fingerprints. Optical fingerprinting increases classification accuracy for both qualitative and quantitative mapping [5].

This technology has previously been applied to airborne remote sensing, both in terrestrial and marine environments, through passive sensors requiring sunlight. However, sunlight is highly attenuated in marine waters [6,7]. As a consequence, this technique is suitable only in coastal areas and relatively shallow water (up to 50 m depth: [8–10]). Hence, works on hyperspectral imaging from satellite or airplanes are focussed on oceanographic and biological studies [11,12], mapping of ocean colour [12,13] and shallow benthic habitats [8,10] such as coral reefs [14–17], seagrasses [18–20] and kelp forests [9].

Recently, different instrument carriers for the underwater hyperspectral imager (UHI) have been used in underwater field applications, such as the customized scanning rig [21,22], remotely operated vehicle (ROV) [6,7,23–27] or autonomous underwater vehicle (AUV) [28]. The UHI has been tested and utilized for different purposes from shallow (< 6 m) [22] to abyssal depths (ca. 4200 m depth) [6,7]. Among the many applications, UHI was related to the identification of manganese nodules [6], infrastructure inspection, seafloor impact of offshore drilling [29] and marine archaeology [25,27,30]. However, the most reported UHI application is within the field of benthic habitat mapping, modelling and monitoring. Underwater hyperspectral imaging with ROV has been used to study coastal kelp forests [25], vertical rock wall habitat and soft sediments [24], red calcareous algae and associated fauna [25,26], deep-sea megafauna [7] and CWC communities [23,25]. Laboratory experiments to measure changes in the health status of CWCs exposed to hydrocarbons emissions is another application of UHI [31].

As a first application to the Mediterranean basin, we tested the UHI in the Adriatic Sea [32]. The semi-enclosed Adriatic Sea hosts a variety of benthic habitats, including the shallow oyster reefs and sponge communities in the Venice Lagoon [33], coralligenous formations on the shelf (e.g., [34] with references therein), down to the CWC habitat in deep water (> 200 m) in the south (e.g., [35–40]). At present, the Adriatic Sea is under siege by a number of stressors, such as high demographic pressure on its coastal areas, pollution, marine littering and dumping, fishing practices, ship traffic, harbour activities and industrial operations [41]. Our study targets the distribution and extent of two biogenic habitats (CWC and Coralligenous), in different geomorphological and depth contexts, considered to be of key importance in monitoring plans. In this perspective, the UHI may prove useful in habitat mapping to meet the requirements of European programs (e.g., EU MSFD).

## 2. Materials and Methods

### 2.1. Study Area

The two selected sites are located in the Southern Adriatic Sea (Figure 1): the Bari Canyon (CWC habitat) and the continental shelf off-shore Brindisi (Coralligenous habitat).

The Bari Canyon site is located ca. 40 km away from the city of Bari, on the continental margin, within a well-known Cold-Water Coral ecosystem, extending between –200 and –700 m on the southern flank of the canyon [35,36,38,42,43]. The CWC habitat is here characterised by complex megabenthic communities, mainly represented by the colonial scleractinian *Madrepora oculata*, subordinately *Desmophyllum pertusum* (*Lophelia pertusa* [44]) and the solitary *Desmophyllum dianthus*, and by large fan-shaped sponges (i.e. *Pachastrella monilifera* and *Poecillastra compressa*) [35–37,40].

The Brindisi site is placed on a flat continental shelf, about 10 km far from the coast at an average depth of 30 m. Coralligenous outcrops, mosaicking coarse biogenic sediments [34–46], dominate the seafloor. The coralligenous is a very complex habitat where crustose coralline algae (CCA) and red algae belonging to the order of Peyssonelliales are often the main bioconstructors in shallower waters, generating a new solid substrate and constituting a three-dimensional biogenic build-up [47–52]. It represents a key habitat of the Mediterranean continental shelf because of its structural and functional importance, as well as for its considerable aesthetic value [53]. In the study area, discrete coralligenous build-ups [46] characterize the seafloor, with a thickness up to 70 cm. CCA, usually growing in dim light conditions, and other algae such as Peyssonelliales primarily form these solid substrates; bryozoans and serpulids contribute to the bioconstruction [54,55]. Moreover, these hard substrates host different fauna and flora, often overgrowing the calcified red algae [51].

### 2.2. Underwater Hyperspectral Imager (UHI)

The underwater hyperspectral imager (UHI), developed and patented by Ecotone AS, consists of a waterproof housing containing camera system, computer and data storage. It is operated with a light source for proper illumination, and represents a new system for the identification, mapping and monitoring of OOI at the seabed [5,25].

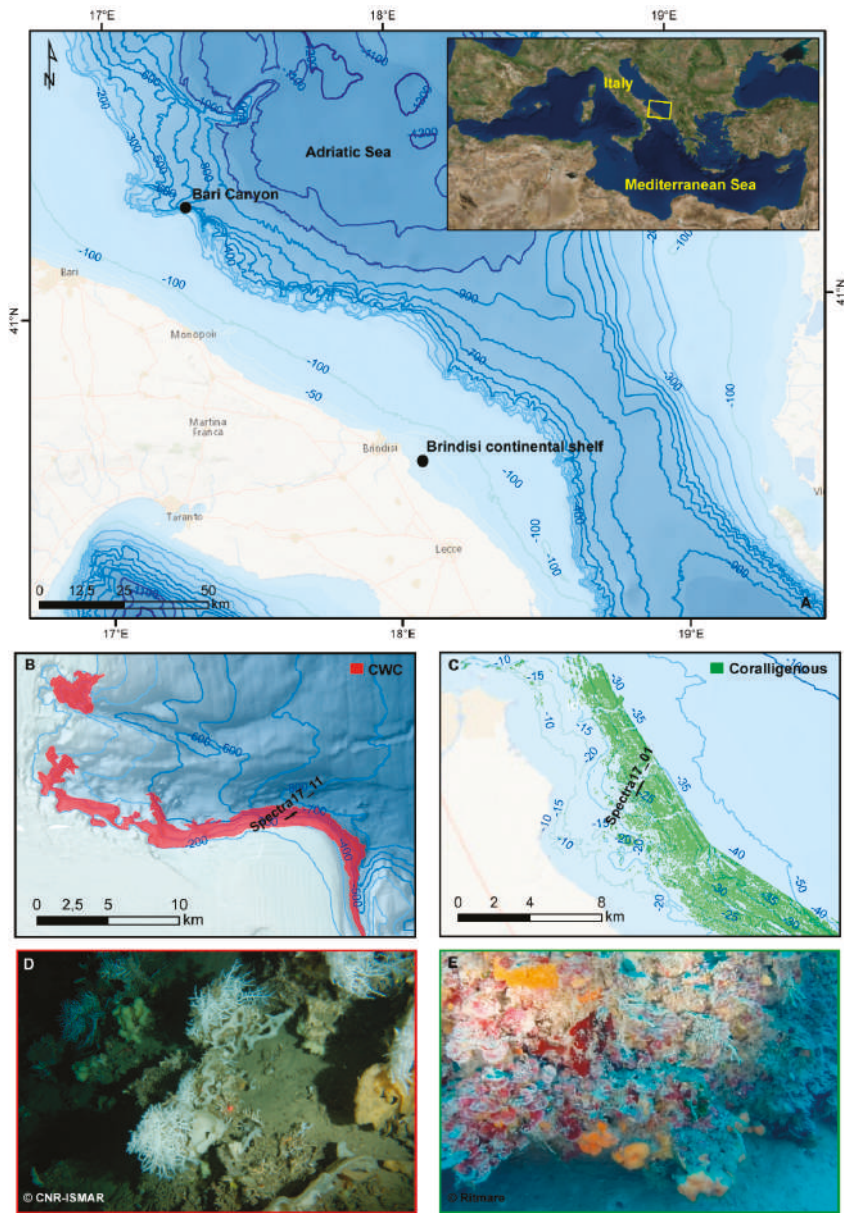


**Figure 1.** (A) Location of the two sites, inset shows the position in the Mediterranean Sea; (B) the extension of the Bari Canyon CWC province (from [56]) and (C) the extension of the coralligenous in the Brindisi area (black lines indicate the ROV surveys). Habitat maps produced by the BIOMAP project and further updated within the CoCoNet project. (D) Example of CWC habitat complexity showing colonies of *M. oculata* and large fan-shaped sponges (from [38]); (E) example of coralligenous characterized by CCA and Peyssonelliales, serpulids and orange encrusting sponges overprinting the calcified red algae.

The UHI is a push broom camera, which records one line at time. It is equipped with a spectrograph that receives light through a thin entrance slit [57]. Light entering the instrument is diffracted into separate wavelengths and projected onto the camera sensor as a contiguous spectrum. A continuous image is built up line by line and can be presented on a monitor for visualisation [26].

The UHI needs to be mounted on a moving platform (e.g., ROV) that operates at a fairly constant speed and altitude from the seafloor. Mobile platforms equipped with dynamic positioning systems permit larger areal coverage, and the possibility of re-visiting the surveyed sites based on their geolocation data [58]. External lamps provide seafloor illumination. Due to the rapid attenuation of light in the marine environment, UHI is normally confined to scanning altitudes <5 m above the OOI, depending on water quality and turbidity.

Image lines are captured perpendicular to the direction of movement. The result is a hyperspectral image, featuring detected intensities for all the wavelengths used [57]. The spatial resolution provided by hyperspectral cameras varies with altitude, exposure time of the camera and speed vessel.

### 2.3. Data Acquisition

In February 2017, we carried out the SPECTRA17 cruise on board of the R/V Minerva Uno, aimed at testing the ability of the UHI to acquire seafloor hyperspectral images in the Southern Adriatic Sea.

An Ecotone UHI (Model 4) was mounted vertically beneath the ROV Super Mohawk II 34 Observation Class, facing directly towards the seafloor, together with two LED lamps (3200 lumens per lamp) oriented at 90°, a 2D high resolution RGB camera with two lamps oriented at 60° and a system to correct UHI camera motion for pitch, roll and yaw. Acquisition and pre-processing of data were managed through the C++ based UHI customized software Immersion installed on the topside control unit.

The ROV maintained constant speed (about 1 knot) and heading in each dive (45° for CWC and 25° for coralligenous, respectively), at a constant altitude of 1–1.5 m. The track length was about 2.5 km for the CWC site and 785 m for the coralligenous site.

ROV navigation and position was provided by Low-Accuracy TrackLink USBL Positioning System (accuracy of <2% of the water depth), positioning data were recorded at 1 sec. The positioning system was operated using the software PDS2000. In addition to UHI, a black and white camera for ROV navigation and a high-resolution camera provided footage for manual identification of OOI.

We reoccupied previous ROV tracks, making use of high-resolution videos and photos already available for comparing the UHI results and classification.

### 2.4. High Resolution Camera Image Data Processing

The RGB images for coralligenous and CWC sites, collected by the high-resolution camera, were processed using ADELIE Software by IFREMER and used to identify and classify the OOI. ADELIE is a software able to synchronise video and navigation and then automatically capture georeferenced still images (or image sequences) for a chosen time interval (e.g., every 10 s). Through a specific module of ADELIE based on ArcGIS Desktop, it is possible to filter and smooth vehicle navigation, to have direct access to pictures and to localize video in real time. Following this procedure, we mapped all track lines producing benthic habitat maps and estimated the extent of habitat at ROV scale.

### 2.5. UHI Data Processing

Processing of hyperspectral images consisted of three main steps: (1) Radiometric processing correcting for sensor influence; (2) Georeferencing to assign geospatial information and perform image geocorrection; (3) Conversion of radiance to reflectance by correction of external influences from illumination source. Using Immersion, we performed the georeferencing and radiometric correction of the acquired images to produce non-distorted and georeferenced hyperspectral images. The spectral resolution is up to 2.2 nm, while the spatial resolution is 1 cm for CWCs and 0.5 cm for coralligenous. The resulting UHI coverage is about 1–1.2 m width, depending on height above seafloor.

The pre-processed UHI images used in this work are available as Research Object (for further details see Supplementary Materials).

### 2.5.1. Radiometric Processing

The UHI was calibrated in the laboratory before the oceanographic mission. A standard lamp with known spectral properties was used to find the ratio between observed the digital counts of intensity for each wave band on the sensor, to spectral radiance ( $\text{W m}^{-2} \text{sr}^{-1} \text{nm}^{-1}$ ). These measurements can be applied on raw recordings from the field to correct for sensor-specific noise and dark current, as well as data acquisition parameters such as exposure time and binning. Radiance conversion was automatically performed as part of the georeferencing algorithm in Immersion.

### 2.5.2. Georeferencing

Geographic position and spatial correction of the hyperspectral images were provided by the georeferencing procedure through Immersion software by using: (1) USBL data for the ROV position and (2) altitude data from the Ecotone IMU (Inertial Measurement Unit). As the navigation produced by USBL track link contains frequent spikes and some metrical gaps, we statistically filtered navigation and altitude data through 20- and 5-point-wide windows, respectively, using an adjacent averaging smoothing algorithm to improve resolution [59]. In addition to navigation, motion and altitude data the following parameters for Immersion were set: (1) course-made-good option for ROV heading calculation; (2) a spectral binning of 8 resulting in 28 bands with 15 nm resolution; (3) a spatial binning of 1 and (4) a cell resolution of 1 cm for CWCs and 0.5 cm for coralligenous.

### 2.5.3. Reflectance Processing

Following the procedure in [1], radiance data was converted into reflectance correcting for the external influence on the spectral characteristics from LED lamps or their combination with sunlight, at the deep and shallow site, respectively. These spectral characteristics are not definable, so we approximated the illumination influence by using a reference spectrum calculated for the entire analysed segment of both sites in R software [60]. Then, we divided each image pixel by its respective reference spectrum.

## 2.6. UHI Spectral Supervised Classification

We selected a segment from the CWC track line of about 10 m and a segment from the coralligenous track line of about 7.5 m for the spectral supervised classification and further analysis. Classification was performed through the software ENVI 5.5, using the spectral angle mapper (SAM) method. The accuracy was determined generating a confusion matrix for each site.

### 2.6.1. Spectral Angle Mapper (SAM)

The spectral angle mapper (SAM) is a supervised classification technique that measures the similarity of image spectra to reference spectra. The reference spectra can be measured in field or laboratory, they can be taken directly from the image as region of interest (ROI) or imported from already known spectral libraries. SAM measures similarity by calculating the angle between the two spectra, treating them as vectors in  $n$ -dimensional space, with  $n$  being the number of bands [61]. The angle is the arccosine of the dot product of the two spectra. Smaller values for the angle indicate higher similarity between pixel and reference spectra. As the angle between two vectors is independent of the vector length, this method is unaffected by gain factors, such as solar illumination [62]. The SAM only compares the angle between the spectral directions of the reference and test pixels considered, there is no specific requirement for a large amount of training samples [63].

We trained the model selecting ROIs that include spectral signatures representing substrates, megaflore and megafauna ( $> 2 \text{ cm}$ ) present in the surveyed areas. The selected ROIs reflect the highest

spectral diversity due to different pigmentation of the OOI and make up the benthic classes that will constitute the final classification.

In particular for the CWC site, we used 10 ROIs to train the SAM classification representing 4 benthic classes: (1) colonial cnidarian, (2) sponge, (3) mud, (4) bedrock (Table 1). For colonial cnidarian, bedrock and sponge we selected multiple ROIs due to the differences of the UHI RGB colours along the segment. For the coralligenous site, we created 13 ROIs identifying 5 benthic classes: (1) CCA and Peyssonelliales (P) forming the build-ups (CCA+P); (2) green algae on build-ups (in particular *Codium bursa* and *Flabellia petiolata*) and on sediment (*Caulerpa prolifera*); (3) Seagrass (*Posidonia oceanica*); (4) organisms associated with the presence of build-ups; and (5) sand (Table 2). For the CCA+P and the green algae (Green algae 1 and 2) classes, we selected more than one ROI due to the illumination unevenness caused by the slight altitude variation along the track.

After running the SAM with a maximum angle of 0.1 radian, we applied the ENVI 'Rule classifier' post classification tool to adjust the threshold angles for each class and improve the classification results. We choose the appropriate thresholds classifying by minimum values and visualizing the histogram that shows the frequency of pixel with different angles. Finally, we used the ENVI 'Majority/Minority analysis' tool with a kernel size of 3 × 3 to clean and smooth the SAM classification.

**Table 1.** Selected ROIs for the benthic classes of the CWC site and relative threshold values used in the 'Rule classifier' tool.

Benthic Class	Colonial Cnidarian			Sponge				Mud	Bedrock		
	ROI	1	2	3	1	2	3	4	1	1	2
Taxonomy	<i>M. oculata</i> / <i>D. pertusum</i>			<i>Hexactinellida</i> sp.	<i>Demospongiae</i> sp. 1	<i>Demospongiae</i> sp. 2	<i>Demospongiae</i> sp. 3				
Threshold	0.035	0.025	0.08	0.08	0.15	0.045	0.035	0.08	0.08	0.08	

**Table 2.** Selected ROIs for the benthic classes of the coralligenous site and relative threshold values used in the 'Rule classifier' tool.

Benthic Class	CCA+P			Green Algae			Seagrass	Associated Organism				Sand		
	ROI	1	2	3	1	2	3	1	Sponge 1	Sponge 2	Serpulids	Red Starfish	Red Ascidia	1
Taxonomy				<i>C. bursa</i> / <i>F. petiolata</i>	<i>C. prolifera</i>	<i>P. oceanica</i>	<i>Axinella</i> sp. 1	<i>Axinella</i> sp. 2				<i>E. sepositus</i>	<i>H. papillosa</i>	
Threshold	0.2	0.02	0.07	0.08	0.08	0.065	0.045	0.08	0.07	0.03	0.18	0.06	0.2	

## 2.6.2. SAM Classification Accuracy

We generated a confusion matrix for both test sites using ENVI and ArcGIS desktop to determine the accuracy of the classification results. Firstly, we produced eight random sampling points for each benthic class using the 'Generate random sample' ENVI tool with the equalized random technique to divide the population into homogeneous subgroups, while ensuring that each class sample size was the same (1 pixel). Then, we compared within ArcGIS Desktop the random sampling points predicted classes with the UHI image (ground truthing), to assign the real class for each point as defined by the expert interpretation. We generated the confusion matrix for each classification using the predicted classes and the real class values specifying the overall, producer's and user's accuracies. The overall accuracy is calculated by summing the number of correctly classified values and dividing by the total number of values. The user's accuracy (UA) is the number of correctly identified pixels in a class, divided by the total number of pixels of the class in the classified image; it shows false positives, where pixels are incorrectly classified as a known class when they should have been classified as something else. Producer's accuracy (PA) is the number of correctly identified pixels divided by the total number of pixels in the reference image; it gives a false negative, where pixels of a known class are classified as something other than that particular class.

### 3. Results

#### 3.1. Spectral Library for CWC Site

The mean spectra of the 10 ROIs selected for the CWC site are shown in Figure 2. Mud and bedrock have an almost constant level of reflectance along all wavelengths. The bedrock shows a deflection point at 473 nm, with a minimum at 500 nm (Figure 2A,B). The sponge 1 has an inflection point at 500 nm and an increasing trend between 555 and 680 nm (from green to red) (Figure 2C). Sponge 2 and 3 display similar patterns with a dissimilar level of reflectance due to different illumination, an inflection point at 530 nm and highest values in the orange/red part of the spectrum between 630 nm and 670 nm. Sponge 4 has a slightly different shape and a smoothed slope, possibly caused by a minor colour difference. Despite all sponges seem to pertain to the same morphotype (belonging to the white/orange large fan-shaped *P. compressa* and/or *P. monilifera*), it is not possible to attribute the accurate species to each ROI and to each spectrum (Figure 2D). The colonial cnidarian 2 and 3 have a spectral signature with a similar pattern, constant along the entire wavelength range, with a difference in the level of reflectance, while colonial cnidarian 1 shows a slight peak in the blue part of the spectrum (about 470 nm) (Figure 2E). According to previous studies (e.g., [35,36,38,43,56]), we can assume that the most probable species belong to *M. oculata*, while the *D. pertusum* appears to be rarer in this site.

For benthic classes with multiple ROIs (colonial cnidarian, sponge and bedrock), we analyzed the spectral differences and considered the mean for spectra with the same pattern but a different reflectance intensity (Figure 2F). The three ROIs of the colonial cnidarians are recognized as a unique class, because the peak in the blue part of the spectrum for colonial cnidarian 1 is considered an artefact.

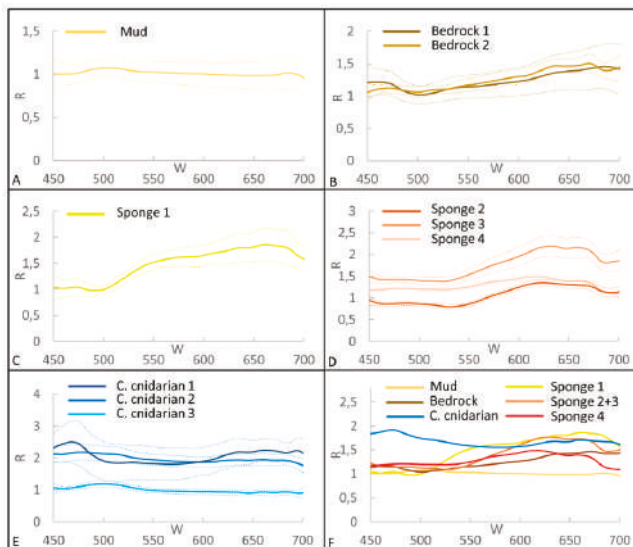


**Figure 2.** Mean spectra of the ROIs for the CWC site. R is the reflectance and W the wavelength. In A, B, C, D and E, dashed lines represent the standard deviation. F shows the synthesis of all spectra.

#### 3.2. Spectral Library for the Coralligenous Site

The mean spectra of the 13 ROIs selected for the coralligenous site are shown in Figure 3. The CCA+P1, CCA+P2, CCA+P3 have the inflection point at 600 nm with a maximum between 630 and 670 nm in the red part of the spectrum. The wide range of standard deviation probably reflects the high biodiversity of this category. We can assume that the three spectra, with a similar pattern and a different level of reflectance intensity, belong to the same benthic class CCA+P.

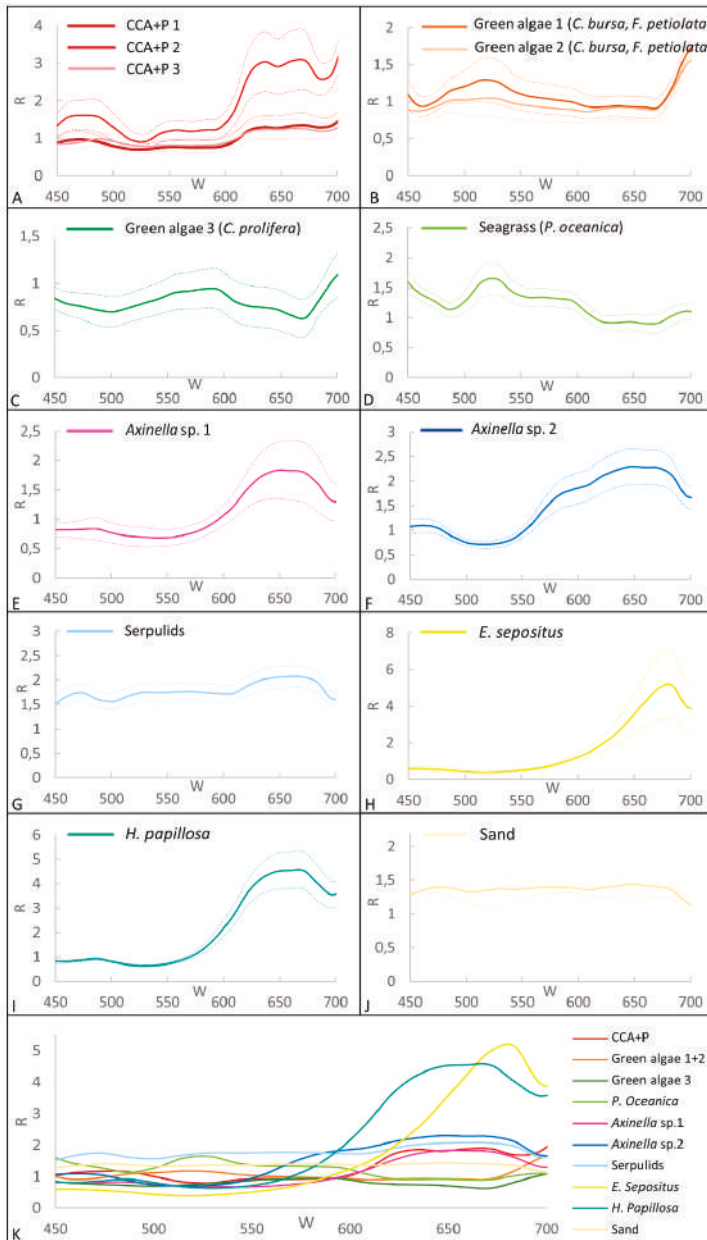


**Figure 3.** Mean spectra based on the ROIs relative to the coralligenous site. The dashed line in the graphs represents the standard deviation. K shows the synthesis of all spectra.

The green algae on build-ups (green algae 1+2), mainly represented by *C. bursa* and *F. petiolata*, have a maximum at about 515 nm (green part of the spectrum), while the green algae *C. prolifera* (Green algae 3) and the seagrass *P. oceanica* show a slight difference with a maximum of reflectance at 595 and 528 nm, respectively. The ascidian *Halocynthia papillosa* and the starfish *Echinaster sepositus* show a peak

at 650 and 680 nm in the red part of the spectrum. The serpulids show an almost constant spectrum with a small inflection at 610 nm. The two species belonging to the genus *Axinella* have similar spectra with a maximum between 630 and 670 nm (red part of the spectrum). The sand has a constant value of reflectance along all wavelengths.

### 3.3. Supervised Classification Results for CWC Site

Based upon the previous considerations about the spectra, we can define six benthic classes for the final classification: (1) colonial cnidarian, (2) sponge 1, (3) sponge 2+3, (4) sponge 4, (5) mud and (6) bedrock (Figure 4). The mud class results were the most dominant (40%) followed by the bedrock (23.6%). The colonial cnidarian class is scattered along the track with a total coverage of 0.4%, the sponge classes (sponge 1, sponge 2+3, sponge 4) are patchy with a total coverage of 0.3%. The illumination problems, due to low lamp potential, ROV orientation and dipping of the substrate (the canyon flank in this site is up to 25°), cause a homogenous dark shading on the right (deeper) section of the image. This results in a high percentage of unclassified pixels (26.5%), also including colonial cnidarians and sponges still visible on the RGB image. However, these technical issues do not prevent the clear discrimination of the benthic classes and the estimation of percentage cover.

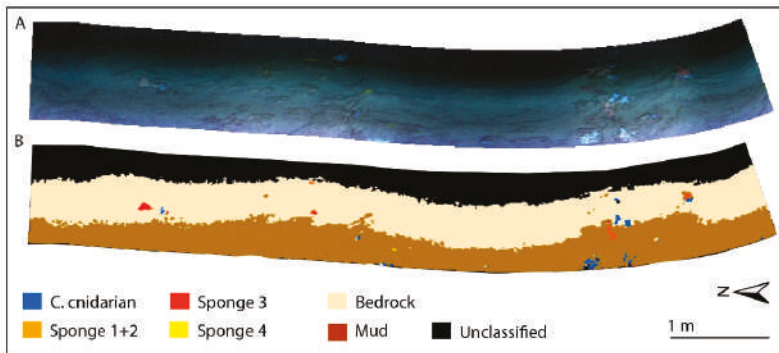


Figure 4. RGB UHI image of the CWC site in A and its SAM classification in B.

### 3.4. Supervised Classification Results for Coralligenous Site

For the coralligenous we defined 10 benthic classes for the final classification (Figure 5), according to the analysis of spectral signatures: (1) CCA+P, (2) green algae 1+2, (3) *C. prolifera*, (4) *P. oceanica*, (5) *Axinella* sp. 1, (6) *Axinella* sp. 2, (7) serpulids, (8) *E. sepositus*, (9) *H. papillosa*, (10) Sand. The sand class is the most dominant in the area with a coverage of 60%. The build-ups are generally well discriminated along the entire track with a coverage of 29% for CCA+P and 8% for the green algae on build-ups (Green algae 1+2). The SAM identifies well green algae *C. prolifera* (Green algae 3) and the seagrass *P. oceanica* with a coverage of 0.7% and 0.9% of the total classified area, respectively. The taxa associated with coralligenous are easily distinguishable with a total coverage of 0.13%. We highlight the low percentage of unclassified pixel (1.5% in total).

### 3.5. Classification accuracy for CWC and Coralligenous Sites

The CWC SAM has a high overall accuracy (84.38%) as determined from the confusion matrix comparing the predicted classes with the real classes (see Table 3). The colonial cnidarian class gives 100% UA and 87.5% PU showing the presence of a minimum number of false negative along the deepest section of the analysed segment. The sponges (sponge 1, sponge 2+3, sponge 4) show a lower value in terms of PA (87.50%) than UA (100%) due to the presence of false negative. The bedrock and mud classes show almost the same accuracy (>60% both for PA and UA) both for the presence of false negative and positive.

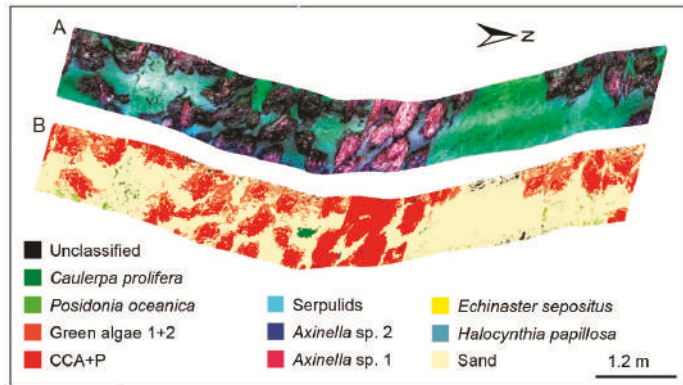


Figure 5. RGB UHI image of the coralligenous site in A and its SAM classification in B.

The overall accuracy of the SAM for the coralligenous is 72% (see Table 4). There is a high discrepancy between PA and UA for the *P. oceanica* and *C. prolifera* (Green algae 3) classes with no commission errors (100% UA), but with a level of reliability of 37.5% and 50% due to a higher omission errors. For the sand class, the UA is extremely low (25%) because of the high number of false positive. For the CCA+P both PA and UA are 100%. The green algae on build-ups (green algae 1+2) shows no false positives (100% UA) and a PA higher than the overall value (87.5%). In general, all organisms associated with the coralligenous build-ups have a high level of accuracy (> 88% both for PA and UA), with the exception of *Axinella* sp. 1 (75% PA) showing the presence of false negatives.

Table 3. Confusion Matrix for the CWC site classification.

Overall Accuracy 84.38%						
	Mud	Sponge	Bedrock	C. cnidarian	TOT	UA
Mud	7	0	2	1	10	67.78
Sponge	0	7	0	0	7	100.00
Bedrock	1	1	6	0	8	66.67
C. cnidarian	0	0	0	7	7	100.00
TOT	8	8	8	8	32	
PA	87.50	87.50	75.00	87.5		

Table 4. Confusion Matrix for the coralligenous site classification.

Overall Accuracy 72%												
	Serpulids	E. sepositus	H. papillosa	Axinella sp.1	Axinella sp.2	CCA+P	Green Algae 3	Sand	P. oceanica	Green Algae 1+2	TOT	UA
Serpulids	7	0	0	0	0	0	0	0	0	0	7	100.0
E. sepositus	0	8	0	0	0	0	0	0	0	0	8	100.0
H. papillosa	0	0	8	1	0	0	0	0	0	0	9	88.9
Axinella sp.1	0	0	0	6	0	0	0	0	0	0	6	100.0
Axinella sp.2	0	0	0	0	8	0	0	0	0	0	8	100.0
CCA+P	1	0	0	1	0	8	0	1	0	0	11	61.5
Green algae 3	0	0	0	0	0	0	3	0	0	0	3	100.0
Sand	0	0	0	0	0	0	5	5	4	1	15	25.0
P. oceanica	0	0	0	0	0	0	0	0	4	0	4	100.0
Green algae 1+2	0	0	0	0	0	0	0	2	0	7	9	70.0
TOT	8	8	8	8	8	8	8	8	8	8	80	
PA	87.5	100	100	75	100	100	37.5	62.5	50	87.5		

#### 4. Discussion

##### 4.1. Evaluation of the Acquisition Set-up and Suggestion of Best Practice for Data Collection

The acquisition of high-quality UHI is challenging because of the requirements to perform a satisfactory survey, such as maintaining a constant speed, heading and altitude, as well as

high-resolution navigation data [5–7]. Proper illumination is mandatory to avoid the acquisition of “striped” images, characterised by shadowed and hyper-illuminated areas, leading to misclassification of the acquired images.

In our survey, the ROV met most requirements, yet seafloor illumination and navigation data were not optimal. At both sites, the illumination was uneven due to a non-optimal configuration of the lamps (two lamps for the ROV RGB camera running simultaneously with two UHI lamps) and articulated topography. This condition affected the CWC site the most, where pixels on the western side of the image, characterised by a constant darker area, could not be strictly compared to those of the eastern side. For the coralligenous site, the presence of sunlight improved the condition, giving a more homogeneous illumination of the surveyed track, which was also favoured by a rather flat topography.

Furthermore, the low accuracy of the underwater positioning system sometimes induced image distortion and a lower spatial resolution of the geocorrected images, more evident at the CWC site. Finally, the difficulty in maintaining the correct ROV altitude in areas characterized by seafloor heterogeneity, a common trait at both study sites, may have influenced the reliability of UHI acquisition and, therefore, classification [26].

Based on our experience, we can summarise some best practices needed to acquire good quality hyperspectral images using an ROV. A rigorous UHI survey functional to seafloor mapping requires:

- an ROV ensuring a constant heading and altitude above the seafloor and suitable to host the UHI and other devices (e.g., RGB camera, lamps);
- an efficient positioning system for the ROV and the UHI itself, able to provide accurate and adequately dense navigation data;
- an appropriate lamp system to illuminate the surveyed area uniformly in function of water depth and sunlight;
- an RGB camera mounted vertically alike the UHI camera, to record concomitantly the seafloor for the OOI identification;
- an advanced background knowledge of the target area.

#### 4.2. Evaluation of Spectral Libraries for Seafloor Mapping

A spectral library permits a quick and reliable classification of benthic habitats and their individual components up to taxonomic level, if a substantial number of reference spectra has been filed [7]. Its construction represents one of the most challenging and time-consuming aspects of the automatic classification of the UHI images.

In this perspective, it appears obvious that there is a strong need to implement substantially the spectral library with respect to the deep-water scleractinians (CWCs). Living *M. oculata* appears to contain a variety of colored facies from white to pinkish hues [64]. The same holds true for *D. pertusum*, a species also present at the CWC site here considered, whose living colonies cover a chromatic spectrum from white to orange, up to reddish [65,66]. Dead skeletons of these and other CWCs are often co-occurring, further complicating the hyperspectral approach as they are characterized by whitish, yellowish and brownish colours. However, UHI is documented [5] to discriminate the optical fingerprints of white, orange and dead *D. pertusum*.

A robust sponge taxonomic classification requires the analysis of spicules and genetics, while the external morphology or colour commonly provides only an indication of ‘morpho-species’ or ‘morpho-categories’ [67]. In the specific case of the deep-water situation here considered, the large fan-shaped sponges (i.a., *P. compressa* and *P. monilifera*, often co-occurring together with other sponges) are characterized by a wide range of colours even within the same taxon [36,68–70]. Therefore, collected spectra are not unequivocally associated to species, making difficult a precise taxonomic assignment.

The resilient core of the Coralligenous habitat is hard, hosting a variety of fauna and flora, the latter often seasonal and epibiontic. At times, such seasonal overgrowth may mask, often significantly but ephemerally, the underlying substrate provided by CCA and Peyssonelliales. These considerations

are relevant in defining the spectral library associated with coralligenous as a unique habitat, when tested using the UHI camera. Concerning algae, supervised UHI classification was unable to map accurately different red algae species, due to their similarity on the optical fingerprint, deciding instead for grouping [26]. We tested that the spectral fingerprint of CCA and Peyssonelliales as an opting group is conspicuous enough to be distinguished in the natural environment, where their presence prevails with seasonal and accidental signals (such as green algae bloom or megabenthos).

#### 4.3. SAM Classification

For our scope, the SAM classification is considered ideal because it is intensity independent (LED lamps and sunlight illumination) and focuses only on identifying the spectral similarity (i.e., colour). The SAM method can eliminate the effect of the spectral brightness values (i.e., spectral vector lengths in feature space) on the classification and it is insensitive to the data variance, imparting a significant advantage for the analysis of regions with complex terrain [63]. On the other hand, this method is highly dependent on the wavelength ranges and on the thresholds selected, which are arbitrary [62]. In our study, we choose several ROIs for the same benthic class for different illumination conditions, because the illumination is not influencing only the reflectance intensity, but also colour variation (e.g., colonial cnidarian 1 in Figure 2E results blue).

At the CWC site, SAM was functional in recognizing colonial cnidarians and sponges. However, the method proved inadequate in discriminating between mud and bedrock substrates, probably characterized here by similar spectra, hampering a reliable mapping of the seafloor (Figure 4 B).

The CCA+P and associated organisms were correctly classified at the coralligenous site, despite habitat heterogeneity. Green algae as *C. bursa* and *F. petiolata* (Green algae 1+2) appear overestimated, since SAM imported artifacts such as the build-up shadows and distortions (Figure 6).

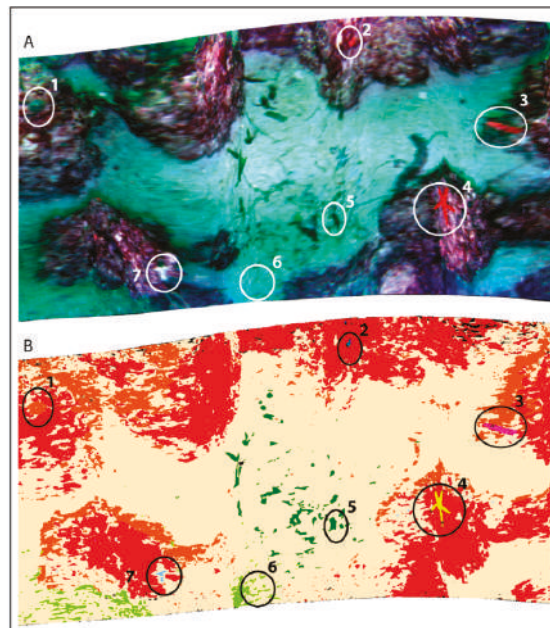


**Figure 6.** Zoom in the classified segment of coralligenous site, where numbers indicate the organism identified (A) and classified (B): 1. *C. bursa*, 2. *H. papillosa*, 3. *Axinella* sp. 1, 4. *E. sepositus*, 5. *C. prolifera*, 6. *P. oceanica*, 7. Serpulids. For the colour legend in B, see Figure 5.

According to confusion matrices limited to the dataset analysed in this study, the SAM classification accuracy is higher for the CWC (84.38%) than for the coralligenous (72%) site. This result could derive from differences in habitat complexity. Firm numbers on the overall classification accuracy could be obtained by increasing the number of iterations or considering a larger dataset.

#### 4.4. Evaluation of the UHI for Seabed Monitoring

Our tests document that the UHI method is able to map the habitat extent independently of the water depth and at a high level of spatial detail. The UHI provides the effective spatial coverage of CWCs habitat-formers and coralligenous builds-ups (Figure 7), which is hard to estimate using conventional methods. This level of detail is extremely useful for monitoring purposes (e.g., MSFD) enabling a quantitative and repeatable measure of habitat extent and distribution. However, this process is heavily time-consuming compared to the conventional ROV approach, mostly due to inadequate spectral libraries, which is the major limitation to date.

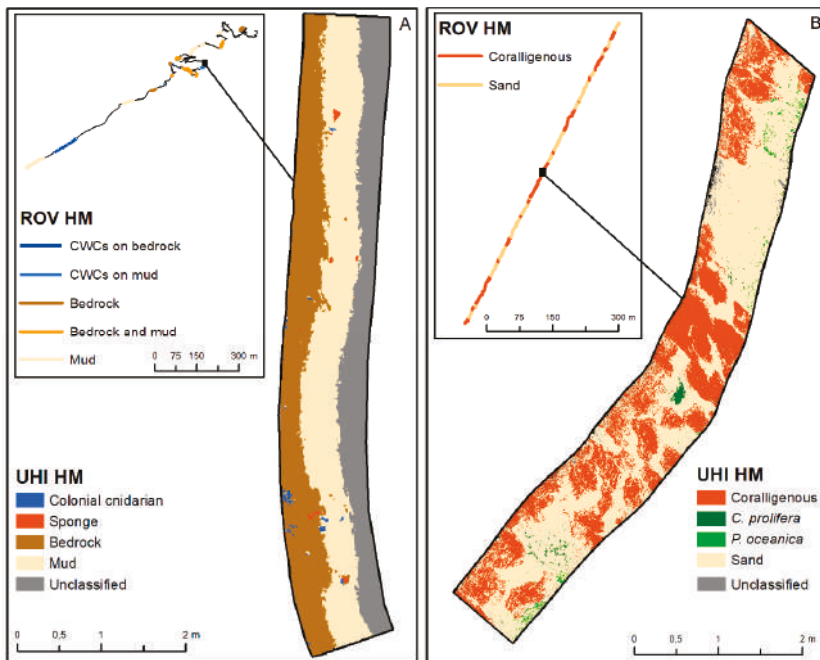


**Figure 7.** Comparison between the ROV transect classified with conventional methodologies (A and B insert) and the UHI classification for (A) CWC and (B) coralligenous sites. The image shows the higher level of detailed obtained by the UHI camera, in contrast with the larger amount of data analyzed by the ROV video.

## 5. Conclusions

This first application of the UHI camera in the Mediterranean Sea (Southern Adriatic Sea) confirmed its potential for underwater habitat mapping in shallow and deep water.

We tested the UHI camera in two geomorphological contexts containing charismatic marine benthic habitats. We noticed that the quality of the positioning system, the illumination settings and the complexity of the seafloor affected the UHI performance and the hyperspectral image analysis. We created a preliminary spectral library for each site enabling a supervised classification (SAM), which discriminated between substrates, megafauna and megafloora in a satisfactory manner.

Given substantially implemented spectral libraries, the UHI camera will likely represent a valid aid for habitat mapping and monitoring, in the perspective of quantifiable and repeatable classifications and European MSFD indicators.

**Supplementary Materials:** The UHI raw data analyzed in this work and relative documentation are stored as Data Research Object (RO) in ROHUB at the following link: [http://www.rohub.org/rodetails/UHI\\_Data/overview](http://www.rohub.org/rodetails/UHI_Data/overview).

**Author Contributions:** Conceptualization, Federica Foglini; Data curation, Valentina Grande, Fabio Marchese, Valentina Alice Bracchi, Mariacristina Prampolini, Ingrid Myrnes Hansen, Magne Gudmundsen and Agostino Niyonkuru Meroni; Formal analysis, Federica Foglini, Valentina Grande, Fabio Marchese, Valentina Alice Bracchi, Mariacristina Prampolini and Giorgio Castellan; Funding acquisition, Federica Foglini, Fabio Badalamenti, Cesare Corselli, Eleonora Martorelli and Alessandra Savini; Investigation, Federica Foglini, Valentina Grande, Fabio Marchese, Mariacristina Prampolini, Lorenzo Angeletti, Giovanni Chimienti, Agostino Niyonkuru Meroni, Alessandra Mercorella, Agostina Vertino and Marco Taviani; Resources, Ivar Erdal; Validation, Federica Foglini; Writing—original draft, Federica Foglini, Valentina Grande, Fabio Marchese, Valentina Alice Bracchi, Mariacristina Prampolini, Lorenzo Angeletti, Giovanni Chimienti, Ingrid Myrnes Hansen, Fabio Badalamenti, Eleonora Martorelli and Marco Taviani.

**Funding:** Flagship Project RITMARE (La Ricerca Italiana per il Mare) and EVER-EST projects (ID: 674907).

**Acknowledgments:** Captain, crew and scientific staff on-board of the R/V Minerva Uno and three ROV pilots are acknowledged for their support during the operations at sea. The research is part of the National Flagship Project RITMARE (La Ricerca Italiana per il Mare), and a contribution to EU EVER-EST, EU IDEM and MIUR GLIDE projects. ISMAR-CNR Bologna scientific contribution n. 1996. This paper is a scientific contribution of Project MIUR—Dipartimenti di Eccellenza 2018–2022.

**Conflicts of Interest:** The authors declare no conflict of interest.

## References

1. Brown, C.J.; Smith, S.J.; Lawton, P.; Anderson, J.T. Benthic habitat mapping: A review of progress towards improved understanding of the spatial ecology of the seafloor using acoustic techniques. *Estuar. Coast. Shelf Sci.* **2011**, *92*, 502–520. [CrossRef]
2. Angeletti, L.; Bargain, A.; Foglini, F.; Grande, V.; Prampolini, M.; Taviani, M. Cold-water coral multiscale habitat mapping: Methodologies and perspectives. In *Mediterranean Cold-Water Corals: Past, Present and Future, Coral Reefs of the World*; Orejas, C., Jiménez, C., Eds.; Springer International Publishing: Berlin, Germany, 2019; Volume 9.
3. Lim, A.; Wheeler, A.J.; Arnaubec, A. High-resolution facies zonation within a cold-water coral mound: The case of the Piddington Mound, Porcupine Seabight, NE Atlantic. *Mar. Geol.* **2017**, *390*, 120–130. [CrossRef]
4. Berg, T.; Fühaupter, K.; Teixeira, H.; Uusitalo, L.; Zampoukas, N. The Marine Strategy Framework Directive and the ecosystem-based approach—pitfalls and solutions. *Mar. Pollut. Bull.* **2015**, *96*, 18–28. [CrossRef]
5. Johnsen, G.; Volent, Z.; Dierssen, H.; Pettersen, R.; Ardelan, M.V.; Søreide, F.; Fearn, P.; Ludvigsen, M.; Moline, M. Underwater hyperspectral imagery to create biogeochemical maps of seafloor properties. In *Subsea Optics and Imaging*, 1st ed.; Watson, J., Zielinski, O., Eds.; Elsevier: Amsterdam, the Netherlands, 2013; pp. 508–540.
6. Dumke, I.; Nornes, S.M.; Purser, A.; Marcon, Y.; Ludvigsen, M.; Ellefmo, S.L.; Johnsen, G.; Søreide, F. First hyperspectral imaging survey of the deep seafloor: High-resolution mapping of manganese nodules. *Remote Sens. Environ.* **2018**, *209*, 19–30. [CrossRef]
7. Dumke, I.; Purser, A.; Marcon, Y.; Nornes, S.M.; Johnsen, G.; Ludvigsen, M.; Søreide, F. Underwater hyperspectral imaging as an in situ taxonomic tool for deep-sea megafauna. *Sci. Rep.* **2018**, *8*, 12860. [CrossRef] [PubMed]
8. Klonowski, W.M.; Fearn, P.R.C.S.; Lynch, M.J. Retrieving key benthic cover types and bathymetry from hyperspectral imagery. *JARS* **2007**, *1*, 011505. [CrossRef]
9. Volent, Z.; Johnsen, G.; Sigernes, F. Kelp forest mapping by use of airborne hyperspectral imager. *J. Appl. Remote Sens.* **2007**, *1*, 011505. [CrossRef]
10. Fearn, P.R.C.; Klonowski, W.; Babcock, R.C.; England, P.; Phillips, J. Shallow water substrate mapping using hyperspectral remote sensing. *Cont. Shelf Res.* **2011**, *31*, 1249–1259. [CrossRef]
11. Chang, C.; Member, S.; Du, Q. Estimation of Number of Spectrally Distinct Signal Sources in Hyperspectral Imagery. *IEEE Trans. Geosci. Remote Sens.* **2004**, *42*, 608–619. [CrossRef]

12. Dickey, T.; Lewis, M.; Chang, G. Optical oceanography: Recent advances and future directions using global remote sensing and in situ observations. *Rev. Geophys.* **2006**, *44*, 1–39. [[CrossRef](#)]
13. Dierssen, H.M.; Randolph, K. Remote Sensing of Ocean Color. In *Earth System Monitoring*; Orcutt, J., Ed.; Springer: New York, NY, USA, 2013; pp. 439–472. ISBN 978-1-4614-5683-4.
14. Hochberg, E.J.; Atkinson, M.J. Spectral discrimination of coral reef benthic communities. *Coral Reefs* **2000**, *19*, 164–171. [[CrossRef](#)]
15. Hochberg, E.J.; Atkinson, M.J.; Andréfouët, S. Spectral reflectance of coral reef bottom-types worldwide and implications for coral reef remote sensing. *Remote Sens. Environ.* **2003**, *85*, 159–173. [[CrossRef](#)]
16. Kutser, T.; Miller, I.; Jupp, D.L.B. Mapping coral reef benthic substrates using hyperspectral space-borne images and spectral libraries. *Estuar. Coast. Shelf Sci.* **2006**, *70*, 449–460. [[CrossRef](#)]
17. Petit, T.; Bajjouk, T.; Mouquet, P.; Rochette, S.; Vozel, B.; Delacourt, C. Hyperspectral remote sensing of coral reefs by semi-analytical model inversion—Comparison of different inversion setups. *Remote Sens. Environ.* **2017**, *190*, 348–365. [[CrossRef](#)]
18. Phinn, S.; Roelfsema, C.; Dekker, A.; Brando, V.; Anstee, J. Mapping seagrass species, cover and biomass in shallow waters: An assessment of satellite multi-spectral and airborne hyper-spectral imaging systems in Moreton Bay (Australia). *Remote Sens. Environ.* **2008**, *112*, 3413–3425. [[CrossRef](#)]
19. Dierssen, H.M. Overview of hyperspectral remote sensing for mapping marine benthic habitats from airborne and underwater sensors. In *Imaging Spectrometry XVIII, Proceedings of SPIE- International Society for Optics and Photonics, San Diego, CA, USA, 26–28 August 2013*; Mouroulis, P., Ed.; 2013; Volume 8870.
20. Dierssen, H.M.; Chlus, A.; Russell, B. Hyperspectral discrimination of floating mats of seagrass wrack and the macroalgae *Sargassum* in coastal waters of Greater Florida Bay using airborne remote sensing. *Remote Sens. Environ.* **2015**, *167*, 247–258. [[CrossRef](#)]
21. Chennu, A.; Färber, P.; Volkenborn, N.; Al-Najjar, M.A.A.; Janssen, F.; de Beer, D.; Polerecky, L. Hyperspectral imaging of the microscale distribution and dynamics of microphytobenthos in intertidal sediments. *Limnol. Oceanogr. Methods* **2013**, *11*, 511–528. [[CrossRef](#)]
22. Pettersen, R.; Johnsen, G.; Bruheim, P.; Andreassen, T. Development of hyperspectral imaging as a bio-optical taxonomic tool for pigmented marine organisms. *Org. Divers. Evol.* **2014**, *14*, 237–246. [[CrossRef](#)]
23. Ludvigsen, M.; Gjohansen, G.; Sørensen, A.J.; Lågstad, P.A.; Ødegård, Ø. Scientific operations combining ROV and AUV in the Trondheim Fjord. *Mar. Technol. Soc. J.* **2014**, *48*, 59–71. [[CrossRef](#)]
24. Tegdan, J.; Ekehaug, S.; Hansen, I.M.; Sandvik Aas, L.M.; Steen, K.J.; Pettersen, R.; Beuchel, F.; Camus, L. Underwater hyperspectral imaging for environmental mapping and monitoring of seabed habitats. In *Proceedings of the OCEANS 2015, Genova, Italy, 18–21 May 2015*; pp. 1–6.
25. Johnsen, G.; Ludvigsen, M.; Sørensen, A.; Sandvik Aas, L.M. The use of underwater hyperspectral imaging deployed on remotely operated vehicles—Methods and applications. *IFAC* **2016**, *49*, 476–481. [[CrossRef](#)]
26. Mogstad, A.A.; Johnsen, G. Spectral characteristics of coralline algae: A multi-instrumental approach, with emphasis on underwater hyperspectral imaging. *Appl. Opt.* **2017**, *56*, 9957. [[CrossRef](#)]
27. Ødegård, Ø.; Mogstad, A.A.; Johnsen, G.; Sørensen, A.J.; Ludvigsen, M. Underwater hyperspectral imaging: A new tool for marine archaeology. *Appl. Opt.* **2018**, *57*, 3214. [[CrossRef](#)]
28. Sture, Ø.; Ludvigsen, M.; Søreide, F.; Sandvik Aas, L.M. Autonomous underwater vehicles as a platform for underwater hyperspectral imaging. In *Proceedings of the OCEANS 2017, Aberdeen, UK, 19–22 June 2017*; pp. 1–8.
29. Cochrane, S.K.J.; Ekehaug, S.; Refit, E.C.; Hansen, I.M.; Sandvik Aas, L.M. Detection of deposited drill cuttings on the sea floor—A comparison between underwater hyperspectral imagery and the human eye. *Mar. Pollut. Bull.* **2019**. in review.
30. Ødegård, Ø.; Sørensen, A.J.; Hansen, R.E.; Ludvigsen, M. A new method for underwater archaeological surveying using sensors and unmanned platforms. *IFAC-PapersOnLine* **2016**, *49*, 486–493.
31. Letnes, P.A.; Hansen, I.M.; Sandvik Aas, L.M.; Eide, I.; Pettersen, R.; Tassara, L. Underwater hyperspectral classification of deep sea corals exposed to 2-methylnaphthalene. *PLoS ONE* **2019**, *14*, e0209960. [[CrossRef](#)]
32. Fogliani, F.; Angeletti, L.; Bracchi, V.A.; Chimienti, G.; Grande, V.; Hansen, I.M.; Meroni, A.N.; Marchese, F.; Mercorella, A.; Prampolini, M.; et al. Underwater Hyperspectral Imaging for seafloor and benthic habitat mapping. In *Proceedings of the 2018 IEEE International Workshop on Metrology for the sea (MetroSea 2018)*, Bari, Italy, 8–10 October 2018; pp. 201–205.

33. Gavazzi, G.M.; Madricardo, F.; Janowski, L.; Kruss, A.; Blondel, P.; Sigovini, M.; Foglini, F. Evaluation of seabed mapping methods for fine-scale classification of extremely shallow benthic habitats—Application to the Venice Lagoon, Italy. *Estuar. Coast. Shelf Sci.* **2016**, *170*, 45–60. [[CrossRef](#)]
34. Ingrosso, G.; Abbiati, M.; Badalamenti, F.; Bavestrello, G.; Belmonte, G.; Cannas, R.; Benedetti-Cecchi, L.; Bertolino, M.; Bevilacqua, S.; Bianchi, C.N.; et al. Mediterranean Bioconstructions Along the Italian Coast. *Adv. Mar. Biol.* **2018**, *79*, 61–136.
35. Freiwald, A.; Beuck, L.; Rüggeberg, A.; Taviani, M.; Hebbeln, D.; R/V Meteor Cruise M70-1 Participants. The white coral community in the Central Mediterranean Sea Revealed by ROV Surveys. *Oceanography* **2009**, *22*, 58–74. [[CrossRef](#)]
36. Angeletti, L.; Taviani, M.; Canese, S.; Foglini, F.; Mastrototaro, F.; Argnani, A.; Trincardi, F.; Bakran-Petricioli, T.; Ceregato, A.; Chimienti, G.; et al. New deep-water cnidarian sites in the southern Adriatic Sea. *Mediterr. Mar. Sci.* **2014**, *15*, 263–273. [[CrossRef](#)]
37. D’Onghia, G.; Capezzuto, F.; Cardone, F.; Carlucci, R.; Carluccio, A.; Chimienti, G.; Corriero, G.; Longo, C.; Maiorano, P.; Mastrototaro, F.; et al. Macro-and megafauna recorded in the submarine Bari Canyon (southern Adriatic, Mediterranean Sea) using different tools. *Mediterr. Mar. Sci.* **2015**, *16*, 180–196. [[CrossRef](#)]
38. Taviani, M.; Angeletti, L.; Beuck, L.; Campiani, E.; Canese, S.; Foglini, F.; Freiwald, A.; Montagna, P.; Trincardi, F. Reprint of ‘On and off the beaten track: Megafaunal sessile life and Adriatic cascading processes’. *Mar. Geol.* **2016**, *375*, 146–160. [[CrossRef](#)]
39. Taviani, M.; Angeletti, L.; Cardone, F.; Montagna, P.; Danovaro, R. A unique and threatened deep water coral-bivalve biotope new to the Mediterranean Sea offshore the Naples megalopolis. *Sci. Rep.* **2019**, *9*, 3411. [[CrossRef](#)] [[PubMed](#)]
40. Chimienti, G.; Bo, M.; Taviani, M.; Mastrototaro, F. Occurrence and Biogeography of Mediterranean Cold-Water Corals. In *Mediterranean Cold-Water Corals: Past, Present and Future, Coral Reefs of the World*; Orejas, C., Jiménez, C., Eds.; Springer International Publishing: Berlin, Germany, 2019; Volume 9. (in press)
41. Foglini, F.; Angeletti, L.; Campiani, E.; Correggiari, A.; Grande, V.; Leidi, E.; Madricardo, F.; Mercorella, A.; Remia, R.; Taviani, M. Habitat mapping in the Adriatic (Mediterranean Sea) from coastal areas to deep sea: Approaches and methodologies for assessing seafloor habitat for sustainable and integrated sea management strategy. In Proceedings of the GeoHab 2015, Salvador, Brazil, 3–8 May 2015.
42. Sanfilippo, R.; Vertino, A.; Rosso, A.; Beuck, L.; Freiwald, A.; Taviani, M. *Serpula* aggregates and their role in deep-sea coral communities in the southern Adriatic Sea. *Facies* **2013**, *59*, 663–677. [[CrossRef](#)]
43. Bargain, A.; Foglini, F.; Pairaud, I.; Bonaldo, D.; Carniel, S.; Angeletti, L.; Taviani, M.; Rochette, S.; Fabri, M.C. Predictive habitat modeling in two Mediterranean canyons including hydrodynamic variables. *Prog. Oceanogr.* **2018**, *169*, 151–168. [[CrossRef](#)]
44. Addamo, A.M.; Vertino, A.; Stolarski, J.; García-Jiménez, R.; Taviani, M.; Machordom, A. Merging scleractinian genera: The overwhelming genetic similarity between solitary *Desmophyllum* and colonial *Lophelia*. *BMC Evol. Biol.* **2016**, *16*, 108. [[CrossRef](#)]
45. Bracchi, V.; Savini, A.; Marchese, F.; Palamara, S.; Basso, D.; Corselli, C. Coralligenous habitat in the Mediterranean Sea: A geomorphological description from remote data. *Ital. J. Geosci.* **2015**, *134*, 32–40. [[CrossRef](#)]
46. Bracchi, V.A.; Basso, D.; Marchese, F.; Corselli, C.; Savini, A. Coralligenous morphotypes on subhorizontal substrate: A new categorization. *Cont. Shelf Res.* **2017**, *144*, 10–20. [[CrossRef](#)]
47. Laborel, J. Le concrétionnement algal ‘coralligène’ et son importance géomorphologique en Méditerranée. *Recueil des travaux Station Marine d’Endoume* **1961**, *23*, 37–60.
48. Pérès, J.M.; Picard, J. Nouveau manuel de bionomie benthique de la mer Méditerranée. *Recent Trav. De La Stn. Mar. De Endoume* **1964**, *31*, 1–137.
49. Bellan-Santini, D.; Lacaze, J.C.; Poizat, C. Les biocénoses marines et littorales de Méditerranée, synthèse, menaces et perspectives. *Collection Patrimoines Naturels. Muséum National d’Histoire Naturelle* **1994**, *19*, 1–246.
50. Bressan, G.; Babbini, I.; Ghirardelli, L.; Basso, D. Bio-costruzione e bio-distruzione di corallinali nel Mar Mediterraneo. *Biol. Mar. Mediterr.* **2001**, *8*, 131–174.
51. Ballesteros, E. Mediterranean coralligenous assemblages: A synthesis of present knowledge. *Oceanogr. Mar. Biol. Annu. Rev.* **2006**, *44*, 123–195.
52. Piazzì, L.; Gennaro, P.; Balata, D. Threats to macroalgal coralligenous assemblages in the Mediterranean Sea. *Mar. Poll. Bull.* **2012**, *64*, 2623–2629. [[CrossRef](#)]

53. Chimienti, G.; Stithou, M.; Mura, I.D.; Mastrototaro, F.; D'Onghia, G.; Tursi, A.; Izzi, C.; Fraschetti, S. An explorative assessment of the importance of Mediterranean Coralligenous habitat to local economy: The case of recreational diving. *J. Environ. Account. Manag.* **2017**, *5*, 315–325. [CrossRef]
54. Sarà, M. *Research on Benthic Fauna of Southern Adriatic Italian Coast: Final Scientific Report*; Office of Naval Research: Washington, DC, USA, 1968; pp. 1–53.
55. Sarà, M. Un biotopo da proteggere: Il coralligeno pugliese. In Proceedings of the Atti del I Simposio Nazionale sulla Conservazione della Natura, Bari, Italy, 21–25 April 1971; pp. 145–151.
56. Angeletti, L.; Prampolini, M.; Fogliani, F.; Grande, V.; Taviani, M. Cold-water coral habitat in the Bari Canyon System, Southern Adriatic Sea (Mediterranean Sea). In *Seafloor Geomorphology as Benthic Habitat*, 2nd ed.; Harris, P., Baker, E., Eds.; Elsevier: Amsterdam, the Netherlands, 2019. (in press)
57. Johnsen, G.; Volent, Z.; Sakshaug, E.; Sigernes, F.; Pettersson, L. Remote sensing in the Barents Sea. In *Ecosystem Barents Sea*; Sakshaug, E., Johnsen, G.H., Kovacs, K.M., Eds.; Fagbokforlaget: Bergen, Norway, 2009; Volume 2, pp. 139–166.
58. Dukan, F.; Ludvigsen, M.; Sorensen, A.J. Dynamic positioning system for a small size ROV with experimental results. In Proceedings of the IEEE OCEANS, Santander, Spain, 6–9 June 2011; pp. 1–10. [CrossRef]
59. Williams, D.J.; Shah, M. A fast algorithm for active contours and curvature estimation. *CVGIP Image Under.* **1992**, *55*, 14–26. [CrossRef]
60. R Core Team. *R: A Language and Environment for Statistical Computing*; R Foundation for Statistical Computing: Vienna, Austria, 2013; Available online: <http://www.R-project.org/> (accessed on 18 May 2019).
61. Kruse, F.A.; Heidebrecht, K.B.; Shapiro, A.T.; Barloon, P.J.; Goetz, A.F.H. The Spectral Image Processing System (SIPS) Interactive Visualization and Analysis of Imaging Spectrometer Data. *Remote Sens. Environ.* **1993**, *44*, 145–163. [CrossRef]
62. Crósta, A.P.; Sabine, C.; Taranik, J.V. Hydrothermal Alteration Mapping at Bodie, California, Using AVIRIS Hyperspectral Data. *Remote Sens. Environ.* **1998**, *64*, 309–319. [CrossRef]
63. Liu, Y.; Lu, S.; Lu, X.; Wang, Z.; Chen, C.; He, H. Classification of Urban Hyperspectral Remote Sensing Imagery Based on Optimized Spectral Angle Mapping. *J. Indian Soc. Remote Sens.* **2019**, *47*, 289–294. [CrossRef]
64. Boland, G.S.; Etnoyer, P.J.; Fisher, C.R.; Hickerson, E.L. State of deep-sea coral and sponge ecosystems of the Gulf of Mexico Region: Texas to the Florida Straits. In *The State of Deep-Sea Coral and Sponge Ecosystems of the United States*; Hourigan, T.F., Etnoyer, P.J., Cairns, S.D., Eds.; NOAA Tech. Memo. NMFS-OHC-4; Silver Spring: Silver, MD, USA, 2017; pp. 321–378.
65. Freiwald, A. Geobiology of *Lophelia pertusa* (Scleractinia) Reefs in the North Atlantic. Unpublished Habilitation Thesis, Bremen University, Bremen, Germany, 1998.
66. Freiwald, A.; Fosså, J.H.; Grehan, A.; Koslow, T.; Roberts, J.M. Cold-water coral reefs—Out of sight—No longer out of mind. In *UNEP-WCMC Biodiversity*; UNEP Coral Reef Unit: Cambridge, UK, 2004; Volume 22, pp. 1–84.
67. Santín, A.; Grynó, J.; Ambroso, S.; Uriz, M.J.; Dominguez-Carrió, C.; Gili, J.M. Distribution patterns and demographic trends of demosponges at the Menorca Channel (Northwestern Mediterranean Sea). *Prog. Oceanogr.* **2019**, *173*, 9–25. [CrossRef]
68. Bell, J.J.; Barnes, D.K.A. Sponge morphological diversity: A qualitative predictor of species diversity? *Aquat. Conserv.* **2001**, *11*, 109–121. [CrossRef]
69. Calcinai, B.; Moratti, V.; Martinelli, M.; Bavestrello, G.; Taviani, M. Uncommon sponges associated with deep coral bank and maerl habitats in the Strait of Sicily (Mediterranean Sea). *Ital. J. Zool.* **2013**, *80*, 412–423. [CrossRef]
70. Rueda, J.L.; Urrea, J.; Aguilar, R.; Angeletti, L.; Bo, M.; García-Ruiz, C.; González-Duarte, M.; López, E.; Madurell, T.; Maldonado, M.; et al. Cold-water coral associated fauna in the Mediterranean Sea and adjacent areas. In *Mediterranean Cold-Water Corals: Past, Present and Future, Coral Reefs of the World*; Orejas, C., Jiménez, C., Eds.; Springer International Publishing: Berlin, Germany, 2019; Volume 9.



MDPI  
St. Alban-Anlage 66  
4052 Basel  
Switzerland  
Tel. +41 61 683 77 34  
Fax +41 61 302 89 18  
[www.mdpi.com](http://www.mdpi.com)

*Sensors* Editorial Office  
E-mail: [sensors@mdpi.com](mailto:sensors@mdpi.com)  
[www.mdpi.com/journal/sensors](http://www.mdpi.com/journal/sensors)



MDPI  
St. Alban-Anlage 66  
4052 Basel  
Switzerland

Tel: +41 61 683 77 34  
Fax: +41 61 302 89 18

[www.mdpi.com](http://www.mdpi.com)



ISBN 978-3-03928-407-8